Engine Integration Flying-V

Design Methodology for Unconventional Engine Mounting Structures, Including Crashworthiness Assessment

R. Koenderink

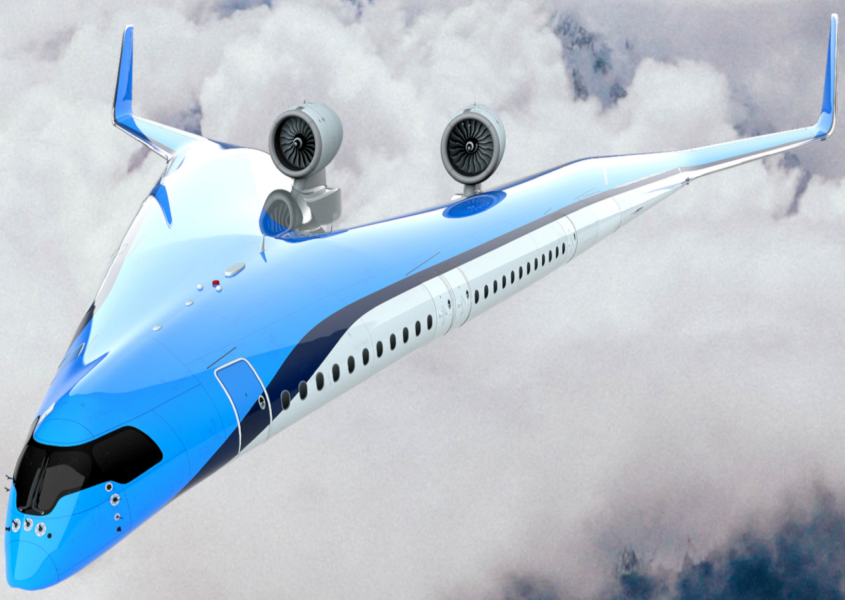

Delft University of Technology

TU Delft

This page is intentionally left blank

Engine Integration Flying-V

Design Methodology for Unconventional Engine Mounting Structures, Including Crashworthiness Assessment

by

R. Koenderink

In fulfilment of the requirements to obtain the degree of
Master of Science in Aerospace Engineering,
at Delft University of Technology

To be defended publicly at the Faculty of Aerospace Engineering at Delft University of Technology,
on February 28, 2024 at 9:30 CET.

Student number:	5643872	
Project Duration:	September, 2022 - February, 2024	
Thesis committee:	Dr. ing. S.G.P. Castro	TU Delft, Daily supervisor
	Dr. ir. R.C. Alderliesten	TU Delft, Secondary supervisor
	Dr. ir. O.K. Bergsma	TU Delft, Chair
	Dr. ir. R. Vos	TU Delft, Examiner

TU Delft

This page is intentionally left blank

Acknowledgements

This master thesis marks the end of my educational journey which started in Enschede at University of Twente with a bachelor in Mechanical Engineering. I have always had an interest in the aerospace field, and after completion of my bachelors I decided to pursue my interest by doing a master in Aerospace Engineering at TU Delft. Although this journey was not always easy I have enjoyed it and I am very grateful to everyone who have helped me along the way.

Firstly I want to thank my daily supervisor Saullo G.P. Castro and co-supervisor Rene C. Alderliesten. Their expertise and enthusiasm has helped me become a better engineer and have greatly improved the quality of this thesis. Furthermore, I want to thank Saullo in particular for his availability even in the most busy times. I could not have wished better supervisors and I have enjoyed working with you and I wish to carry forward the same enthusiasm for engineering in my future endeavours.

Additionally, I want to thank Daniel M. Atherstone for his much appreciated support and help regarding the 3DExperience software and Tiago Ferreira da Costa for the collaboration and interesting discussions on the crashworthiness part of the thesis. Without their help I would not have been able to finish a thesis of this quality within the same time frame.

Lastly, I want to thank the persons most dearest to me. Special thanks to my parents, sisters, girlfriend and friends which have always supported me along this journey. I am grateful for the unconditional love and support you have given me.

Rowan Koenderink
Delft, January 2024

Abstract

The need for better fuel efficiency within the growing aviation sector is increasing every day. Meanwhile conventional aircraft are reaching an asymptote regarding fuel efficiency and therefore the focus switches to unconventional aircraft. These aircraft have unique challenges whereof one is the structural connection between engine and aircraft. In this research an automated design methodology is developed which allows for optimization of such a structure. This design methodology uses a parameterised computer-aided design (CAD) connected to Python, which can automatically alter the parameters and make a finite element (FE) model of the design and subsequently run the desired simulations. The results of the simulations are extracted and post-processed into margins of safety (MoS) using the direct results or (semi-)analytical equations for each individual component. In total five failure modes are assessed, which are Von Mises stress, displacement of engine, crippling, panel buckling and column buckling. The most critical MoS and the relation to the parameters is used in combination with an adaptive damping parameter to optimize each individual part. This design methodology is tested using the Flying-V, which is a novel aircraft configuration in the shape of a V, as a reference aircraft. Therefore, first the requirements, critical loadcases, loads and initial design have been developed based on regulations and previous research regarding the Flying-V and have been used as input for the CAD model and simulations. The design methodology has proven not be perfect as regions with stress concentration cause the minimum MoS to be below zero for all iterations and could not be solved within the time frame of this research. However, the design methodology has proven to be significantly faster compared to a design of experiments used in previous research. Overall it should be noted that there are still many other limitations regarding this method. These limitations are related to the limited amount of failure modes used and the fact that it still requires some kind of Design of Experiment, which is time-consuming. The final mass of an optimized engine mounting structure is estimated to be approximately 40% higher than the design methodology used in previous research, which is due to the higher amount of details in the design as well as the significant higher estimated mass for the engine. This means that the current estimated mass for the full engine mounting structure including landing gear and engine is approximately 22150 kg compared to the estimated 17360 kg before.

Furthermore, an assessment of the influence of the developed design on the crashworthiness of the Flying-V has been done. This assessment focuses on one of the four main criteria regarding occupant protection, namely the guarantee of acceptable acceleration and loads sustained by the occupants. This is done by connecting the engine mounting structure to the developed wing-fuselage structure of the Flying-V with a tie connection. In order to compare different cases a new variable has been created, which is based on empirical equations developed by the U.S. Air Force. In addition, a new method based on moments of inertia has been developed to take the rest of the aircraft into account without increasing the size and thus computational effort of the simulation. To validate this method, the wing-fuselage structure has first been extended to fit the structure and results are compared to previous research. This has shown large, unexpected, differences which could not be explained even with thorough investigation. Applying the inertia method to the extended fuselage has shown small but explainable and expected differences, validating that the method has no unforeseen effects on further results. Simulations using this inertia method and the wing-fuselage with full engine mounting structure shows an improved performance in crashworthiness as the engine mount also absorbs some of the energy. Similar simulation without engine shows an even more improved performance, meaning that engine separation is of interest for the Flying-V. Initial further-reaching investigation into engine separation, using a point-mass model, shows that engine separation might be possible without impacting the Flying-V for crashes without any initial yaw, pitch or roll angle.

Contents

List of Figures

List of Tables

Nomenclature

Abbreviations

Abbreviation	Definition
AMC	Acceptable Means of Compliance
CAD	Computer Aided Design
CR	Cruise
CS	Certification Specification
DoE	Design of Experiment
DOF	Degrees of Freedom
DRI	Dynamic Response Index
EASA	European Union Aviation Safety Agency
FE	Finite Elements
FEM	Finite Elements Model
FV	Flying-V
GR	Ground
LD	Landing
MoS	Margin of Safety
MTOW	Maximum Take-Off Weight
MLW	Maximum Landing Weight
MRW	Maximum Ramp Weight
OH	Overhead
OOP	Object Oriented Programming
SEV	Severity index
SSLB	Skin Stiffened Landing Gear Box
TACDWG	Transport Aircraft Crashworthiness and Ditching Working Group
TL	Thrust link
TO	Take-off

Symbols

Symbol	Definition	Unit
a	Length of plate	$[m]$
a	Acceleration	$[ms^{-2}]$
A	Area	$[m^2]$
A	Johnson-Cook hardening variable	$[Nm^{-2}]$
b	Width of plate	$[m]$
b	Width of OH beam	$[m]$
b	Length of flange	$[m]$
b_{eff}	Efficient width of plate post-buckling	$[m]$
B	Johnson-Cook hardening variable	$[Nm^{-2}]$
c	Chord length	$[m]$
c	Johnson-Cook hardening variable	[-]
C_D	Drag coefficient	[-]
d	Diameter	$[m]$
d	Length of web $[m]$	

Symbol	Definition	Unit
D	Drag force	[N]
D	Johnson-Cook damage parameter	[-]
E	Young's modulus	[Pa]
F	Force	[N]
g	Gravitational constant	[ms^2]
G	Acceleration magnitudes	[-]
G_L	Acceleration magnitude limit	[-]
h	Height of OH beam	[m]
I	Second moment of area	[m^4]
I, J	Moment of inertia	[kgm^2]
k	Empirical constant	[-]
k_f	Friction coefficient	[-]
L	Length	[m]
n	Material constant	[-]
n	Johnson-Cook hardening variable	[-]
N	Load	[N]
m	Johnson-Cook hardening variable	[-]
m	Mass	[kg]
M	Moment	[Nm]
P_{cr}	Critical buckling load	[N]
R	Rotation matrix	[-]
t	Thickness	[m]
t_w	Thickness of web	[m]
t_f	Thickness of flange	[m]
T	Temperature	[K]
T	Thrust	[N]
T_{cruise}	Thrust in cruise	[N]
T_m	Melting temperature	[K]
T_{max}	Maximum thrust	[N]
Q_c	Activation energy	[J]
r	Radius	[m]
r	Distance from centerline to engine	[m]
SF	Safety Factor	[-]
u	Velocity in x-direction	[ms^{-1}]
U_{limit}	Maximum allowable deflection of engine	[m]
v	Velocity	[ms^{-1}]
v	Velocity in y-direction	[ms^{-1}]
w	Velocity in z-direction	[ms^{-1}]
x, X	Distance in x-direction	[m]
y, Y	Distance in y-direction	[m]
z, Z	Distance in z-direction	[m]
α	Material constant	[-]
α	Adaptive damping parameter [-]	
δ	Degree of freedom	[-]
δ	Wing sign coefficient	[-]
ζ	Damping ratio	[-]
θ	Rotation of engine around x-axis	[-]
θ	Angle of panel	[-]
θ	Yaw angle	[-]
θ	Angle between engine centerline and zenith	[-]
θ_{limit}	Maximum allowable rotation of engine	[-]
κ	Wing planform coefficient	[-]
Λ	Quarter-chord weep angle	[-]
μ	Friction coefficient	[-]

Symbol	Definition	Unit
ρ	Air density	[kgm^{-3}]
σ	Stress	[Pa]
σ_{cr}	Critical buckling stress	[Pa]
σ_{cy}	Yield strength	[Pa]
σ_f	Critical crippling stress	[Pa]
σ_{Mises}	Von Mises Stress	[Pa]
τ_{ult}	Ultimate shear strength	[Pa]
ν	Poisson ratio	[-]
ν	Thickness distribution coefficient	[-]
ϕ	Rotation of engine around y-axis	[-]
ϕ	Pitch angle	[-]
ψ	Rotation of engine around z-axis	[-]
ψ	Roll angle	[-]
ω	Angular velocity	[s^{-1}]
ω_n	Natural frequency	[s^{-1}]

1 Introduction

In the global aviation market airlines have to cope with increasing amount of passengers. Current projections estimate an increase of 3.6% annually for at least the next two decades [1]. Furthermore, the pressure from society to reduce the amount of emissions and reduce environmental impact is increasing every day and thereby having a massive influence on the aviation sector. In order to deal with both, industry has put their effort in the increase of efficiency in terms of costs, fuel and manufacturing time. However, for the conventional aircraft shape the fuel efficiency has reached an asymptote and therefore research is focussed on unconventional aircraft [24]. One of these aircraft is the blended wing body aircraft by Benad, also nowadays known as the Flying-V and show in Figure 1.1. In the current state of research it is estimated that this aircraft has the potential to be up to 20% more energy efficient compared to an Airbus A350 while having the same capacity [31]. For this reason researchers at Delft University of Technology think it is of most importance to further investigate this concept. As the configuration of the Flying-V is unprecedented certain challenges needs to be overcome to reach an feasible and more efficient final design. One of these challenges is the structural layout of the aircraft which includes the mounting of the engine to the wing-fuselage structure. In addition, the main landing-gear is located close to the engine and therefore it has been chosen to integrate this into the same structure, making it even more complex. The first steps regarding this structure has already been done by Voeten [44] and is shown in Figure 1.2 but a detailed design of the full structure has not been reached yet. The current design uses simplistic frame elements as overhead beams and joints are represented with kinematic couplings, which are not representing reality very well.

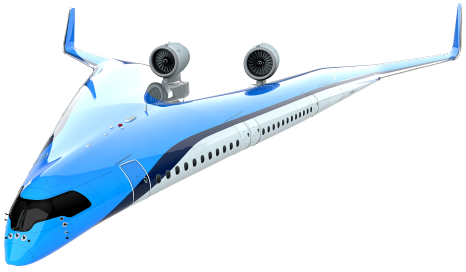

Figure 1.1: Visualisation of Flying V by E. Wallet. [45]

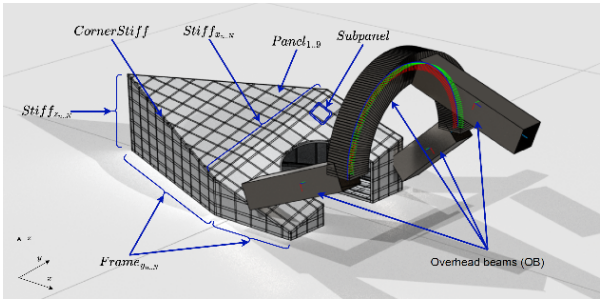

Figure 1.2: Engine mounting structure from Voeten [44], showing the simplistic overhead beams and lack of joints.

This research is a follow up on Voeten's research wherein a more detailed and optimized engine mounting structure is developed using an improved automated approach. This should give a better impression of the mass and thus viability of the current design and also result in a method that can be applied to other unconventional structures. Furthermore, the effect of the engine mounting structure on the crash-worthiness of the Flying-V is assessed, which should also give a better impression on the viability of the Flying-V.

The report starts with the research objective and question which needs to be answered in Chapter 2. In Chapter 3 the technical specifications of engine and landing gear are given. Furthermore, unique definitions of the engine mounting structure are explained and design choices and improvements are mentioned and supported. Chapter 4 contains the different load cases and locations which are used for the optimization. A detailed description of the model, code overview, post-processing and optimization method is given in Chapter 5. In Chapter 6 the criteria and finite elements model regarding crashworthiness are described. This chapter also contains an engine-impact model to analyse the possibility of impact after separation. The results of both the optimization and crash scenarios are given in Chapter 7. Conclusions based on these results are given in Chapter 8. Lastly, assumptions and recommendations are mentioned throughout this document, which can be found in listed format in Chapter C and Chapter 8 respectively.

2

Research Objective and Questions

In this chapter the purpose of the research is stated and motivated. Furthermore, questions are formulated which have to be answered in order to reach the research objective.

2.1. Research objective

The objective of this research is a follow up from previous research related to the Flying-V. Herein an automated design methodology for the engine mounting structure was developed. However, the full structure was not considered and the design methodology is only viable for a limited amount of design parameters. The goal of this research is thus similar as Voeten [44] but worked out more extensively. This means that the resulting engine mount should be lightweight and also fulfill all regulations and other set requirements. This way a mass efficient, safe and easily maintainable structure is ensured. From this the final research objective is as follows:

The goal of the research is the development of a certifiable and lightweight engine mounting structure and corresponding joints for the Flying-V which comply with all set requirements.

2.2. Research questions

In order to know when above described objective is reached a research question is formulated. Once this question is answered than the goal of the research is reached. This main research question is as follows:

How can a lightweight and certifiable engine mounting structure and corresponding joints be developed for the Flying-V which comply with all set requirements?

The main research question is quite complex and broad and therefore hard to answer accurately and structured instantly. For this reason the main research question is divided in sub-questions. The sub-questions that are needed to be answered are as follows:

- **What are the critical load cases?**
- **What are the regulations and requirements regarding engine mounting structures?**
- **What is the effect of a higher level on detail on the viability of the Flying-V?**
- **What is a suitable optimization method?**
- **What is the influence of the engine mounting structure on the viability of the design regarding crashworthiness?**

3

Design Improvements

In this chapter the initial designs of the overhead beams and corresponding joints are made which are optimised using the method described in Chapter 5. These designs are of moderate level of detail, this means that dimensions, general material choice and occasionally general fastening methods are specified. Specific details about fastening, such as bolt grades and dimension or type of welding, are not considered as part of this research but should be assessed in future research.

Recommendation 1 *Future studies should consider more in-depth material analysis and specific fastening details, such as fastener dimensions or grade.*

Furthermore, the global design of the overhead beams of Voeten [44] is chosen, also shown in Chapter 3.2, as various concepts were already considered and discussed in his research. The current design is deemed to be the most efficient while also taking all the requirements into account.

3.1. Technical specifications

The engine that has been chosen for the Flying-V is the same engine used in the relevant family member of the reference aircraft, the Airbus A350. As determined by Oosterom [31], the Flying-V is capable of family design and therefore it has been chosen to design for the worst case, which is the FV-1000 variant. This aircraft uses the heavier Rolls Royce Trent XWB-97 engine shown in Figure 3.1. This engine has a length, fan radius and total radius of 5.812, 1.5 m and 2 m respectively, can provide a maximum take-off thrust and continuous thrust of 431.5 kN and 369.6 kN respectively with a bypass ratio of 9.6:1 and has a raw engine mass of 7549 kg [19] [14]. However, during operation, the engine does include other components such as a nacelle and fluids which means that 7549 kg is an underestimate of the total mass. Therefore, due to lack of additional information, a mass of 10950 kg will be used for the engine mass which was found by Oosterom [31] using empirical relations by Torenbeek [39].

Assumption 1 *The mass of the Rolls Royce Trent XWB-97, including nacelle, is 10950 kg.*

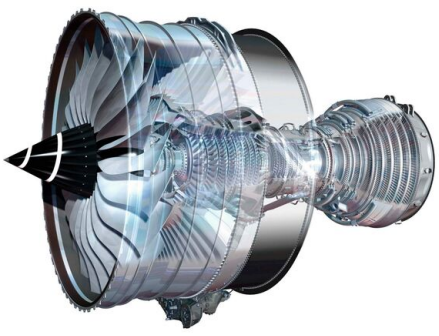

Figure 3.1: Visualisation of a Rolls Royce Trent XWB engine from Janes. [19]

From Figure 3.1 it can be seen that the engine is mounted at two positions, wherein both the front and the aft mount have three connection points.

Another point of interest is the center of gravity of the engine, as this is the point whereupon most of the loads act. This information is not available and therefore an educated guess has to be made. In this research the same assumption made by Voeten [44] and Dotman [11] is used, which is that the center of gravity is in the center at 1/3rd of the engine's length due to the size of the fans in the front and position of the gearbox and pumps.

Assumption 2 *The center of gravity is in the center at 1/3rd of the engine's length.*

As both the mass and the position of center of gravity are determined using educated guesses these should be included in a sensitivity analysis if time allows.

The initial landing gear for the Flying-V is designed by Bourget [4]. Bourget determined the bogie setup, tyre selection, location, and retraction system based on aerodynamics and stability of the aircraft. In the research three types of landing gear configurations were considered which differ in wing dihedral. For this research it has been chosen to use the floor height of 5.5 m configuration as it is the moderate case. This configuration shows improvements in terms of mass, volume and maintenance compared to the default case but does not worsen the already bad stability as much as the max dihedral configuration. The resultant mass (m_{mlg}) and strut length (L_{mlg}) of a single main landing gear are:

$$m_{mlg} = 6400\ kg \qquad L_{mlg} = 5.3\ m$$

The locations of both the engine and landing gear have been slightly altered by Voeten [44] for structural reasons. Which are for the FV-900 configuration at:

$$\begin{array}{lll} x_{engine} = 31\ m & y_{engine} = 4.2\ m & z_{engine} = 0.8\ m \\ x_{landing} = 29.3\ m & y_{landing} = 4.2\ m & z_{landing} = -0.658\ m \end{array}$$

This results in 59% and 55.8% of the total aircraft's length for the engine and landing gear respectively in x-direction and 14% of the aircraft's span in y-direction.

The effect of these changes on the aerodynamic performance and stability of the aircraft have not been investigated and will not be done within this research.

Recommendation 2 *The effects on stability and aerodynamic performance due to change in location of landing gear and engine should be investigated in future research.*

3.2. Definitions

As mentioned in the introduction, the Flying-V is unprecedented and so is the structure to mount the engine and landing gear. This means that the usual nomenclature of components does not hold in all cases and to avoid confusion a clear definition for each part of the structure is given in this section. In Figure 3.2, an altered image is shown of the design as made by Voeten [44], wherein with red the new abbreviations of the nomenclature are added. It should be noted that the curved beam has been split into two different objects in the new design.

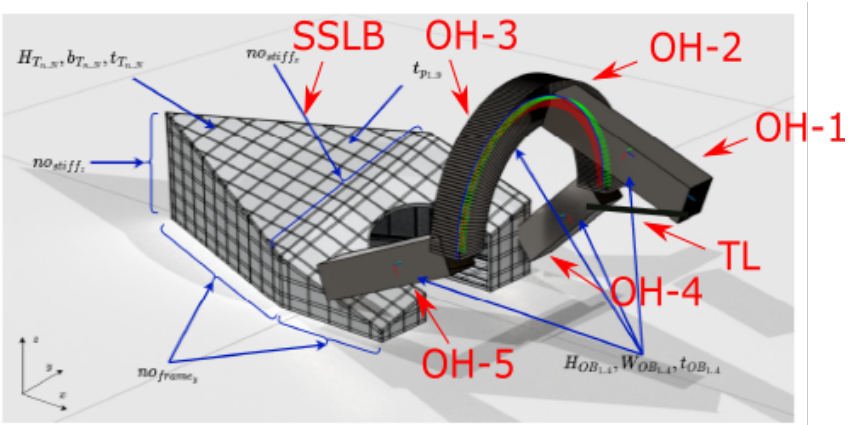

Figure 3.2: Engine mounting structure with definitions altered from Voeten. [44]

In the research of Voeten, the focus was on the skin-stiffened landing gear box (SSLB), while for this research the focus will be mainly on the overhead structure, which contains of five different beams, Overhead-1 (OH-1) to Overhead-5 (OH-5). Additionally, the thrust link (TL) is added for clarification as one might consider OH-1 to also be a thrust link.

3.3. Loadpaths at engine

Each of the engine mounts carry different kind of loads into the structure. In a conventional engine mounting structure this will be the vertical and side loads for the front engine mount, the vertical, side and torque loads for the aft engine mount and the thrust loads through the thrust link to the aft engine mount [34] [6]. For this new design it might be desired to have the front engine mount to carry most of the loads as this reduces the amount of loads through OH-1 which results in a lighter structure. However, it is assumed that the engine is not able to transfer these loads to the front engine mount or the aft mount and therefore no changes are made to the types of loads the mounts are carrying.

Assumption 3 *The Trent XWB-97 engine is not able to transfer different kind of loads to the mounts as it does in existing aircraft.*

This means that OH-1 will take bending moments in two directions and both compressive and tensile loads due to the thrust and thrust reverser respectively. Consequently, OH-2 and OH-3 will be mainly under shear and bending moments and both OH-4 and OH-5 under bending moments and compressive and tensile loads.

3.4. Material choice

The material choice is done qualitatively. In previous research of Voeten [44] a similar approach was used and Ti-6Al-4V was chosen for the overhead beams based on the creep resistance, lower conductivity and higher stiffness and strength of the material. However, this material also has a higher density and is more expensive compared to Al-7475 [3], which is mostly used in aircraft structures. Furthermore, most of the loads are subjected at the front of the engine, where the relative cold fan is located as shown in Figure 3.3. Only the aft part of the engine is where the elevated temperature might cause issues in the case of aluminium. For these reasons it has been decided that the part from the skin-stiffened box to the front mount will be made from Al-7475 whereas the part between the front mount

and aft mount will be made from Ti-6Al-4V. Upon optimization it remains to be checked if this decision has been favourable in terms of weight and costs or that it is more beneficial if the overhead beams are made of Ti-6Al-4V. It should be noted that the Young's modulus and yield strength of Ti-6Al-4V lowers to 90 GPa and 600 MPa respectively at 400 °C [3].

A similar approach have been made regarding the joints. As the function and conditions for the joints between the skin-stiffened box and overhead beams are similar, a single material is chosen. The chosen material is Al-7475 as it is lightweight, easy processable, cheap and there are no issues regarding temperatures.

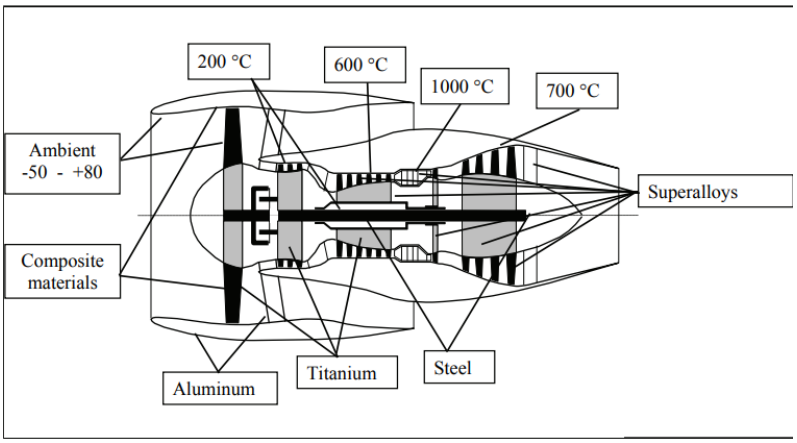

Figure 3.3: Temperature distribution and materials for a turbofan, showing the relatively cold front and hot rear connections. [35]

Titanium and aluminium have a potential difference, which will cause the aluminium alloy to corrode, it has been decided to keep these materials as it can be solved in various ways such as applying a non-conductive layer between the joint [32]. It is of importance that this is going to be investigated more deeply in future research as corrosion pits are one of the main sources of fatigue cracks in engine mounting structures. In various instances connection bolts and mounts have been found which were subjection to corrosion [16].

Recommendation 3 *Future research should investigate solutions for the possible corrosion between aluminium and titanium.*

The material properties of Al-7475 and Ti-6Al-4V are noted in Table 3.1 below.

Table 3.1: Material properties of Al-7475 and TI-6Al-4V from [3].

	Ti-6Al-4V	**Al-7475**
Young's modulus (GPa)	115	71.8
Yield strength (MPa)	1050	429
Poisson ratio (-)	0.360	0.337
Density (kg/m^3)	4420	2800

3.5. Overhead beams

In this section an initial design is made for the different parts of the overhead structure. No change in general design has been made as the requirement of an overhead structure comes from the industry. Engineers must be able to perform maintenance at all possible airports, which means that the engine must be able to be removed without the need of special equipment, requiring the engine to be supported from above. However, a design can be made of these beams themselves. All beams of this overhead structure encounter the same kind of loads, getting larger the closer to the skin-stiffened landing gear box. This means that all parts of the structure will be of the same variant with different dimensions. This variant should have a large second moment of area with variable values in two directions and a large

enough area for the axial loads. Based on this a skin stiffened box structure has been chosen as it is deemed the most mass efficient method to satisfy the previous mentioned requirements. In addition, it has the advantage of having enough space for cables, fuel ducts etc..

This structure will contain stiffeners, ribs and skins with varying dimensions, however it has been chosen to choose one single type of design for all these parts for simplicity. This means that in future research the structure may be further optimized by having e.g. two different stringer types in the structure.

Recommendation 4 *In future studies the structure may be further optimized by having different stiffener or rib designs at different places.*

For manufacturing reasons, the angled corner and T-stiffener are chosen for this design. These stiffeners allow multiple manufacturing options to be open as it can both be riveted and welded if necessary. The angled corner can be used to connect the various plates to each other. The ribs will be made of sheet metal, with a single circular or oval shape cut out. Around this hole a stiffening element, similar to an angled corner is placed. This results in a rib that is relatively easy and cheap to manufacture various sizes of and is also easy to install. The ribs are placed perpendicular to the central axis of the beam. Figure 3.4 gives an impression of the resultant cross section of an overhead beam.

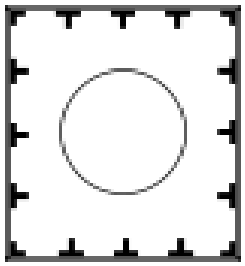

Figure 3.4: Example of the cross section of an overhead beam.

In order to reduce loads in the overhead beams they have to be located as close to the engine as possible while still allowing some clearance for the (de-)installing of the engine. This clearance is set at a minimum of 5 cm, meaning that, apart from the engine mounts, the overhead beams can not be within 5 cm of the engine. Furthermore, the inlet of the engine may not be obstructed by the beams as this has a negative influence on the efficiency of the engine.

3.6. Skin-stiffened landing gear box

The original skin-stiffened landing gear box design is from Voeten [44]. This design consists of 8 stiffened plates and is shown in Section 3.2. This part contains the connections of the landing gear and engine mounting structure and transfers the loads into the trailing edge spar.

However, the design, as designed by Voeten, is not sufficient for the current research. Firstly the current design is not taking into account the connection of OH-4 and OH-5 with the landing gear box. Furthermore, the loads will be transferred into the spar at the location of the plates, which means that the connection plate itself has little function, while adding mass. For these reasons some adjustments have been made to reach a viable design. The adjustments made are:

1. Openings for the joints of OH-4 and OH-5.
2. Limit stiffeners such that they do not intersect with the joints of OH-4 and OH-5.
3. Removal of the plate at the location for the spar.

Due to the time limit of the research other necessary or beneficial adjustments have not been made but are listed below for future consideration.

4. The skin-stiffened landing gear box should be made bigger as the used engine in the CAD model is smaller than the Trent XWB-97 engine.

5. Making the upper, most inclined, plate single curved. This can greatly reduce the amount of empty space at the spar-side of the box, reducing the total mass.

Recommendation 5 *Adjustments 4 and 5 should be considered in future research.*

A figure of the altered design, in non-optimized manner is shown in Figure 3.5.

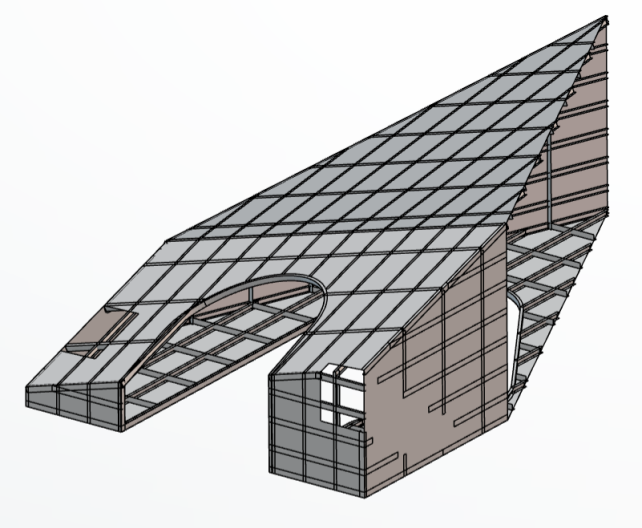

Figure 3.5: Visualisation of the non-optimized altered skin-stiffened landing gear box.

3.7. Joints

In this section the initial designs of the engine mounts and the joints between overhead beams and the landing gear skin-stiffened box is described. These joints were in the design of Voeten [44] non-existent and were represented with a rigid coupling. The joint of the skin-stiffened landing gear box and the spar has been disregarded completely.

Recommendation 6 *The connection between the skin stiffened landing gear and rear spar should be investigated in future research.*

3.7.1. Thrust links and engine mounts

The standard Trent XWB-97 engine contains two attachment points for thrust links. These links carry the thrust loads into the engine mounts. As described in previous chapter it is assumed that the type of loads through the engine mounts do not change with respect to the current design. This means that the design of both thrust links and engine mounts will be excluded from this research. It will however be investigated if a future engine mount needs a separation mechanism for safe engine release in case of emergency.

Recommendation 7 *In future research the design of the thrust links and engine mounts should be taken into account.*

3.7.2. Joints

The connection between the overhead beams will be done via an additional part, herefrom called joints. These joints eases the assembly of the structure while also ensuring that the fasteners undergo the desired, shear, loads. The first joint connects OH-1 with OH-2 and OH-3 and also accommodates the attachment point for the front engine mount. OH-2 and OH-3 are connected via another joint to OH-4 and OH-5 respectively. OH-4 and OH-5 are individually connected using another joint to the skin-stiffened landing gear box. This joint is designed such that it is attached at the side, bottom and top panel. This ensures that the local moment induced by the thrust or gravity is solved by the top and bottom panel. For future studies it might be useful to combine the to be designed landing-gear connection with this joint. A visualisation of these joints, non optimized, are shown in Figure 3.6 from left to right in the order that they are mentioned.

Recommendation 8 *Future studies should consider to combine the to be designed landing-gear connection with the skin-stiffened landing gear joints.*

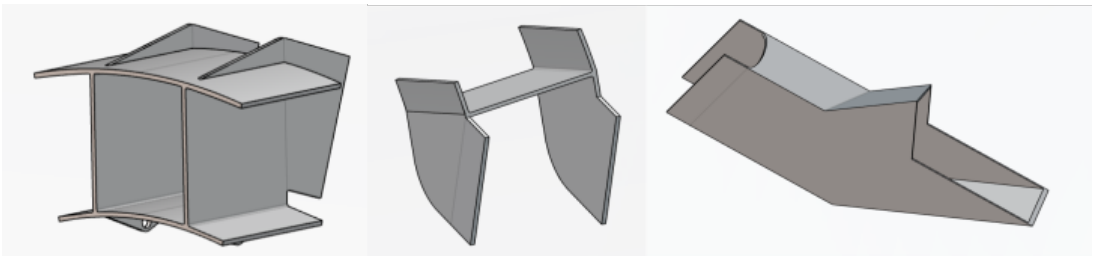

Figure 3.6: Visualisation of the non-optimized joints.

3.8. Assembly

Above design decisions lead to the designed, non-optimized, engine mounting structure as shown in Figure 3.7.

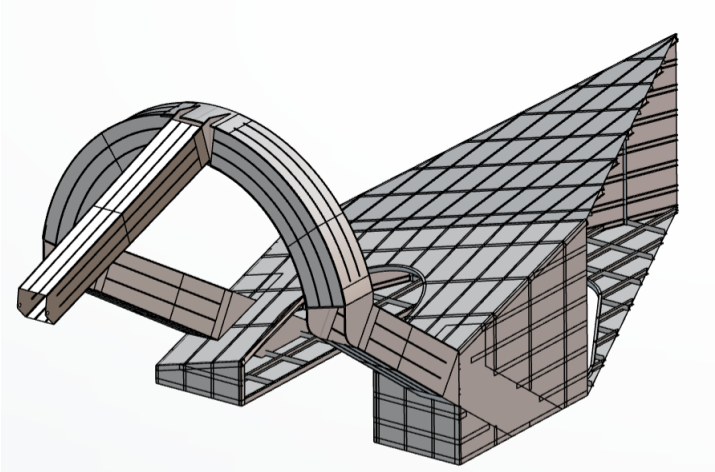

Figure 3.7: Visualisation of the total, non-optimized, assembly after all design alterations.

4

Loads

This section contains information about the load cases that the engine mounting structure will endure during its life time. From all these load cases the most critical ones are determined and chosen to size the design. Furthermore, the magnitude, location and orientation of these loads introduced by the engine and landing gear are determined.

4.1. Load cases

In previous research regarding the Flying-V different lists with load cases have been considered. The most relevant list of these load cases lists has been made by Voeten [44] and is shown in Table 4.2. This list is thought to be complete and will thus not be extended within the present research. From this list Voeten has determined the most critical load cases in order to save computation time. This was done by comparing the expected magnitude and direction of loads of each loadcase, reducing the list to the 7 load cases presented in Table 4.1, to be used for sizing. Afterwards Voeten concluded that of these critical load cases only TO-04, LD-06, LD-08 and CR-05 have significant effect on the final design. Although the addition of details in the current design might result that the other load cases become more prominent, it has been decided to continue with these 4 critical load cases to save additional computational time. This is to compensate the additional run time the model requires due to the addition of the details. The other three load cases, CR01, CR02 and TO05, will be used as verification cases by checking the viability of the optimized design.

Different loads are applied n each of these different cases, an overview of the applicable loads for each case are shown in Table 4.1. Herein are T_{cruise} and T_{max} the cruise thrust and maximum thrust, which are together with the maximum failure loads, Fy_{fail} and Fz_{fail} determined in Section 4.3. The loads by the landing gear, F_x, F_y and F_z, are determined in Section 4.2. The factors in front of the F_z loads in the F_x and F_y columns result from the regulations, more specifically CS 25.479 and CS 25.485. [13]

Table 4.1: Critical load cases and their corresponding loads.

No.	Nz	Tx	Ty	Tz	Fx	Fy	Fz
CR-01	2.5	T_cruise	0	0	N/A	N/A	N/A
CR-02	-0.75	T_max	0	0	N/A	N/A	N/A
CR-05	1	T_cruise	Fy_fail	Fz_fail	N/A	N/A	N/A
TO-04	Nz_cos(t)	T_max	0	0	0.25*Fz_cos(t)	0	Fz_cos(t)
TO-05	Nz_28R(t)	T_max	0	0	0.25*Fz_28R(t)	0	Fz_28R(t)
LD-06	Nz_OG(t)	0	0	0	0.25*Fz_OG(t)	0.4*Fz_OG(t)	Fz_OG(t)
LD-08	Nz_Lat(t)	0	0	0	0.25*Fz_Lat(t)	0.8*Fz_Lat(t)	Fz_Lat(t)

Table 4.2: All possible load cases applicable to the engine mounting structure as determined by Voeten [44], with the most critical loadcases colored red, less critical pink and not critical blank.

No.	Operation	Critical Load case	Load case description	Weight	Analysis type	Nz (g)	Vz ground [m/s]	Loading condition
CR-01	Cruise	Y	Maximum load factor cruise	MTOW	Static	2.5	0	Limit
CR-02	Cruise	Y	Minimum load factor maximum thrust	MTOW	Static	-0.75	0	Limit
CR-03	Cruise	N	Failure engine stop	MTOW	Dynamic	1	0	Ultimate
CR-04	Cruise	N	Failure engine start	MTOW	Dynamic	1	0	Ultimate
CR-05	Cruise	Y	Failure Engine max imbalance (fan blade loss)	MTOW	Static	1	0	Limit
CR-06	Cruise	N	Minimum load factor	MTOW	Static	-1	0	Limit
TO-01	Take-off	N	Maximum thrust after TO	MTOW	Static	1.875	0	Limit
TO-02	Take-off	N	Max thrust during TO	MTOW	Dynamic	Dynamic model S/A	0	Limit
TO-03	Take-off	N	Aborted TO (only main gear)	MTOW	Dynamic	Dynamic model S/A	0	Limit
TO-04	Take-off	Y	Most severe bump (1-cos) just before aborted TO with maximum thrust	MTOW	Dynamic	Dynamic model S/A	0	Limit
TO-05	Take-off	Y	Most severe bump San-Fransisco 28R just before aborted TO with maximum thrust	MTOW	Dynamic	Dynamic model S/A	0	Limit
LD-01	Landing	N	Level-landing sea level 3-point	MLW	Dynamic	Dynamic model S/A	-3.05	Limit
LD-02	Landing	N	Level-landing high alt 3-point	MLW	Dynamic	Dynamic model S/A	-3.05	Limit
LD-03	Landing	N	Tall-down landing sea level 2-point	MLW	Dynamic	Dynamic model S/A	-3.05	Limit
LD-04	Landing	N	Tall-down landing high alt 2-point	MLW	Dynamic	Dynamic model S/A	-3.05	Limit
LD-05	Landing	N	One gear landing sea level 1-point	MLW	Dynamic	Dynamic model S/A	-3.05	Limit
LD-06	Landing	Y	One gear landing high alt 1-point	MLW	Dynamic	Dynamic model S/A	-3.05	Limit
LD-07	Landing	N	Lateral drift landing sea level 2-point	MLW	Dynamic	Dynamic model S/A	-3.05	Limit
LD-08	Landing	Y	Lateral drift landing high alt 2-point	MLW	Dynamic	Dynamic model S/A	-3.05	Limit
LD-09	Landing	N	Braked roll (only main gear)	MLW	Dynamic	Dynamic model S/A	-3.05	Limit
LD-10	Landing	N	Rebound landing	MLW	Static	Dynamic model S/A	-3.05	Limit
LD-11	Landing	N	Failure 1 impact on gear	MLW	Dynamic	N/A		Ultimate
LD-12	Landing	N	Failure 2 impact on plane	MLW	Dynamic	N/A		Ultimate
GR-01	Ground	N	Reversed braking	MRW	Dynamic	0	0	Limit
GR-02	Ground	N	Towing loads	MRW	Static	0	0	Limit

4.2. Landing gear loads

The loads introduced by the landing gear have been analysed by Voeten [44]. In this study by Voeten, a simplified approach is used by assuming a rigid body single degree of freedom system for the landing gear. Voeten also acknowledges that there are more detailed approaches out there which will result in more accurate values for the loads. However, these require experimental data which could not be gathered in the time-span of his research. The current research has a slightly higher level of detail as Voeten but has a similar time restriction. It is thought that these more accurate values would not add much value to this research and therefore it has been chosen to use the values for the loads introduced by the landing gear as found by Voeten. This means that the recommendation already made by Voeten holds.

Recommendation 9 *The loads introduced by the landing gear should be evaluated with more detailed methods in future studies.*

The resultant landing gear forces from the single degree of freedom model for the various types of runway are shown in Figure 4.1

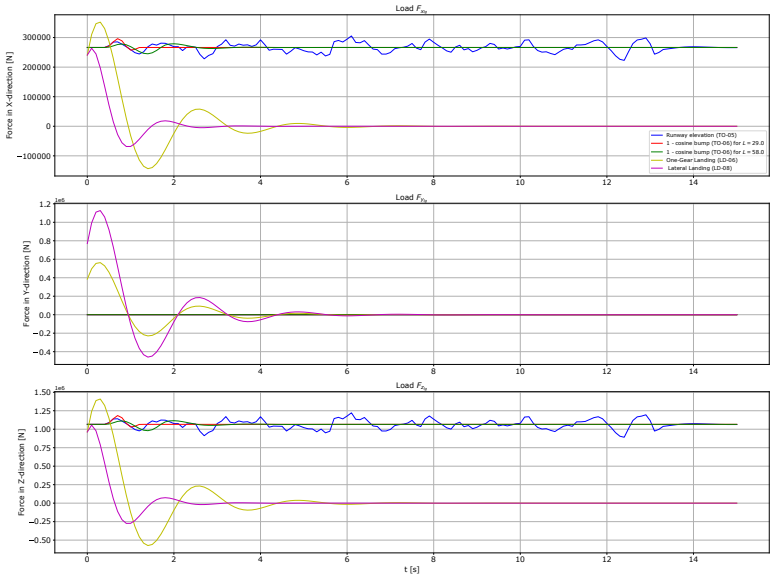

Figure 4.1: Landing gear forces determined by Voeten [44], showing the applied forces per load case and emphasising the criticality of LD-06 and LD-08.

The resultant moments, shown in Figure 4.2, are determined by multiplying the found loads in X and Y-direction with the maximum stroke minus the occurring stroke.

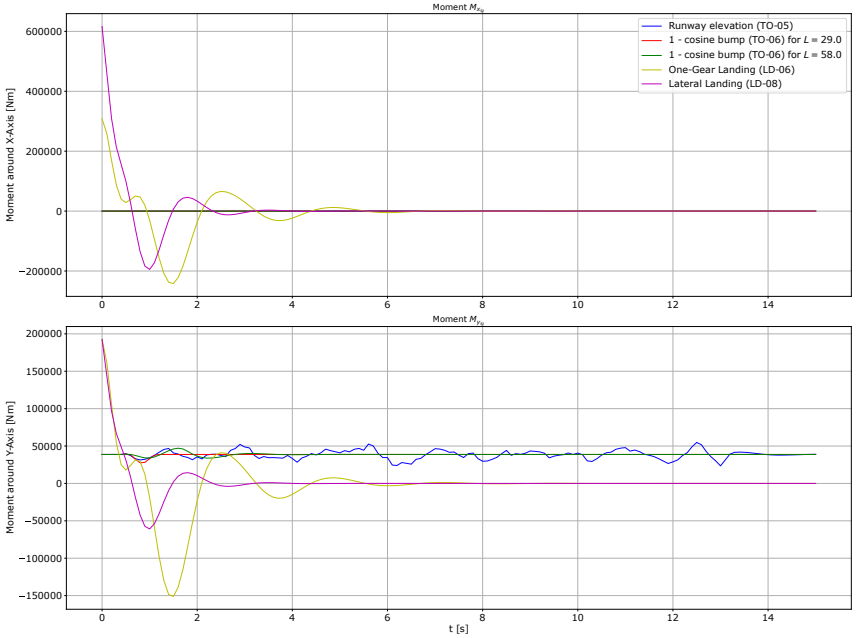

Figure 4.2: Landing gear moments determined by Voeten. [44], showing the applied moments per load case and emphasising the criticality of LD-06 and LD-08.

It should be noted that the negative forces and moments depicted in above figures are not possible in real life as the runway can not impose a tension force on the landing gear. However, for conservative reasons, Voeten has chosen to conserve these values.

4.3. Engine loads

The engine is next to the landing gear the main contributor of loads to the engine mounting structure. Therefore, the loads during both normal operations and those occurring upon engine failure are deter-

mined in this section.

4.3.1. Operational loads

The operational loads imposed by the engine during normal operations are the thrust, drag, lift and the gravity. Whereof the lift and drag are small compared to the thrust and gravity and will therefore be ignored in this research.

Assumption 4 *The drag and lift generated by the engine can be ignored during operation.*

The gravitational load acting on a single engine is:

$$F_g = 10950 \cdot 9.81 = 107409.5\ N \tag{4.1}$$

The thrust of this engine varies during the flight and from datasheets of Janes [19] and EASA [13] it is known that the maximum thrust at take-off which the engine can provide is 431.5 kN and 369.6 kN continuously.

During cruise, the thrust is equal to the drag and the lift is equal to the weight. The total drag of the aircraft can be found using Equation 4.2, considering the MTOW of 275000 kg and L/D of 21.2 for the FV-1000 [31].

$$D = \frac{MTOW \cdot 9.81}{L/D} = \frac{275000 \cdot 9.81}{21.2} = 127252.4\ N \tag{4.2}$$

Which results in the thrust of a single engine during cruise of:

$$T = \frac{D}{2} = \frac{127252.4}{2} = 63626.2\ N \tag{4.3}$$

The nacelle for this engine also has cascade thrust reversers of the blocker door type [2]. This means that, using the value of the bypass ratio of 9.6:1, the reversed thrust load is approximately 30% of the thrust load [30]. Which means that at maximum a reverse thrust of 129.45 kN can be expected.

Next to these operational loads the engine mount also have to handle side loads, which are described in CS 25.363. This load is independent of other flight conditions and is equal to the maximum load factor in yawing condition but no less than a factor of 1.33. The maximum load factor in yawing condition can be calculated by calculating the centrifugal force during the maximum yawing rotational velocity. The maximum yawing rotational velocity could not be found for the Flying-V nor the Airbus A350. Therefore, an assessment is done if the rotational velocity to reach a load factor of 1.33 is reasonable. Herein is m the mass of the engine, r the distance from the center line to the engine.

$$\omega = \sqrt{\frac{1.33 \cdot m \cdot 9.81}{m \cdot r}} = \sqrt{\frac{1.33 \cdot 9.81}{4.2}} = 1.7625\ rad/s$$

This is a unrealistic high value which means that the load factor of 1.33 is highly likely to not be reached, therefore the minimum side load on the engine mount, whereupon no failure may occur is;

$$F_{side} = m \cdot 9.81 \cdot 1.33 = 10950 \cdot 9.81 \cdot 1.33 = 142879.35\ N \tag{4.4}$$

This value is lower than the loads due to blade loss, described in next section, and will therefore not result in a more critical load case.

During operation the engine also applies moments onto the mounts, this coming from the engine torque and gyroscopic loads due to manoeuvres of the aircraft. In order to calculate these moments additional information is needed, such as engine inertia and manoeuvre rates of the aircraft. This information is, again, not available. Using the fact that a commercial aircraft has relative small manoeuvre rates it is assumed that the other load cases are of higher concern even while these values, as described in CS 25.361 and CS 25.371 should be combined with normal flight conditions.

Assumption 5 *Engine torque and gyroscopic loads are small compared to the other load cases.*

Recommendation 10 *In future studies the structure should be reassessed by including the engine torque and gyroscopic loads in the load cases.*

4.3.2. Engine failure loads

During flight a part of the engine might fail which causes additional loads. In the regulations by EASA, CS-25.362, is stated which failures and in what extend this should be accounted for.

(a) For engine mounts, pylons and adjacent supporting airframe structure, an ultimate loading condition must be considered that combines 1g flight loads with the most critical transient dynamic loads and vibrations, as determined by dynamic analysis, resulting from failure of a blade, shaft, bearing or bearing support, or bird strike event. Any permanent deformation from these ultimate load conditions should not prevent continued safe flight and landing.

(b) The ultimate loads developed from the conditions specified in paragraph (a) are to be:

- *multiplied by a factor of 1.0 when applied to engine mounts and pylons; and*
- *multiplied by a factor of 1.25 when applied to adjacent supporting airframe structure.*

In the corresponding AMC is stated that it is most likely that blade loss causes the most severe loads but that all cases should be checked for each new engine. In previous work by Voeten [44] the blade loss case has been analysed which resulted in a maximum centrifugal load of 256354 N. However, Voeten did not analyse the loads generated by the other specified failures. Additional failures which should be considered according to CS-520(c)(2) are the failure of shaft, failure or loss of bearing or bearing support and bird ingestion. Furthermore, it is stated that these loads should be determined by dynamic analysis. Such an analysis requires a validated engine model supplied by the engine manufacturer, which is not available for this research. For this reason it has been considered that, for the current level of detail, a static load occurring during blade loss is the most critical engine failure load.

Assumption 6 *A static load of 256354 N during blade loss is the most critical load during failure.*

Recommendation 11 *In future studies the dynamic loads of blade loss, shaft failure, failure or loss of bearing/bearing support and bird ingestion needs to be determined.*

4.4. Load location

In this section the location of previous determined loads are established and shown in Figure 4.3 for the engine and Figure 4.4 for the landing gear.

There is no direct information available of the center of thrust for the Trent XWB engines. This means that the location should be approximated for this research. Since thrust (T_x) is generated by moving large amount of air, this is mostly done by the fan due to the large by-pass ratio of the engine. In addition, it is assumed that the center of thrust is along the central axis at the center of the fan.

Assumption 7 *The center of thrust is along the central axis of the engine at the center of the fan.*

The loads due to imbalance (T_y,T_z), calculated by Voeten [44], is located at the fan as those blades create the largest centrifugal loads. The remaining loads, such as the gravitational (F_g) or side load (F_{side}), are located in the center of gravity of the engine. Remind, that this is assumed to be at 1/3rd of the engine length.

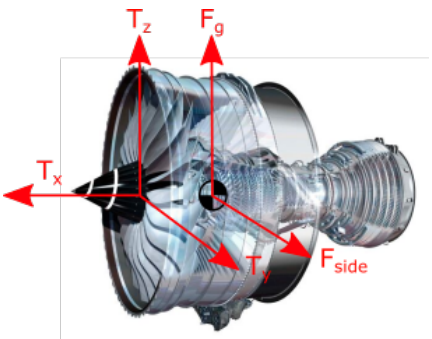

Figure 4.3: Trent XWB engine with location of loads, adapted from Janes. [19]

The calculated moments in Figure 4.2 are the perpendicular loads at the connection point of the wheels multiplied by the length of the shock absorber at any given time. This means that both the force and moment should be applied after the shock absorber instead of at the connection point of the wheels. This means that all loads (F_x,F_y, F_z) and moments (M_x,M_y) are applied after the shock absorber as shown in Figure 4.4. The used location is approximated using the CAD model of the landing gear by Voeten.

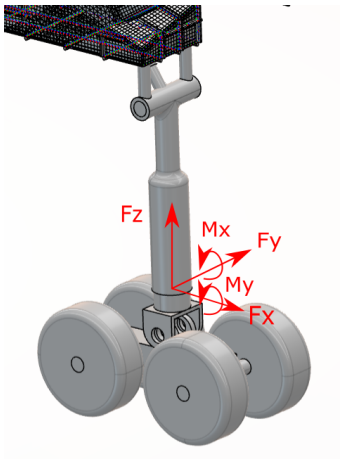

Figure 4.4: Visualisation of the landing gear with location and direction of loads and moments.

5

Model and Post-processing

This chapter starts with a simplification of the model by reducing the number of variables to save computational effort. Afterwards a general overview of the code is given which automatically analyses and optimizes the design according to methods later discussed within this chapter. Lastly, this chapter also includes an explanation of the finite element models used for the simulations.

5.1. Reduction of variables

In order to reach an optimized structure it is of importance to identify the parts which have a significant influence on the final mass and structural performance. This section contains an identification of the variables which can be fixed to save additional computation time without having a significant influence on the final mass.

Stiffeners

Apart from the length, widths, thicknesses and shape of the cross section of the stiffener also the spacing and number of stringers can be varied. This means that each additional stiffener, depending on shape of the cross sections, adds a minimum of 5 variables and each plate an additional 1 for the number of stiffeners. Only the length of all these variables is initially fixed due to other geometry. In order to improve manufacturability and save a lot of computational time it has been chosen to use a fixed cross sectional shape and make the spacing between the stringers equal. This reduces the minimum number of variables for a single plate to 3. In order to reduce the number of variables even further, it has been chosen to group the stiffeners in each direction. This means that the number of stiffeners and their cross sectional properties are constant for stiffeners spaced in the same direction for each part. Additionally, all corner stiffeners are grouped, reducing the minimum number of variables for the stiffeners to 8 for each overhead beam and 11 for the skin-stiffened landing gear box.

Skin

Each plate has a width, length and thickness whereof the width and length are fixed due to geometry. The thickness of the full plate is considered to be constant over the area, which means that 4 variables for each overhead beam and 7 variables for the skin-stiffened landing gear are added.

It should be noted that it is possible to have a gradually changing thickness along the plate by dividing the plate mesh into submeshes. This is not considered for the current research as the time is limited and the reduction of mass is thought to be relatively small.

Recommendation 12 *In future studies a gradually changing thickness of the skin should be considered.*

Joints

The joints used in this design are quite complex shapes but their dimensions are mainly fixed by the overhead beams and skin-stiffened landing gear box. The only dimensions which are free are the internal thicknesses. In order to save computational effort it has been chosen to group these thicknesses

into one single parameter.

Each of above made decisions is considered to have limited impact to the general optimisation and final mass of the product. However, for a fully optimised design these simplifications should be removed.

Recommendation 13 *In future studies each fixed variable to save computation time should be made free.*

5.2. Design workflow

In this section a general overview of the code is made and explained what each part of the code does. The model uses Object Oriented Programming (OOP). The code is started from the MainEditor which connects Python to 3DExperience and opens all the required files. The initialisation of the parameters is done in the Optimiser which alters the model accordingly in each parts own Modifier file and meshes it using either MeshSFD or MeshSolid depending if it is a skin-stiffened structure or a solid joint. After meshing the Optimizer starts the simulation using SimulationEditor, which also creates folders for the raw and processed data. After the simulation is done, the raw data is processed in the Post-Processor to Margins of Safety (MoS) per failure mode per element. These are further processed in Optimizer, which is explained in Section 5.5. An overview of above is shown in Figure 5.1.

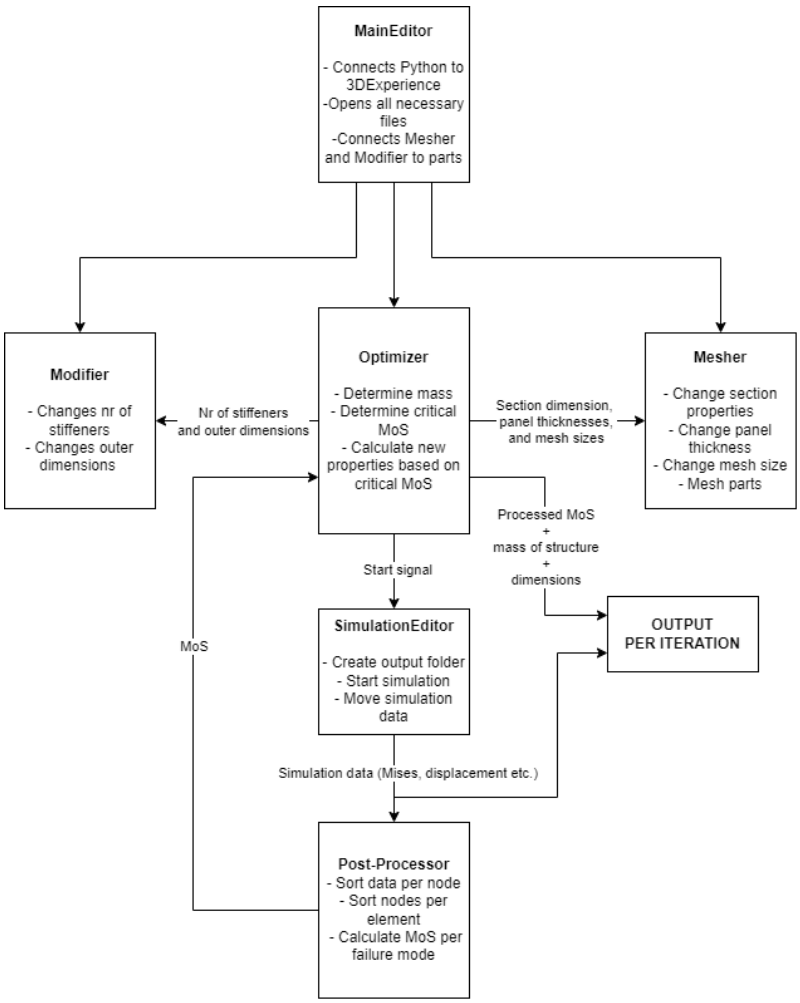

Figure 5.1: Overview of the automation code, showing the functions of each class and the flow of data between the various classes.

As explained in previous sections the structure has various parts with many variables. Some of these variables overlap between parts, which means that if one variable is changed all relevant parts need to be updated. Furthermore, it should be build up in a way that it is easy to add or remove parts or variables in the future. For this reason a tabular method has been chosen, which will be generally explained. Firstly, all the variables and the variables corresponding to the parts are noted as shown below.

$$Variables = [V1, V2, V3, V4, V5]$$
$$Parts = [P1, P2, P3]$$

$$P1 = [V1, V2]$$
$$P2 = [V1, V3, V4]$$
$$P3 = [V2, V4, V5]$$

Using the information above, three automated tables are made. Table A consists of the names of the variables, Table B consists of the values of the variables and Table C consists of zeros and ones. A zero value in Table C means that the variable has remained unchanged and an one if the variable has been changed. Table A is used to find the location of the value which needs to be changed in Table B, while Table C allows the program to only update the necessary parts, saving computation time. An example of the tables is made using above used variables and parts and shown in Table 5.1. In this case variables $V1$ and $V3$ have been altered while the other remain the same.

Table 5.1: Table A, B, and C from top to bottom respectively, showing the method used to take dependencies between parts into account.

	V1	**V2**	**V3**	**V4**	**V5**
P1	V1	V2	None	None	None
P2	V1	None	V3	V4	None
P3	None	V2	None	V4	V5

P1	20	10	None	None	None
P2	20	None	20	30	None
P3	None	10	None	30	15

P1	1	0	0	0	0
P2	1	0	1	0	0
P3	0	0	0	0	0

In the code a distinct difference have been made between inner and outer variables. Inner variables are variables which have no influence on the outer dimensions such as number of ribs and stiffeners and their dimensions. For these variables a similar tabular approach have been used for consistency, but these remain separate, independent, tables.

5.3. Finite element model

In this section a more detailed description of the finite element model depicted in Figure 5.2 is described. This description contains the type of elements used and the connections between loads and structure for the different loadcases.

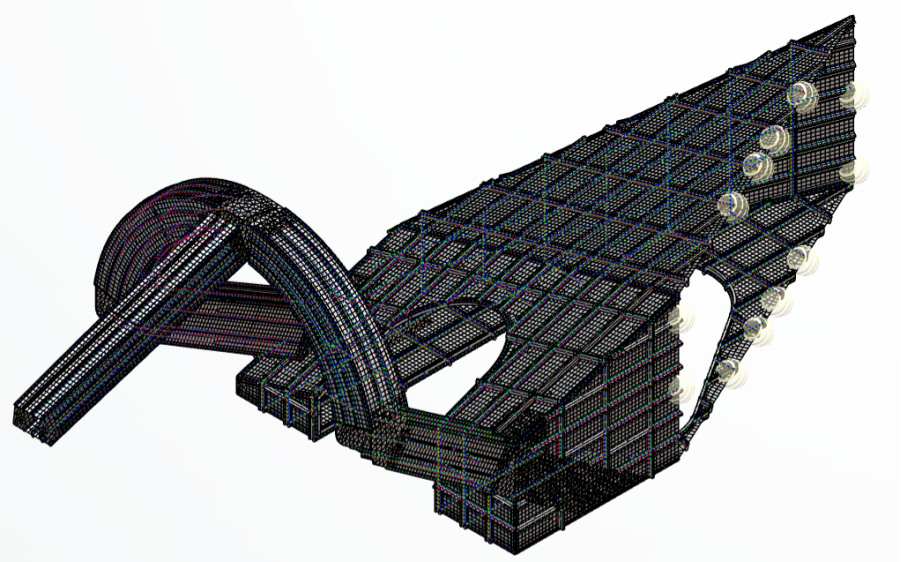

Figure 5.2: Visualisation of the FE model of the engine mounting structure used for the optimization of the structure, showing the clamped boundary condition.

5.3.1. Element types

The FE model, shown in Figure 5.2, has a total of three different element types. The panels are simplified to a 2D quadratic surface mesh with a shell section property and the stiffeners to a 1D coating mesh with a beam section property. The joints are not simplified and are represented with a tetrahedron mesh with a solid section property. These element types have been chosen in such a way that the computational effort is reduced without having a big impact on the results. This also means that when the design goes to a greater level of detail that the chosen element types might not suffice.

Assumption 8 *Stiffeners and panels can be simplified to 1D coating and 2D shell elements without having a large effect on the results.*

Sectional properties

The 3DExperience software has a set of the most used beam profile sections, which include the used T-section and angled corner, wherein the dimensions can directly be substituted. However, it is not intuitive to rotate the beam sections to the desired orientation within the software using Python. For this reason a general beam profile section has been chosen and the profile properties, such as second moment of area, are calculated separately, rotated and substituted into the software. For the anti-clockwise rotation Equation 5.1 to 5.3 are used.

$$I_{xx'} = \frac{I_{xx} + I_{yy}}{2} + \frac{I_{xx} - I_{yy}}{2} \cos 2\theta - I_{xy} \sin 2\theta \tag{5.1}$$

$$I_{yy'} = \frac{I_{xx} + I_{yy}}{2} + \frac{I_{xx} - I_{yy}}{2} \cos 2\theta + I_{xy} \sin 2\theta \tag{5.2}$$

$$I_{xy'} = \frac{I_{xx} - I_{yy}}{2} \sin 2\theta + I_{xy} \cos 2\theta \tag{5.3}$$

5.3.2. Connections

The loads and masses are connected using a combination of rigid couplings. Herein a distinction is made for the loadcases with extended (TO-04, TO-05, LD-06 and LD-08) and retracted landing gear (CR-01, CR-02 and CR-05). In both cases the coupling at the engine remain the same. Herein are all loads coupled to the back of OH-1 and the central insert except for the thrust which is only coupled to the back of OH-1 as discussed in Section 3.3. These couplings are shown in Figure 5.3, the location of each load in the figure can be found in Figure 4.3.

Assumption 9 *The connections represented by couplings are assumed to be relatively rigid compared to the rest of the structure*

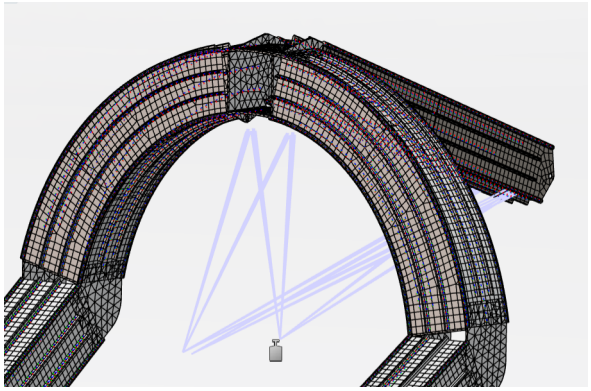

Figure 5.3: Couplings located at the engine, showing the links between engine loads and the engine mounting structure.

The landing gear is simplified and connected via three connections spot to the skin-stiffened landing gear box. These three connections represent two drag braces and the hydraulic cylinder in the extended landing gear case. Voeten [44] decided to place the two drag braces under an angle, instead as shown in Figure 4.4, to get a better distribution of the side loads by the landing gear. Voeten had the coupling at the end of these braces attached to the full back side, including aft panels, of the skin-stiffened box while it is unlikely that the landing gear will be connected at these positions. Therefore, it has been decided to limit the area of these connections to the part shown in Figure 5.4. The drag braces and hydraulic cylinder are connected to a central point which on itself is connected to the top part of the shock absorber, where the loads specified in Section 4 are applied. For the retracted landing gear the same three connection locations are applied but these are connected to the center of gravity of the retracted landing gear and the mass of the landing gear is added.

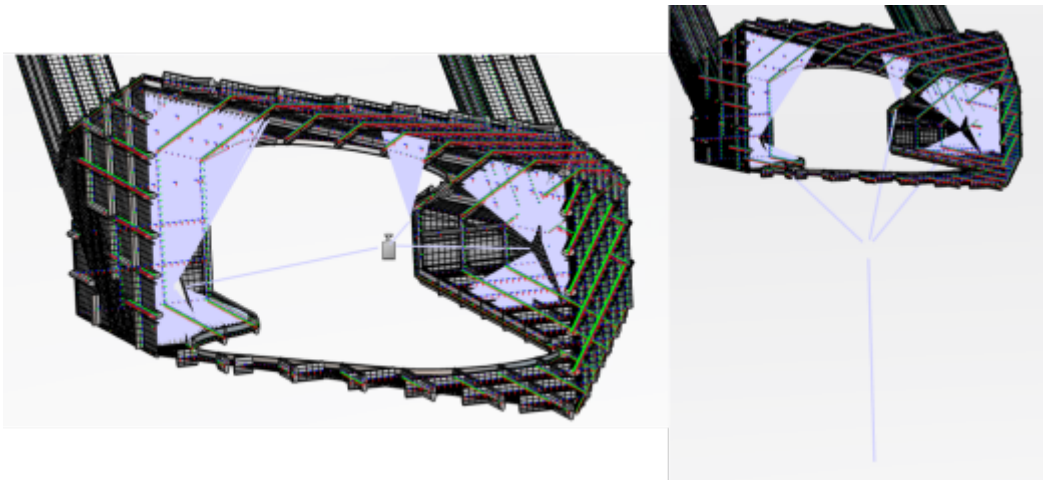

Figure 5.4: Couplings for the extended (right) and retracted (left) landing gear loadcases, showing the links between landing gear loads and engine mounting structure.

All couplings made from a single point to group are of the continuum distribution type with all degrees of freedom constrained. Furthermore all internal connections, connections between parts, panels etc., are done using a tie connection. Lastly, a clamped boundary condition is applied around the edges at the location of the spar, this can be seen in Figure 5.2.

5.4. Post-processing

In order to reach an optimized structure it is necessary to post-process the results in a way such that it can be determined if the critical value at a certain node has been exceeded. This is determined using a document-based approach, which is, as stated by Stefanovich [37], often used in industry for the engineering of an engine pylon. In this document-based approach a FE model is used to gather the

internal forces and von Mises stress at each node. Furthermore, the whole model is split into individual elements (stiffener, skin etc.) with their corresponding nodes. In this way, each element can be optimized individually regarding the individual failure modes. This process is repeated till all elements and thus the full structure reaches a satisfactory value.

In this section the analytical or empirical relations of the critical value for each individual failure modes are explained. In addition, it is explained for which element these failure modes are applicable and till which degree. Due to time limitations it has been decided to only use the same post-processing failure modes as Voeten [44].

5.4.1. Margin of Safety

The Margin of Safety (MoS) is the main parameter used to determine the safety of a structure. All the critical values and occurring values are used to calculate the MoS of that specific element. This is done such that different designs and failure modes can be compared using a normalised parameter and to easily determine the critical element of the structure. The MoS for each failure mode is calculated using Equation 5.4 and it is of high importance that for all elements $MoS \geq 0$.

$$MoS = \frac{Critical}{SF \cdot Occuring} - 1 \tag{5.4}$$

Herein is SF the safety factor that is applied for a structure. This safety factor is generally dependent on the part and loading conditions and is specified in the certification specifications of aviation agencies, in this case CS25 of EASA [13].

Two parts of the certification regarding safety factors are applicable for the engine mounting structure and are noted below. This means that for the to be analysed cases, a safety factor of 1.5 must be applied for all cases except the engine failure case (CR-05), which needs a safety factor of 1.0.

- **CS 25.303 Factor of safety**

  Unless otherwise specified, a factor of safety of 1.5 must be applied to the prescribed limit load which are considered external loads on the structure. When loading condition is prescribed in terms of ultimate loads, a factor of safety need not be applied unless otherwise specified.

- **CS 25.362 Engine failure loads**

  (a) For engine mounts, pylons and adjacent supporting airframe structure, an ultimate loading condition must be considered that combines 1g flight loads with the most critical transient dynamic loads and vibrations, as determined by dynamic analysis, resulting from failure of a blade, shaft, bearing or bearing support, or bird strike event. Any permanent deformation from these ultimate load conditions should not prevent continued safe flight and landing.

  (b) The ultimate loads developed from the conditions specified in paragraph (a) are to be:
  - multiplied by a factor of 1.0 when applied to engine mounts and pylons; and
  - multiplied by a factor of 1.25 when applied to adjacent supporting airframe structure.

5.4.2. Time-frame selection

The extraction and post-processing of all the data for each time-step in dynamic loadcases is a computational heavy job. In order to reduce this Voeten [44] decided to extract the von Mises stress for all time-steps and calculate the corresponding MoS. The time-step whereupon the minimum MoS occurs is assumed to have the highest nodal forces and thus to be the most critical time-step. Voeten could not verify the validity of this assumption as a mistake has been made while exporting the results. In other words, the extracted time-step of the nodal forces and minimum MoS are different from eachother. It has been decided to do the same assumption, however, if time allows, it will be checked for the final design if other time-steps results in higher nodal forces.

Assumption 10 *For each dynamic loadcase, the time step producing the lowest MoS in the Von Mises criterion provides the most critical nodal forces.*

5.4.3. Applied criteria

In this section the failure modes and other criteria are explained which are applied within this research.

Von Mises criterion

The yielding of structures happens when the stress at the material is high enough such that the deformation of the material goes from elastic to permanent plastic deformation. These deformations might influence the function of the structure and could therefore be deemed failed even before fracture. In order to prevent this the structure should be designed such that the stress does not exceed the yield strength. This yield strength is dependent on the chosen material and the treatment that it undergoes during manufacturing. The stress itself is often calculated using the Von Mises criterion, shown in Equation 5.5. [20]

$$\sigma_{Mises} = \sqrt{\frac{1}{2}((\sigma_{11} - \sigma_{22})^2 + (\sigma_{22} - \sigma_{33})^2 + (\sigma_{33} - \sigma_{11})^2) + 3(\sigma_{12}^2 + \sigma_{23}^2 + \sigma_{31}^2)} \tag{5.5}$$

If the value from the von Mises stress exceeds the yield strength then plastic deformation occurs. For the engine mounting structure this is considered a failure as it this might result in unpredictable and less optimal load paths. Therefore, it is desired that the maximum occurring von Mises stress is a safety factor below the yield strength as some loads might be underestimated or unforeseen. These von Mises stresses at each node are directly extracted from the 3DExperience software.

Displacement

In the regulations minor considerations regarding the displacement of the structure are made as shown below which is further specified in the AMC. In addition CS-25.362, noted in Section 4, specifies that any permanent deformation from these ultimate load conditions should not prevent continued safe flight and landing.

- **CS 25.305 Strength and deformation**

  (a) The structure must be able to support limit loads without detrimental permanent deformation. At any load up to limit loads, the deformation may not interfere with safe operation.

- **AMC 25.307 Proof of Structure**

  (a) be able to support limit loads without detrimental permanent deformation, and:
  (b) be able to support ultimate loads without failure.

Above means that for the ultimate limit case (CR-05) post-processing based on yielding is enough whereas for the limit cases it should be checked if the displacement interferes with safe operation. Therefore it should first be checked what this safe operations involves. For the engine mounting structure the only deformation which might affect the operation is the displacement and more specifically rotation of the engine as this changes the direction of the thrust and thus influences the performances of the aircraft. In addition, the total displacement should also be limited as the skin-stiffened landing gear box might affect the air intake of the engine and with that the performance when deformed too much.

As there are no specifications regarding these deflections and rotations, limits are set which are based on estimations when the air intake are disrupted. These limits are for simplicity set to be the same in all directions.

$$U_{limit} = 0.05\ m \qquad \theta_{limit} = 1^\circ$$

With the set limits in rotation and translation it is assumed that a follower force will have limited effect on the results.

Assumption 11 *Applying a follower force is not required as its effect is limited with the set limit on the displacement and rotation of the engine.*

Plate buckling
For the post-processing Voeten used panel equations and plane locations to split the panels into sub-panels and to know which node corresponds to which panel. With the addition of joints, thus nodes touching eachother, and panels changing orientations and size a new method was required to find the nodes corresponding to each element. This also meant that all the post-processing code needed to be rewritten using this, more general, method. This did require quite some time and due to time-limitations it has been chosen to only include the skin-stiffened landing box for the local panel buckling as it relatively easy compared to the overhead beams. The overhead beams have variable sized panels which are orientated differently compared to the global coordinate system and should be split using information from stiffeners, ribs and joints. For the splitting of the skin-stiffened box panels into sub-panels only the stiffeners are taken into account. This does mean that local panel buckling is also taken into account for the nodes which would normally be connected to the joints, making the analysis more conservative.

Recommendation 14 *A general method of splitting panels under a random orientation should be investigated in future research.*

Recommendation 15 *Local panel buckling for curved panels should be investigated in future research.*

For the local panel buckling similar conditions are used as Voeten [44] did. This means all sub-panels are considered to be loaded in all three directions, N_x, N_y and N_{xy}, and being simply supported at all four sides. Which still seem correct as all three loads are present and can thus occur simultaneously in a specific sub-panel. Furthermore, although the stiffeners in the corners are changed to angle stiffeners, instead of T-stiffeners, the sub-panels are still connected to a single flange. This single flange is not that stiff in the out of plane direction. In addition, it is assumed that every sub-panel is rectangular of shape. This is considered to be conservative as the size of a sub-panel in reality is always smaller than the one assumed. An example of the panel with all the unit loads is shown in Figure 5.5.

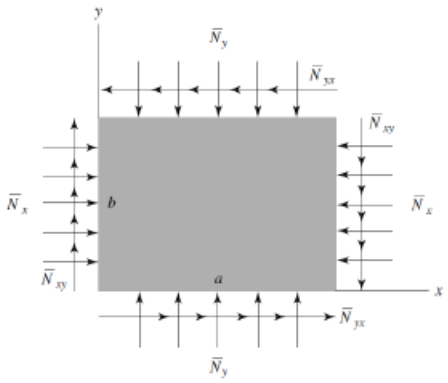

Figure 5.5: Example of plate with bi-axial and shear loading from Dim [12], illustrating the loads considered for local panel buckling.

Assumption 12 *Sub-panels can be assumed rectangular without underestimating the critical buckling loads.*

The critical buckling load can be found by solving the eigenvalue problem in Equation 5.6. The derivation is done by Voeten [44].

$$\mathbf{Aw} = N_x \mathbf{Bw} \tag{5.6}$$

Herein is $N_y = \alpha N_x$ and $N_{xy} = \beta N_x$ with A and B-matrix as shown below.

$$\mathbf{A} = \begin{bmatrix} \pi^4 D(\frac{a}{4b^3} + \frac{1}{2ab} + \frac{b}{4a^3}) & 0 & 0 & 0 \\ 0 & \pi^4 D(\frac{4a}{b^3} + \frac{2}{ab} + \frac{b}{4a^3}) & 0 & 0 \\ 0 & 0 & \pi^4 D(\frac{a}{4b^3} + \frac{2}{ab} + \frac{4b}{a^3}) & 0 \\ 0 & 0 & 0 & \pi^4 D(\frac{4a}{b^3} + \frac{8}{ab} + \frac{4b}{a^3}) \end{bmatrix}$$

$$\mathbf{B} = \begin{bmatrix} \frac{\pi^2}{4}(\frac{a\alpha}{b} + \frac{b}{a}) & 0 & 0 & -\frac{32\beta}{9} \\ 0 & \pi^2(\frac{a\alpha}{b} + \frac{b}{4a}) & \frac{32\beta}{9} & 0 \\ 0 & \frac{32\beta}{9} & \pi^2(\frac{a\alpha}{4b} + \frac{b}{a}) & 0 \\ -\frac{32\beta}{9} & 0 & 0 & \pi^2(\frac{a\alpha}{b} + \frac{b}{a}) \end{bmatrix}$$

Herein are a and b the length and width respectively as shown in Figure 5.5 and D is as shown in Equation 5.7.

$$D = \frac{Et^3}{12(1-\nu^2)} \tag{5.7}$$

The global buckling of the full panels including stiffeners is not included in the research due to time limits and local buckling is assumed to be more critical.

Assumption 13 *Local panel buckling is more critical than global panel buckling.*

Crippling
Crippling is a local failure happening in thin walled structures where a part of the structure fails while the rest is still able to carry the load. This happens for flanges or webs of thin-walled columns with an effective slenderness ratio smaller than 20. In this case the elements buckle as plates and the critical crippling stress ($\bar{\sigma_f}$) can be found using Equation 5.8. Herein is σ_{cy} the yield strength, t and b the thickness and width of the plate respectively, E is the Young modulus, α and n are empirical constants determined by experimental data and k depend on the kind of stiffener. [25]

$$\frac{\bar{\sigma_f}}{\sigma_{cy}} = \alpha k^{1-n}((\frac{t}{b})(\frac{E}{\sigma_{cy}})^{\frac{1}{2}})^{2(1-n)} \tag{5.8}$$

In the research it is assumed that the crippling is independent of the length, which can be valid if the aspect ratio of the plate reaches an asymptotic value. Almost all the stiffeners are relatively long compared to their width, which supports this assumption.

Assumption 14 *The crippling of a flange is independent of the length for all stiffeners.*

The values of $n = 0.6$ and $\alpha = 0.8$ for aluminium alloys are also used for titanium as no better value could be found [25]. Due to above assumption the asymptotic k values for the stiffeners can be found from the *Fundamentals of Aircraft Structural Analysis* by Curtis [8]. The flanges of the T-stiffener are clamped on one side and simply supported on the rest which results in a value of $k = 5.14$, whereas the web is free on one side and simply supported at the rest which gives $k = 0.425$. The angled corner stiffeners are also clamped on one side and simply supported at the rest resulting in $k = 5.14$

Due to the limited time of the research it has been chosen to exclude the crippling of the curved stiffeners from this research.

Column buckling
Column buckling is the sudden deformation of a column under a compressive load and the lowest critical buckling load is governed by Equation 5.9 for a straight, simply supported, homogeneous beam. Herein is P_{cr} the critical load whereupon buckling occurs, E the Young modulus, I the second moment of area and L the length of the beam. A simply supported boundary condition has been considered as it is the most conservative option.

$$P_{cr} = \frac{\pi^2 EI}{L^2} \tag{5.9}$$

The fact that the stiffeners are connected to a panel influences the critical buckling load. This is taken into account by taking the half of the width of the two connected sub-panels and calculate the additional second moment of area of this part of the panel. The total compressive force becomes the average nodal compressive force in the stiffener plus the average compressive force applied at the two half sub-panels. It should be noted, as mentioned before, that not all sub-panels are rectangular of shape and thus that the used values are not entirely correct with reality, but this effect is assumed to be limited.

Assumption 15 *The effect of non-rectangular sub-panels have limited effect on the critical buckling load.*

In the case of ultimate load conditions the sub-panels are allowed to post-buckle and the loads through the sub-panels are redistributed over the columns. The efficient width, which was first the two half sub-panels decreases when the post-buckling ratio increases. The relation between these two has been found by Kassapoglou [21] for quasi-isotropic materials and is shown in Equation 5.10.

$$b_{eff} = \frac{1}{2 + 1.3(1 - \frac{P_{cr}}{P_x})} \tag{5.10}$$

Lastly, crossing stiffeners in the skin-stiffened landing gear box and ribs in the overhead beams provide additional resistance against column buckling. This means that above given method is a more conservative approach and that improvements can still be made. On the contrary, the Euler-Johnson curve is not considered which means that for stiffeners with a small slenderness ratio the critical buckling stress is overestimated. Although this effect is assumed to be small it is still a point to be considered. Above mentioned points and the column buckling of curved stiffeners are not considered due to the limited research time.

Recommendation 16 *The effect of non-rectangular panels should be taken into account in future research.*

Recommendation 17 *The effect of crossing stiffeners on the column buckling of a specific stiffener should be included in future research.*

Recommendation 18 *The Euler-Johnson curve should be considered in future research.*

Recommendation 19 *The crippling and buckling of curved stiffeners should be included in future research.*

5.4.4. Additional considerations

In this section additional failure modes and considerations are explained which are of importance for the engine mounting structure but could not be applied at all or fully due to the limited time-frame of the research. The explanation of these failure modes and readiness for application are of various degrees but are only added to aid future research.

Fatigue

Fatigue, the process wherein a structure fails due to crack growth under cyclic loading, is a failure mode responsible for many unforeseen accidents because it happens at stresses below the yield strength of the material. It is also a failure mode extensively described in EASA CS 25.571 [13], and thus an important part of the evaluation of the design. The limited time of the research did not allow fatigue to be included in the post-processing. In order to implement fatigue still some work needs to be done.

Firstly, the design needs to be more detailed. Although the current design is more detailed than Voeten [44] it is still only concerning the primary elements. The regions of the structure which cause stress concentrations and are thus critical for fatigue are mostly located in the details which have not all been designed yet. These details are for example, radii in stiffener cross-section, type of connection and most importantly the connection the of landing gear. The landing gear gives the highest dynamic loads and fatigue evaluation will therefore highly be influenced by the connection.

Secondly, there is a need for a new standardised loading spectra. According to Nui [29], the use of ground to air to ground load cycles are functional as they produce the same fatigue damage to the structure as if the complete loading spectra was considered. Previous research regarding the Flying V, Dotman [11] and Nanninga [28], use a similar approach developed by De Jonge et al. [9]. In this approach is the fatigue loading standardized with respect to the mean stress during flight and ground operation on the wing itself. The engine mounting structure is a completely different structure, resulting in different mean stresses. This does not render the method useless but rather a new standardised loading spectra needs to be designed before this method can be applied. These are however hard to

design as each runway and flight is different, which means varying stress amplitudes. One can choose to design such that it will not fail for the maximum stress amplitude however this results in an unnecessary heavy and conservative structure. In order to take the varying stress amplitudes into account the linear cumulative damage hypothesis, also known as Miner rule, was developed. However, there are significant discrepancies in this rule, and these discrepancies need to be understood in order to get reasonable fatigue life considerations. Firstly, the Miner's rule ignores fatigue damage of cycles below the fatigue limit. These cycles can not cause crack initiation but can surely cause crack propagation. Furthermore, local effects such as crack tip plasticity and local strain hardening at crack tip are not taken into account, which would also vary with applied stress. Other theories have been developed but also these have not sufficient credibility from a physical point of view. If there are a lot of cycles below the fatigue limit, one could extend extend the slope S-N curve such that stress values below the fatigue limit can be used to reduce fatigue life [33].

Recommendation 20 *In future studies the effects of fatigue on the structure should be considered once the details are known.*

Creep
Creep is a time-dependent plasticity occurring when a material is under a fixed stress at elevated temperatures which could eventually lead to failure. This phenomena normally occurs at temperatures higher than 50% of the material's melting temperature (T_m) expressed in degrees Kelvin, and could be relevant for the parts directly connected to the engine. The temperature and stress might be high enough at these spots for longer periods of time, e.g. cruise, to have an effect. [23]

Despite high temperature creep ($T > 0.6T_m$) being the most apparent, this phenomena also occurs at intermediate ($0.6T_m > T > 0.3T_m$) or lower temperatures ($T < 0.3T_m$) for some materials [22]. The list of these materials include titanium alloys, which are mostly used for engine mounts whereof this design is no exception.

This failure mechanism has been considered qualitatively for the material but can be assessed numerically in future research.

Recommendation 21 *Future research should investigate the effect of creep on the overhead beams.*

Imperfections
Although not a failure mode, the introduction of imperfections are of importance as no structure is perfect. During manufacturing or assembly small initial imperfections could be added which result that the structure behaviour is less than ideal. Furthermore, small nodal moments, which are also ignored in this research, can behave as initial imperfections and lower the critical buckling load. It is recommended to add this to the calculation of the critical buckling loads in the future.

Recommendation 22 *Future studies should investigate the effect of initial imperfections on the structure.*

5.5. Proposed Optimization Method
In this section the initialisation of the variables and the proposed method of optimization is discussed.

5.5.1. Initialization
The initialization is based on the final dimensions of Voeten [44]. As the most influential changes have been made regarding the overhead structure it has been chosen to keep these beams slightly smaller as Voeten had. However, the dimensions of the skin-stiffened landing gear box has been copied exactly. It has been acknowledged that the stiffener dimensions are out of proportion. Above optimization does only alter these dimensions proportionally, which means that with current optimization method this problem will remain. Therefore it has been chosen to alter the dimensions of the stiffeners to more proportional values with approximately same cross-sectional area.

The index in the array for panel thicknesses refer to the numbers in Figure 5.6 below for each part,

for example [Panel 1, Panel 2, Panel 3, Panel 4]. The order for at the stiffeners are: [End-to-end height, flange width, web thickness, flange thickness].

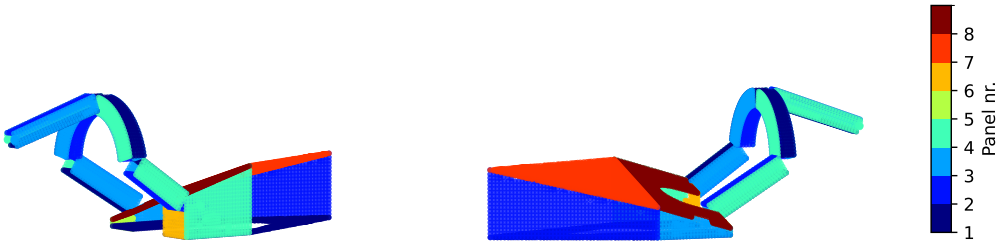

Figure 5.6: Engine mounting structure with colored panels, illustrating which array index of the panel thicknesses in Table 5.3 to 5.9 belongs to which panel.

Table 5.2: Mass and MoS of initial design.

Parameter	Value	Type
Mass [kg]	3483	Output
MoS [-]	-0.81	Output

Table 5.3: Initial dimensions for OH1.

Parameter	Value	Type	Parameter	Value [1]	Type
Width 1 [mm]	400	Input	Stiffeners 1 dim. [mm]	[100, 50, 10, 10]	Input
Height 1 [mm]	450	Input	Stiffeners 2 dim. [mm]	[100, 50, 10, 10]	Input
Width 2 [mm]	360	Input	Corner stiffener dim. [mm]	[75, 75, 10, 10]	Input
Height 2 [mm]	390	Input	Panel thicknesses [mm]	[5, 5, 5, 5]	Input
Nr of stiffeners 1 [-]	2	Input	Nr of ribs [-]	1	Input
Nr of stiffeners 2 [-]	2	Input	Rib thicknesses [mm]	2	Input

Table 5.4: Initial dimensions for OH2.

Parameter	Value	Type	Parameter	Value[1]	Type
Width 1 [mm]	500	Input	Stiffeners 1 dim. [mm]	[100, 50, 10, 10]	Input
Height 1 [mm]	520	Input	Stiffeners 2 dim. [mm]	[100, 50, 10, 10]	Input
Width 2 [mm]	440	Input	Corner stiffener dim. [mm]	[75, 75, 10, 10]	Input
Height 2 [mm]	460	Input	Panel thicknesses [mm]	[5, 5, 5, 5]	Input
Nr of stiffeners 1 [-]	2	Input	Nr of ribs [-]	1	Input
Nr of stiffeners 2 [-]	2	Input	Rib thicknesses [mm]	2	Input

Table 5.5: Initial dimensions for OH3.

Parameter	Value	Type	Parameter	Value[1]	Type
Width 1 [mm]	500	Input	Stiffeners 1 dim. [mm]	[100, 50, 10, 10]	Input
Height 1 [mm]	520	Input	Stiffeners 2 dim. [mm]	[100, 50, 10, 10]	Input
Width 2 [mm]	440	Input	Corner stiffener dim. [mm]	[75, 75, 10, 10]	Input
Height 2 [mm]	460	Input	Panel thicknesses [mm]	[5, 5, 5, 5]	Input
Nr of stiffeners 1 [-]	2	Input	Nr of ribs [-]	1	Input
Nr of stiffeners 2 [-]	2	Input	Rib thicknesses [mm]	2	Input

[1]The index in the array for panel thicknesses refers to the panel numbers shown in Figure 5.6. The dimensions for the stiffeners are listed as follows: [End-to-end height, flange width, web thickness, flange thickness]

Table 5.6: Initial dimensions for OH4.

Parameter	Value	Type	Parameter	Value[1]	Type
Width 1 [mm]	500	Input	Stiffeners 1 dim. [mm]	[100, 50, 10, 10]	Input
Height 1 [mm]	520	Input	Stiffeners 2 dim. [mm]	[100, 50, 10, 10]	Input
Width 2 [mm]	520	Input	Corner stiffener dim. [mm]	[75, 75, 10, 10]	Input
Height 2 [mm]	500	Input	Panel thicknesses [mm]	[5, 5, 5, 5]	Input
Nr of stiffeners 1 [-]	2	Input	Nr of ribs [-]	1	Input
Nr of stiffeners 2 [-]	2	Input	Rib thicknesses [mm]	2	Input

Table 5.7: Initial dimensions for OH5.

Parameter	Value	Type	Parameter	Value[1]	Type
Width 1 [mm]	500	Input	Stiffeners 1 dim. [mm]	[100, 50, 10, 10]	Input
Height 1 [mm]	520	Input	Stiffeners 2 dim. [mm]	[100, 50, 10, 10]	Input
Width 2 [mm]	520	Input	Corner stiffener dim. [mm]	[75, 75, 10, 10]	Input
Height 2 [mm]	500	Input	Panel thicknesses [mm]	[5, 5, 5, 5]	Input
Nr of stiffeners 1 [-]	2	Input	Nr of ribs [-]	1	Input
Nr of stiffeners 2 [-]	2	Input	Rib thicknesses [mm]	2	Input

Table 5.8: Initial dimensions for SSLB.

Parameter	Value[1]	Type
Panel thicknesses [mm]	[6.6, 6.5, 3.1, 1.5, 3.0, 2.2, 11.9, 7.8]	Input
Nr of stiffeners 1 [-]	13	Input
Nr of stiffeners 2 [-]	15	Input
Nr of stiffeners 3 [-]	5	Input
Stiffeners 1 dim. [mm]	[125, 90, 4, 4]	Input
Stiffeners 2 dim. [mm]	[80, 80, 7, 7]	Input
Stiffeners 3 dim. [mm]	[225, 90, 16, 16]	Input
Corner stiffener dim. [mm]	[250, 140, 9, 9]	Input

Table 5.9: Initial dimensions for joints.

Parameter	Value	Type	Parameter	Value	Type
Thickness OH12 [mm]	30	Input	Thickness SSLB4 [mm]	15	Input
Thickness OH24 [mm]	15	Input	Thickness SSLB5 [mm]	15	Input
Thickness OH35 [mm]	15	Input	Location SSLB5 along panel [mm]	400	Input

Proposed parameter update methodology

There are many ways to optimize a structure which have different level of complexity dependent on the application and the amount of data. Voeten [44] used the Design of Experiment (DoE) method. Within this method the limit values of each variable is found and many different designs within these limits are analysed. To ensure that the full range of possible designs are considered a latin hypercube sampling can be used, as shown by Voeten. The DoE method is able to find a reasonable design and spot the desired region of interest however not the most optimal design. Furthermore, it requires an initial analysis of the limits of each variable and one needs to analyse a lot of designs which are both time consuming. The amount of possible designs can increase exponentially with the addition of one extra design variable. Considering that the present design has over 100 additional variables compared to Voeten's design, it can be concluded that a good optimization using only the DoE method will be very time consuming. Based on this it has been decided to use a more progressive optimization method

[1]The index in the array for panel thicknesses refers to the panel numbers shown in Figure 5.6. The dimensions for the stiffeners are listed as follows: [End-to-end height, flange width, web thickness, flange thickness]

which uses the MoS output of the previous design to update the next design. The goal is not to get the perfect optimization method but rather a method that is faster than DoE, and can be extended in the future with additional variables without much loss in performance.

The relationship between MoS and variables for each failure mode are known and shown in Equations 5.12 to 5.17. The relationship of the failure mode which results in the smallest MoS will be used to alter the dimensions of the component according to that relationship and Equation 5.11 below. It should be noted that these failure modes can differ per component and thus every component is considered separately and altered simultaneously.

$$Factor = \frac{1}{MoS + 1} \tag{5.11}$$

The MoS of the von Mises stress is calculated using the data from 3DExperience. The stress is dependent on force and area whereof the former can not be changed. For panels and joints the thickness will increase whereas for stiffeners all dimensions will increase with a similar factor. It should be noted that possible stress concentrations can cause negative MoS due to the von Mises criterion but will not be removed using this method.

$$MoS + 1 \sim \frac{1}{\sigma_{Mises}} \sim A \tag{5.12}$$

The MoS of the displacement is also calculated using the data from 3DExperience. The displacement is mainly dependant on the width and height of the cross-section of the overhead beams. Whereof OH1 influences the relative displacement and OH4 and OH5 the total displacement, this means that dependant on which criteria a different part needs to be changed. The relationship between those criteria and the MoS is as shown in Equation 5.13.

$$MoS + 1 \sim \frac{1}{U_{limit}} \sim \frac{1}{\theta_{limit}} \sim I \sim bh^3 \sim b^3h \tag{5.13}$$

The MoS of panel buckling is dependant on three factors, the thickness, aspect ratio and either the width or length of the panel, dependant on direction. These relationships are non-linear and the aspect ratio and width or length of panel are affected by the same parameters, which makes it hard to twitch each of these variables accurately using a single relationship. Therefore, it has been decided to change both the thickness and the width and length of each subpanel separately for simplicity, thus ignoring the effect the alteration of one variable had on the MoS when changing the other afterwards. It is thought that the adaptive damping parameter, explained later this section, will prevent large unnecessary changes which might follow from this choice. The length and width of a subpanel is changed by adding additional stiffeners to the design.

$$MoS + 1 \sim t^3 \tag{5.14}$$

$$MoS + 1 \sim ab \tag{5.15}$$

The MoS of column buckling is dependant on the second moment of area I, which is dependent on the cross-section of the stiffener and panel thickness. This relationship is not linear but it is thought that for this base model it will suffice to consider linear relationship of each variable of the cross-section and to ignore the panel thickness. One could also change the number of stiffeners to lower the load per stiffener, but this option has been excluded as it is hard to work into a factor due to changing load paths. Furthermore, it is deemed less future proof as it is considered less mass efficient when optimizing on single stiffener level.

$$MoS + 1 \sim t_w \cdot b \cdot t_f \cdot d \tag{5.16}$$

The MoS of crippling is also dependant on the cross-section and does again not have a linear relationship. However, also for this failure mode a linear relationship is thought to be sufficient for basic optimization. A change in number of stiffeners is not considered for this failure mode for similar reasons as stated for column buckling.

$$MoS + 1 \sim t_w \cdot b \cdot t_f \cdot d \tag{5.17}$$

The initial dimensions can also surpass the minimum MoS of 0 easily or overshoot this value largely during the optimization. Therefore, it is of importance to set a range of acceptable MoS, which will

be $0 < MoS < 1$ for this research. This range is thought to save enough optimization time without losing too much performance in terms of mass. The MoS can also overshoot this desired range many times, so there might be a need to add an adaptive damping parameter (α). This adaptive damping parameter is increased each time it overshoots with a fixed value of 0.1 to a maximum of 0.8. The damping parameter is used to change the values of the variables as shown in Equation 5.18. The factor n is dependent on the degree of the relationship between parameter and MoS.

$$t_{new} = \alpha t_{old} + (1 - \alpha) \cdot t_{old} \cdot Factor^n \tag{5.18}$$

6

Crashworthiness

An aircraft is deemed crashworthy if it is able to protect the occupants in the event of a crash. The main strategy to avoid severe injuries is to use the aircraft structure to absorb the impact energy while keeping the deformation sufficient such that a survivable volume is kept and evacuation routes remain free. The novel, eccentric, shape of the cabin's typical cross section of the Flying-V makes the crashworthiness situation unique. A preliminary assessment regarding this topic has been done by Desiderio [10]. In his research, the effect of ovalization and floor-beam height is analysed using a typical cross section of a Fokker F-28 Fellowship aircraft, undergoing a vertical drop-test. It was found that more ovalization and lower floor-beam heights lead to strong increases in the accelerations perceived by the occupants, mainly due to the reduction in crushable volume and impact time duration. This information is used as leading parameters in the creation of various designs for the typical cross section of the Flying-V, which have been analysed in a similar manner as the Fokker F-28.

This chapter contains an follow-up of above described research wherein the engine mounting structure is connected to the most optimal design found by Desiderio. This is done to analyse the effect of the engine mounting structure on a crash-situation with retracted landing-gear. Simultaneously, the effect and possibility of engine separation is investigated. The results from this study are only used to draw conclusions and make some recommendations. In future studies the results may be used to optimize either or both structures.

Recommendation 23 *In future studies results from the crashworthiness tests may be implemented in the optimization model.*

6.1. Criteria for crashworthiness

In this section the criteria for a crash-worthiness aircraft are discussed. This is done by explaining the used crash injury criteria and requirements by Desiderio, which follow from the regulations [13] or The Transport Aircraft Crashworthiness and Ditching Working Group (TACDWG) [40].

6.1.1. Regulations regarding crashworthiness

An aircraft can be seen as crashworthy according to FAA AC20-107B 11.4 if it fulfills the following four, very general, requirements [43]:

1. *Occupants must be protected during the impact event from release of items of mass (e.g., overhead bins)*
2. *The emergency egress paths must remain following a survivable crash.*
3. *The acceleration and loads experienced by occupants during a survivable crash must not exceed critical thresholds.*
4. *A survivable volume of occupant space must be retained following the impact* event.

Desiderio's research goal was to get an initial assessment of the crashworthiness characteristics of the FV in terms of loads and accelerations sustained by the occupants. As this part of the research

is a follow-up research, with the goal to compare the new result to the result of Desiderio, it has been chosen to mainly focus on the 3rd requirement as well.

The regulations only state the maximum loads and accelerations that a person may handle in order to survive the crash with minimal injury. The problem is that in order to show compliance, a model of both seat and anthropomorphic dummy is required to obtain meaningful results. The TACDWG, a group consistent of both experts from the industry (Boeing, Airbus, etc.), and research institutes (NASA, the German Aerospace Center - DLR, among others) recognizes this issue and suggests that other crash injury criteria could be used to show means of compliance. One of these criteria, also used by Desiderio, is the Dynamic Response Index (DRI) and will be further explained in Section 6.1.2. Again, as this is a follow-up research, only the DRI criteria will be considered as it is the sole criteria used by Desiderio.

In addition, the aircraft-level dynamic crash conditions are not specified. The TACDWG acknowledges this gap in regulations as well. Based on self-assessments of original equipment manufacturers and accident studies the TACDWG proposed requirement for the vertical impact velocity is a function of the aircraft's maximum take-off weight (MTOW) shown in Figure 6.1. Desiderio uses this function and the MTOW found by Oosterom [31] to find the vertical impact velocity for the most critical case, the FV-1000, which results in the first requirement set by Desiderio [10]:

FV1000-CRASH-001: The crash-worthiness properties of the typical section of Flying-V aircraft shall be evaluated by means of a drop test at a minimum vertical impact velocity of 26 ft/s, with the fuselage center line horizontal.

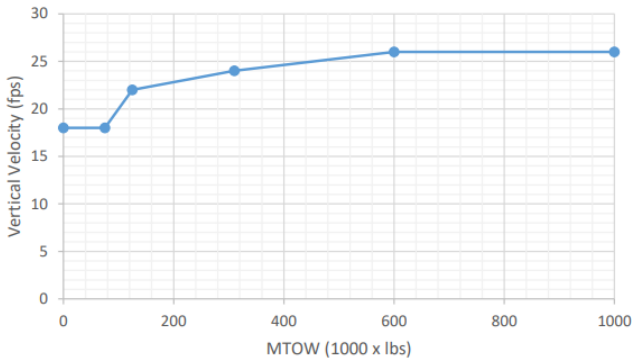

Figure 6.1: Function of vertical velocity impact with MTOW, showing a minimum of 26 ft/s vertical impact velocity for the Flying-V, taken from TACDWG. [40]

6.1.2. Dynamic Response Index

The DRI is a crash injury criteria initially designed to determine the probability of spinal injuries in pilots subjected to the high-amplitude and short-duration accelerations induced by ejection seats [5]. As DRI, only requires the acceleration at airframe level, it is relatively easy to calculate in the case of a drop test. In DRI the total mass acting on the vertebrae is estimated as a point mass in a single degree of freedom spring-dashpot model with Equation 6.1.

$$\frac{d^2\delta}{dt^2} + 2\zeta\omega_n\frac{d\delta}{dt} + \omega_n^2 \cdot \delta = a \tag{6.1}$$

Herein is δ the degree of freedom, ζ the damping ratio and ω_n the natural frequency and a the vertical acceleration. The corresponding DRI value can be calculated using Equation 6.2, wherein g is the gravitational constant [5] .

$$DRI = \frac{\omega_n^2\delta_{max}}{g} \tag{6.2}$$

Stech and Payne [36], considering the 50th percentile of United States Air Force pilots of the time, found ω_n = 52.9 rad/s and ζ = 0.224.

Desiderio [10] does a good job in explaining the downsides of this method, and mainly the used values ζ and ω_n. However, these downside do not have an influence at the indication of the severity of an acceleration effect and therefore DRI can still be a good indicator. For this reason, even with the current values for ω_n and ζ, regulators have accepted an DRI lower than 16 as a means of compliance for crash-worthiness [40]. From this the second and last requirement from Desiderio [10] is set:

FV1000-CRASH-002: The Flying-V typical section shall be designed such that, following the dynamic conditions specified in FV1000-CRASH-001, an equivalent DRI not greater than 16 units is achieved.

It should be noted that Desiderio specified an equivalent DRI, which is an weighted average of all the DRIs. In this research the normal DRIs are considered, as it is thought to be illogical to combine all DRIs into a single value for two reasons. Firstly, it is of interest that all passengers survive, for example it is not desired that half of the passengers have a DRI of 5 and the other half has an DRI of 20. Secondly, it does not show the distribution of the DRIs along the fuselage, losing critical information about the influence of specific designs.

The addition of the engine mounting structure causes a rotation of the fuselage, this will result in accelerations other than the single degree freedom specified in the DRI. In order to take this into account, the United States Airforce, has developed the relationship in Equation 6.3 for ejection seats. [41]

$$\sqrt{(\frac{DRI}{DRI_L})^2 + (\frac{G_x}{G_{xL}})^2 + (\frac{G_y}{G_{yL}})^2} \leq 1 \tag{6.3}$$

Herein is DRI_L the limit DRI, thus 16, G_x and G_y are the acceleration magnitudes to the for and aft and sideways respectively with G_{xL} and G_{yL} as limit values of these magnitudes. In the cases where the acceleration component in z-direction is going downwards, than the $\frac{DRI}{DRI_L}$ term shall be replaced with $\frac{-G_z}{-G_{zL}}$.

The unknown limit values (G_{xL}, G_{yL} and G_{zL}) are dependent on the rise time t_R and plateau duration Δt of the acceleration time plot and are calculated based on percentages of peak acceleration. An example is shown in Figure 6.2. The tables in Figure A.1 to A.6 can then be interpolated to get the limit values.

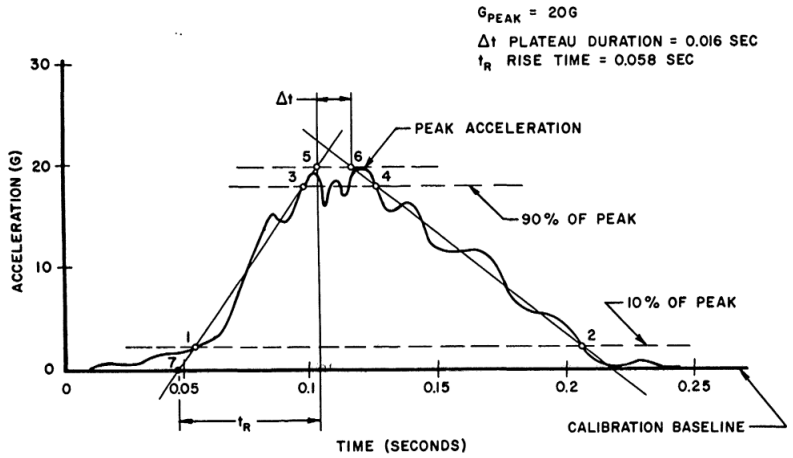

Figure 6.2: An example of an acceleration time with the method used to determine the rise time and plateau time. [41]

Again it should be noted that above method is normally used for fighter pilots, which means that for a normal passenger the limit accelerations are likely lower. Nonetheless, the criteria in Equation 6.3 can still be used to compare the severity of different cases. Therefore from now on Equation 6.4 below will be used, wherein SEV is the severity factor. It should be noted that the equation below is conservative as the maximum DRI, G_x and G_y are considered which do not necessarily happen at the same time.

$$\sqrt{(\frac{DRI}{DRI_L})^2 + (\frac{G_x}{G_{xL}})^2 + (\frac{G_y}{G_{yL}})^2} = SEV \tag{6.4}$$

6.2. Model

In this section an overview of the model in 3DExperience is given. To simplify the model it is necessary to estimate the inertial properties of various parts of the aircraft, which is also assessed in this section.

6.2.1. Estimation of inertial properties

As mentioned, with the addition of the engine mounting structure to the structure the center of mass of the model is not closely aligned with the center of the fuselage anymore. This means that at the moment of impact an unrealistic rotation will happen, as the inertial properties of the rest of the aircraft are not taken into account. Modelling the rest of the aircraft is unrealistic as parts of the aircraft are not designed yet and this will lead to an unnecessary computational heavy model. The approach that will be used is to couple the inertial properties of these parts to the existing model. This coupling will consist of two parts, one at each side of the fuselage.

As mentioned before, large parts of the aircraft still have to be designed. This means that the found inertial properties are a very rough estimation of the inertial properties of the final design. Therefore some assumptions have been made which have relatively small effect on the properties compared to simplification of the calculations. The first assumption made is to assume that all non-designed sections of the aircraft are made from a single material, namely Al2024-T361. This is based on the material used by Desiderio [10] for the general section of the wing-fuselage. An additional assumption is made to separate the aircraft in five distinct sections as shown with different colors in Figure 6.3. This leads to the following assumptions and recommendation:

Assumption 16 *All non-designed sections are made of Al2024-T361.*

Assumption 17 *The aircraft can be divided into five separate sections for a decent indication of the total inertial properties.*

Recommendation 24 *In future research, the inertial properties of the full aircraft needs to be determined more accurately.*

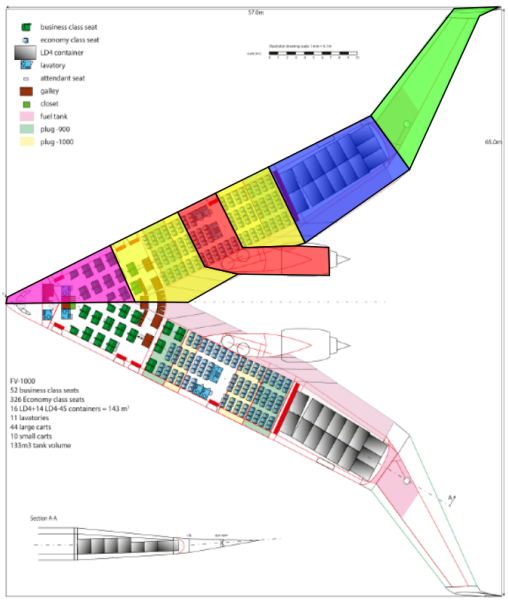

Figure 6.3: Different aircraft sections of FV-1000 wherefrom the inertia is calculated, adapted from Oosterom. [31]

The moments of inertia in this part, unless mentioned otherwise, are from the center of gravity, which itself is calculated from the global coordinate system. This global coordinate system has its origin in the nose of the aircraft, with x-axis in the length of the aircraft, y-axis in the span-direction of the aircraft, and z-axis in the height direction. The initial inertia properties for all sections apart from the red section has been taken in the local coordinate frame and need to be rotated to the global coordinate system using Equation 6.5.

$$I_{Global} = R \cdot I_{Local} \cdot R^T \tag{6.5}$$

Herein is R the rotation matrix, defined as shown in Equation 6.6.

$$R = \begin{bmatrix} cos(\theta) & -sin(\theta) & 0 \\ sin(\theta) & cos(\theta) & 0 \\ 0 & 0 & 1 \end{bmatrix} \tag{6.6}$$

Red section
The red section defined in Figure 6.3 is the model used for the drop-test. Due to symmetric loading during the test only one side of the aircraft is required which means that no inertial properties need to be calculated for this part. However, it has been decided to include it for completeness. The inertial properties can directly be extracted from the 3DExperience software. The found inertia is as follows:

$$I_R = \begin{bmatrix} 166208 & 153737 & -55675.7 \\ 153737 & 386224 & 16529.8 \\ -55675.7 & 16529.8 & 511803 \end{bmatrix} kgm^2 \qquad m_R = 29229.7\ kg$$

The inertia of the red section has been extracted later in the research and has been taken from a model already orientated with respect to the global coordinate frame.

Yellow section
The yellow sections are equivalent to Desiderio's model, the inertial properties of these parts can almost directly be extracted from the 3DExperience software. The only thing that needs to be altered is the length. As the yellow section extends to both sides it is divided into two parts, Y1, towards the front and Y2 towards the back of the aircraft. The estimated lengths, from Figure 6.3, is 7.3 m for Y1 and 5.9 m for Y2. The extracted inertia matrices from the center of gravity are shown below.

$$I_{Y1} = \begin{bmatrix} 50949.4 & -11.7733 & 1.53982 \\ -11.7733 & 50486.9 & 5.33309 \\ 1.53982 & 5.33309 & 91801.9 \end{bmatrix} kgm^2 \quad I_{Y2} = \begin{bmatrix} 38457.6 & 43.1495 & -5.40272 \\ 43.1495 & 23005.3 & 0.1704 \\ -5.40272 & 0.1704 & 54130.7 \end{bmatrix} kgm^2$$

These values are in their local system and need to be rotated using Equation 6.5. Depending on the side of the aircraft this is either clockwise or counterclockwise with the trailing edge sweep angle of 25.5° from Oosterom [31]. Resulting in the final inertia properties for the right (R) side of the aircraft:

$$I_{RY1} = \begin{bmatrix} 50854.53 & -187.12 & 3.69 \\ -187.12 & 50581.77 & 4.15 \\ 3.69 & 4.15 & 91801.9 \end{bmatrix} kgm^2 \quad I_{RY2} = \begin{bmatrix} 35627.21 & -5977.19 & -4.80 \\ -5977.19 & 25835.69 & 2.48 \\ -4.80 & 2.48 & 54130.7 \end{bmatrix} kgm^2$$

$$m_{Y1} = 7987.75\ kg \qquad m_{Y2} = 10610.6\ kg$$

The location of the center of gravity of each of the sections are as follows:

$$X_{Y1} = 18.610\ m \qquad Y_{Y1} = 5.298\ m \qquad Z_{Y1} = -0.371\ m$$
$$X_{Y2} = 29.931\ m \qquad Y_{Y2} = 10.611\ m \qquad Z_{Y2} = -0.360\ m$$

Blue section
The blue section is almost equivalent to Desiderio's model, however the mass of the passengers is replaced with cargo, which results in a slightly more dense section. The length of the blue section

is estimated at 12.4 m from Figure 6.3. Extending Desiderio's model to this length and removing the passenger inertias results in the following inertia properties for the structure of the cargo section:

$$I = \begin{bmatrix} 31669.8 & 116.271 & -2.57597 \\ 116.271 & 64144.9 & 2.64046 \\ -2.57597 & 2.64046 & 79773.6 \end{bmatrix} kgm^2 \qquad m = 4336.26\,kg$$

However, as mentioned, this structure is filled with cargo. Which is assumed to be a cuboid shape with dimensions of 12 x 5.8 x 1.22 m and a constant density of 161 kgm^{-3} [11] [18]. This results that the cargo has the following inertial properties:

$$I = \begin{bmatrix} 0.40020 & 0 & 0 \\ 0 & 2.0237 & 0 \\ 0 & 0 & 1.6575 \end{bmatrix} \cdot 10^5\ kgm^2 \qquad m = 13670.832\,kg$$

Assumption 18 *The blue section contains cargo in a cuboid shape with dimensions of 12.4 x 6 x 2 m and a constant density of 161* kgm^{-3}*.*

As the location of the center of gravity of cargo and structure is at the same location the inertia can be summed up which results in the final inertial properties of the blue section:

$$I_B = \begin{bmatrix} 71689.8 & 116.271 & -2.57597 \\ 116.271 & 266519.0 & 2.64046 \\ -2.57597 & 2.64046 & 245523.6 \end{bmatrix} kgm^2 \qquad m_B = 18007.092\,kg$$

These values are in their local system and need to be rotated using Equation 6.5. Depending on the side of the aircraft this is either clockwise or counterclockwise with the trailing edge sweep angle of 25.5°. Resulting in the final inertia properties for the right (R) side of the aircraft:

$$I_{RB} = \begin{bmatrix} 107889.765 & 75778.535 & -1.188 \\ 75778.535 & 230319.035 & 3.492 \\ -1.188 & 3.492 & 245523.6 \end{bmatrix} kgm^2 \qquad m_B = 18007.092\,kg$$

$$X_B = 38.221\ m \qquad Y_B = 14.471\ m \qquad Z_B = -0.367\ m$$

Green section

The green section is the outer wing, the most detailed design available is from Nanninga [28]. From this research the resultant mass estimate can be found, there is however no information about the moment of inertia or location of the center of gravity. These values needs to be estimated, which is done using the simplified mass and inertia estimate of Moulton and Hunsaker [27]. To use these estimates the research specifies that a 4 digit NACA airfoil is assumed while neglecting twist, camber and dihedral effects. The resultant moments of inertia at the root of the wing can be calculated using Equations 6.7 to 6.11.

$$I_{xx_0} = m \cdot \left(\frac{56b^2\kappa_f\nu_0 + \kappa_g\nu_3}{280\kappa_a\nu_0}\right) \tag{6.7}$$

$$I_{yy_0} = m \cdot \left(\frac{84b \cdot (2b\kappa_f\nu_0 \tan^2(\Lambda) + \kappa_d\nu_1 \tan(\Lambda)) + 49\kappa_e\nu_2 + 3\kappa_g\nu_3}{840\kappa_a\nu_0}\right) \tag{6.8}$$

$$I_{zz_0} = m \cdot \left(\frac{12b \cdot (2b\kappa_f\nu_0(\tan^2(\Lambda) + 1) + \kappa_d\nu_1 \tan(\Lambda)) + 7\kappa_e\nu_2}{120\kappa_a\nu_0}\right) \tag{6.9}$$

$$I_{xy0} = I_{yx_0} = -\delta \cdot b \cdot m \cdot \left(\frac{4b\kappa_f\nu_0 \tan(\Lambda) + \kappa_d\nu_1}{20\kappa_a\nu_0}\right) \tag{6.10}$$

$$I_{xz0} = I_{zx0} = I_{yz0} = I_{zy0} = 0 \tag{6.11}$$

Herein is m the mass, Λ the quarter-chord sweep angle, κ the wing planform coefficient, ν the thickness distribution coefficient and δ the left wing/ right wing sign coefficient.

The thickness distribution coefficients can be calculated using Equations 6.12 to 6.15.

$$\nu_0 = \frac{1}{60}(40a_0 + 30a_1 + 20a_2 + 15a_3 + 12a_4) \tag{6.12}$$

$$\nu_1 = \frac{1}{60}(56a_0 + 50a_1 + 40a_2 + 33a_3 + 28a_4) \tag{6.13}$$

$$\nu_2 = \frac{1}{980}(856a_0 + 770a_1 + 644a_2 + 553a_3 + 484a_4) \tag{6.14}$$

$$\begin{aligned}\nu_3 = {} & \frac{2}{5}a_0^3 + a_0^2a_1 + \frac{3}{4}a_0^2a_2 + \frac{3}{5}a_0^2a_3 + \frac{1}{2}a_0^2a_4 + \frac{6}{7}a_0a_1^2 + \frac{4}{3}a_0a_1a_2 + \frac{12}{11}a_0a_1a_3 + \frac{12}{13}a_0a_1a_4 \\ & + \frac{6}{11}a_0a_2^2 + \frac{12}{13}a_0a_2a_3 + \frac{4}{5}a_0a_2a_4 + \frac{2}{5}a_0a_3^2 + \frac{12}{17}a_0a_3a_4 + \frac{6}{19}a_0a_4^2 + \frac{1}{4}a_1^3 + \frac{3}{5}a_1^2a_2 \\ & + \frac{1}{2}a_1^2a_3 + \frac{3}{7}a_1^2a_4 + \frac{1}{2}a_1a_2^2 + \frac{6}{7}a_1a_2a_3 + \frac{3}{4}a_1a_2a_3 + \frac{3}{8}a_1a_3^2 + \frac{2}{3}a_1a_3a_4 + \frac{3}{10}a_1a_4^2 \\ & + \frac{1}{7}a_2^3 + \frac{3}{8}a_2^2a_3 + \frac{1}{3}a_2^2a_4 + \frac{1}{3}a_2a_3^2 + \frac{3}{5}a_2a_3a_4 + \frac{3}{11}a_2a_4^2 + \frac{1}{10}a_3^3 + \frac{3}{11}a_3^2a_4 + \frac{1}{4}a_3a_4^2 \\ & + \frac{1}{4}a_3a_4^2 + \frac{1}{13}a_4^3\end{aligned} \tag{6.15}$$

From Oosterom [31] it can be found that the outer wing is an symmetrical NACA 0012 airfoil. This means that the following coefficients, from [27], can be used for the calculation:

$$a_0 = 2.969 \qquad a_1 = -1.260 \qquad a_2 = -3.516 \qquad a_3 = 2.843 \qquad a_4 = -1.015$$

Which result in the following thickness distribution coefficients:

$$\nu_0 = 0.6851 \qquad \nu_1 = 0.4670 \qquad \nu_2 = 0.3958 \qquad \nu_3 = -8.5990$$

The wing planform coefficients can be calculated using Equations 6.16 to 6.20.

$$\kappa_a \equiv \tau_r(3c_r^2 + 2c_rc_t + c_t^2) + \tau_t(c_r^2 + 2c_rc_t + 3c_t^2) \tag{6.16}$$

$$\kappa_d \equiv \tau_r(c_r + c_t)(2c_r^2 + c_rc_t + 2c_t^2) + \tau_t(c_r^3 + 3c_r^2c_t + 6c_rc_t^2 + 10c_t^3) \tag{6.17}$$

$$\kappa_e \equiv \tau_r(5c_r^4 + 4c_r^3c_t + 3c_r^2c_t^2 + 2c_rc_t^3 + c_t^4) + \tau_t(c_r^4 + 2c_r^3c_t + 3c_r^2c_t^2 + 4c_rc_t^3 + 5c_t^4) \tag{6.18}$$

$$\kappa_f \equiv \tau_r(c_r^2 + 2c_rc_t + 2c_t^2) + \tau_t(c_r^2 + 4c_rc_t + 10c_t^2) \tag{6.19}$$

$$\begin{aligned}\kappa_g \equiv {} & \tau_r^3(35c_r^4 + 20c_r^3c_t + 10c_r^2c_t^2 + 4c_rc_t^3 + c_t^4) + \tau_r^2\tau_t(15c_r^4 + 20c_r^3c_t + 18c_r^2c_t^2 + 12c_rc_t^3 + 5c_t^4) \\ & + \tau_r\tau_t^2(5c_r^4 + 12c_r^3c_t + 18c_r^2c_t^2 + 20c_rc_t^3 + 15c_t^4) + \tau_t^3(c_r^4 + 4c_r^3c_t + 10c_r^2c_t^2 + 20c_rc_t^3 + 35c^4)\end{aligned} \tag{6.20}$$

Herein is c_r the chord length at the root, c_t the cord length at the tip and τ_r and τ_t are the percent airfoil thickness at tip and root respectively.

The values of c_r and c_t and also Λ are extracted from Dotman [11]. Which estimated these from a CAD model of the outer mold of the Flying-V. The estimated values are shown below.

$$c_r = 6.0\ m \qquad c_t = 3.2\ m \qquad \Lambda = 26°$$

The airfoil thickness of the outer wing could not be found in previous research, therefore it is estimated using a CAD model of the outer shape in 3DExperience. The real owner of the CAD model is unknown as there are many copies of it and there are multiple folders, wherefrom only one can be accessed. The oldest version available within the folder is from D. M. Atherstone. The estimated thickness at the root is $t_r \cdot c_r = 3.5\ m$ and $t_t \cdot c_t = 0.3\ m$, which results in the following percent airfoil thicknesses:

$$t_r = 0.5833 \qquad t_c = 0.0937$$

This results in the following wing planform coefficients:

$$\kappa_a = 101.22\ m^2 \qquad \kappa_d = 717.18\ m^3 \qquad \kappa_e = 6805.51\ m^4 \qquad \kappa_f = 75.51\ m^2 \qquad \kappa_g = 14168.64.\ m^4$$

Substituting all found values, together with semispan length of $b = 15.33\ m$ from Oosterom [31] and mass of $3500\ kg$ from Nanninga [28], results in the following inertia matrix;

$$I_G = \begin{bmatrix} 1.0076 & \delta \cdot -0.72814 & 0 \\ \delta \cdot -0.72814 & 0.27802 & 0 \\ 0 & 0 & 1.7249 \end{bmatrix} \cdot 10^5\ kgm^2$$

Herein is δ, 1 or -1, dependent on the right or left wing.

The resultant inertia values are from the root with the local axis system as defined in Figure 6.4. This means that the inertia values need to be rotated to the global frame. This is done using the same rotation matrix and method as specified before but with a different angle.

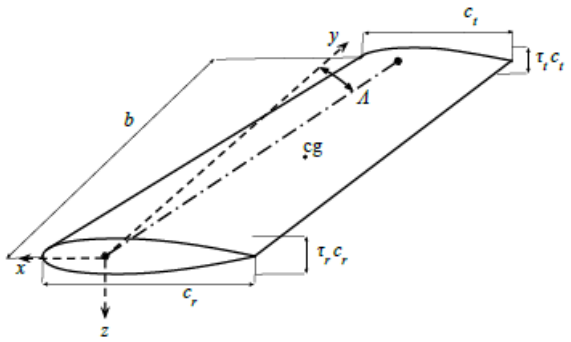

Figure 6.4: Image of an aircraft wing, showing the local axis and the used thicknesses, from Moulton and Hunsaker. [27]

The angle of 37.4° between the outer wing and the global x-axis is extracted from Oosterom [31]. Which results in the following global inertia matrix at the root of the outer wing, with corresponding mass and approximate location. The location is approximated using Figure 6.3.

$$I_{RG} = \begin{bmatrix} 0.0358 & -0.5429 & 0 \\ -0.5429 & 1.2498 & 0 \\ 0 & 0 & 1.7249 \end{bmatrix} \cdot 10^5\ kgm^2 \qquad m_G = 3500\ kg$$

$$X_G = 42\ m \qquad Y_G = 17.5\ m \qquad Z_G = 0\ m \tag{6.21}$$

Purple section

The purple section is the hardest part to estimate the inertial properties as no designs are available. Furthermore, this is also one of the more important parts as this part houses a lot of heavy systems such as the nose landing gear, and consists of the, likely, heavy structural joint of the two wing-fuselages. An rough estimate of the mass can be done but for the inertia it is of high importance how this mass is arranged. In order to have a somewhat decent estimate, it has been chosen to extend Desiderio's model to the desired length and split it in half, as shown in Figure 6.5. In the figure can be seen that structural elements are split in half and mirroring the element along the split plane will result in a unsound structure. This means that the found inertia values are unrealistic, but in the current state of affairs no better method could be thought of. This specifies again the high importance to reconsider the inertia values of this and other sections in future research. The main landing gear is the sole thing also taken into account apart from the structure, which is approximated at 8.9 m from the nose at -1.05 m in height direction with half its mass of 640 kg [31] [4].

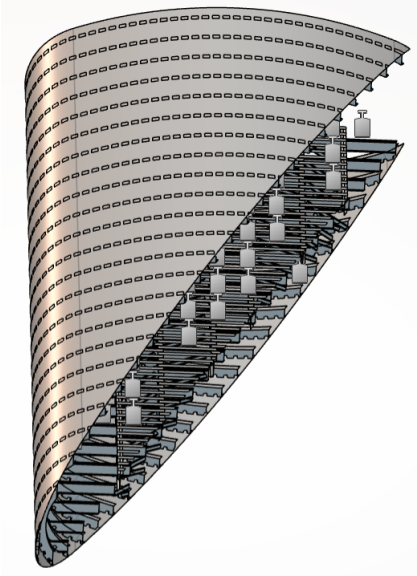

Figure 6.5: Visualisation of the model used to estimate the inertia of the purple section.

Recommendation 25 *The inertia of all sections, especially the purple section, needs to be recalculated in the future.*

The inertia values are extracted directly from the 3DExperience software and are shown below.

$$I = \begin{bmatrix} 31875.8 & -23153.9 & 1634.32 \\ -23153.9 & 101457 & 620.827 \\ 1634.32 & 620.827 & 124258 \end{bmatrix} \; kgm^2$$

These values are in their local system and need to be rotated using Equation 6.5. Depending on the side of the aircraft this is either clockwise or counterclockwise with the trailing edge sweep angle of 25.5°. Resulting in the final inertia properties for the right (R) side of the aircraft:

$$I_{RP} = \begin{bmatrix} 0.2678 & 0.1247 & 0.0174 \\ 0.1247 & 1.0655 & -0.0014 \\ 0.0174 & -0.0014 & 1.2426 \end{bmatrix} \cdot 10^5 \; kgm^2 \qquad m_P = 9995.783 \; kg$$

$$X_P = 10.530 \; m \qquad Y_P = 2.821 \; m \qquad Z_P = -0.395 \; m$$

Super-position
Now all the sections are simplified to a single point with their total inertial properties they need to be connected to the model. In order to simplify the model even further these points are translated to two points using the principle of super-position and the parallel axis theorem. These two points are located at either side of the model, where the purple section and Y1 are connected to one side and Y2 and the green and blue section to the other side. The position of the two points are;

$$X_1 = 21.452 \; m \qquad Y_1 = 6.613 \; m \qquad Z_1 = -0.373 \; m$$
$$X_2 = 27.920 \; m \qquad Y_2 = 9.628 \; m \qquad Z_2 = -0.373 \; m$$

The inertial properties at each point can be calculated using Equation 6.22, with $\mathbf{R} = R_1\hat{\mathbf{x}} + R_2\hat{\mathbf{y}} + R_3\hat{\mathbf{z}}$.

$$J_{ij} = \sum (I_{ij} + m(|\mathbf{R}|^2\delta_{ij} - R_iR_j)) \tag{6.22}$$

Using the values in this document results in the following inertial properties:

$$I_1 = \begin{bmatrix} 0.2352 & -0.4316 & -0.0006 \\ -0.4316 & 1.4141 & -0.0010 \\ -0.0006 & -0.0010 & 1.6305 \end{bmatrix} \cdot 10^6 \; kgm^2 \quad I_2 = \begin{bmatrix} 0.7971 & -1.2917 & -0.0198 \\ -1.2917 & 3.0291 & -0.0109 \\ -0.0198 & -0.0109 & 3.7692 \end{bmatrix} \cdot 10^6 \; kgm^2$$

Only the inertia is added to the model, thus not the mass, as this would lead to higher acceleration without taking the crash and thus energy absorption of the other parts into account. Figure 6.6 has been added for clarification.

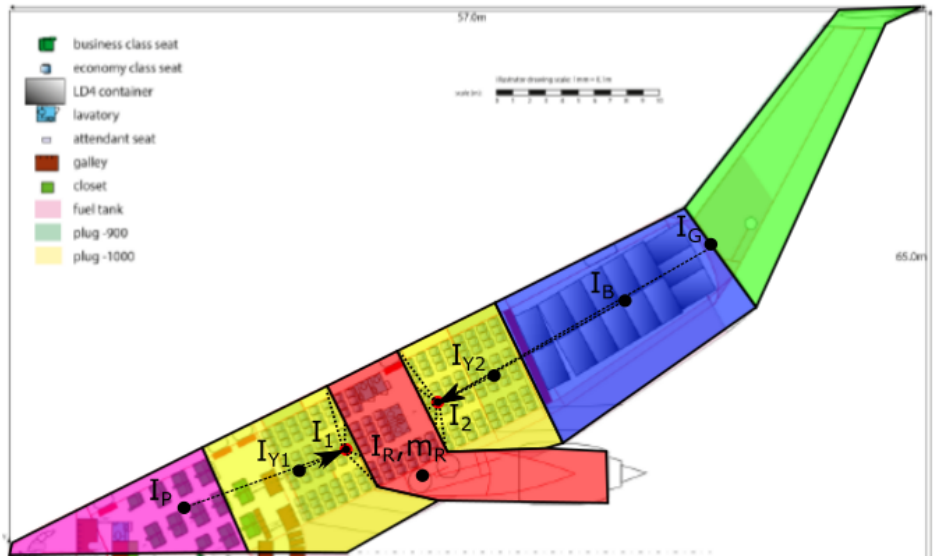

Figure 6.6: Overview of the applied parallel axis theorem, adapted from Oosterom. [31]

6.2.2. FEA model

The final model for the drop test is shown in Figure 6.7. Some important decisions made by Desiderio, which also affect this model are itemized below.

- Stiffeners are excluded from the analysis for the wing-fuselage part as Desiderio has determined that these do not significantly affect the crash characteristics.
- The comparison section is a five-frame one as Desiderio determined there is little to no difference between a five and six-frames section, which is generally used for certification purposes.
- All joints are made using tie connections.
- General contact interaction properties to avoid element penetration are hard contact for normal behavior and tangential behavior uses a penalty friction formulation with a friction coefficient of k_f = 0.5.
- The mass of a single passenger is assumed to be 90 kg with a seat of 10 kg, making the total for a single point mass 100 kg.
- Above point masses are connected using a flexible coupling with the floor structure. These couplings have a stiffness which is assumed to be 3924 N/mm.
- The vertical distance between the point mass and the floor beams has been set to approximately coincide with the location of the lumbar region of a seated passenger.

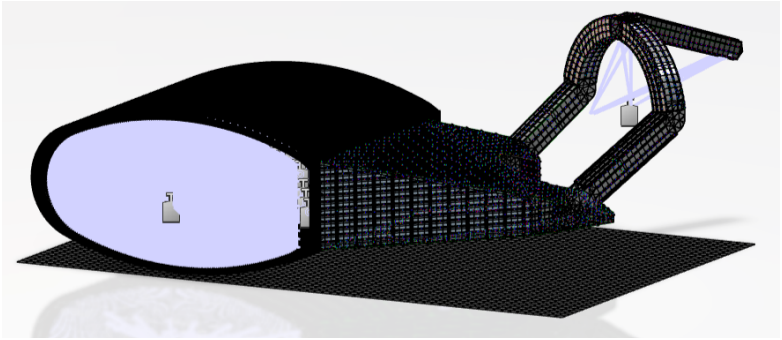

Figure 6.7: A depiction of the used drop test model.

It should be noted that the calculated inertia in previous section are also connected using a flexible coupling to the skin, spar and longitudinal floor beams with infinite stiffness.

The simulation settings are similar as Desiderio, this means an explicit dynamic analysis and that every node of the model, except from the ground, gets an initial velocity of -7.9248 ms^{-1} as according to requirement FV1000-CRASH-001. Furthermore, the ground itself is fixed using a clamped boundary condition and a gravitational load of 9.81 ms^{-2} is applied to the whole model. Desiderio found that increasing the number of frames has little effect on the crashing behaviour for normal fuselages and he only analysed it for a limited number of frames and only considered energy absorption. Therefore first an analysis will be performed on the extended version of the Flying-V to ensure that only the influence of the engine mounting structure is taken into account.

As mentioned before, Al2024-T361 is used as the material for the fuselage. The used properties of this material are noted in Table 6.1 below. It has been noticed that in Desiderio's model a different A and B values in the Johnson-Cook hardening model were used than written in the report. Furthermore, the Johnson-Cook damage model was mentioned in the report but not used in any model. It has been decided to keep the used value in the model as this is likely the value used to gain the results and also to check the influence. The Johnson-Cook hardening (B,c,n,m) variables of Ti-6Al-4V and Al-7075-T651 are given in Table 6.2. The A variable is the yield stress noted in Table 3.1. Al-7075-T651 has been chosen as no information about the Johnson-Cook variables of Al-7475 could be found and it is in the same series which should be a decent substitute. In the end it should be checked if the amount of energy absorbed due to plastic deformation is small enough to validate this choice.

Assumption 19 *The Johnson-Cook variables of Al-7075-T651 are similar to those of Al-7475.*

Table 6.1: Used material properties for Al2024-T361.

Variable	Value	Variable	Value	Variable	Value
Density [kg/m^3]	2780	c [-]	0	D_3 [-]	1.5
Elasticity modulus [N/m^2]	7.3*10^{10}	n [-]	0.73	D_4 [-]	0
Poisson ratio [-]	0.33	m [-]	0	D_5 [-]	0
A [N/m^2]	4.2*10^8	D_1 [-]	0.112		
B [N/m^2]	6.83*10^8	D_2 [-]	0.123		

Table 6.2: Johnson Cook properties of Ti-Al6-4V and Al-7074-T651. [42][7]

Variable	Ti-Al6-4V	Al-7074-T651	Variable	Ti-Al6-4V	Al-7074-T651
A [N/m^2]	1.05*10^9	4.29*10^8	D_1	-0.090	0.015
B [N/m^2]	1.09*10^9	4.05*10^8	D_2	0.270	0.24
c	0	0	D_3	0.480	-1.5
n	0.93	0.41	D_4	0	0
m	0	0	D_5	0	0

The dimensions and mesh sizes of individual components of the wing-fuselage are the same as used in Desiderio's model. These values are shown in Table 6.3 for each component and it can be noted that these are again slightly different from Desiderio's report. The mesh size of the engine mounting structure is 100 mm for all components.

Table 6.3: Thickness and mesh size of different components.

Part	Thick. [mm]	El. size [mm]	Part	Thick. [mm]	El. size [mm]
Skin	2.5	60	Floor long. beams	2	20
Frames	5.7	20	Spar skin	3	20
Struts	2	10	Spar stiffeners	4	20
Floor beams	2	30	Ground	0.1	200

6.3. Engine-impact model

In this section an engine-impact model is made in which the post-separation movement of the engine is modelled for various scenarios. This model is made to get an insight of the possible impact of the engine with the rest of the aircraft and thus if additional separation mechanisms are needed and if these will be helpful.

6.3.1. Loads

In order to find the direction of movement of the engine it is of importance to know the loads which are applied after separation. A total of five loads are applicable in this problem which are defined below.

1. **Gravity**, this causes a constant acceleration of 9.81 m/s^2 towards the Earth.
2. **Thrust**, it is assumed that the thrust upon separation is zero and remains zero after as no fuel is available.
3. **Lift**, any lift that is generated is ignored in this problem as it is assumed to be small.
4. **Drag**, this is caused due to interaction of the engine with the air during flight. This force is in the direction of the flow and the resulting acceleration can be calculated using Equation 6.23.

$$a_D = \frac{1}{2m_{eng}} C_D \rho A_{eng} v^2 \tag{6.23}$$

   Herein is m_{eng} the mass of the engine, C_D the drag coefficient, ρ the density of the air, A the characteristic frontal area of the engine and v the velocity of the engine with respect to the air.
5. **Friction**, this is caused by the interaction of the engine with the ground. This force goes against the direction of the velocity vector and can be calculated using Equation 7.23 for a flat surface.

$$a_F = \mu \cdot g \tag{6.24}$$

   Herein is μ the friction coefficient, which is assumed to be constant with velocity and g the gravitational acceleration.

The gravitational load is applied at the defined center of gravity whereas the drag and friction force are applied at the centroid. This induces a moment and will cause the engine to rotate. The angular acceleration can be calculated using Equation 6.25 and 6.26.

$$\alpha_D = 6 \frac{C_D \rho A_{eng} v^2 (L_{ct} - L_{cg})}{m_{eng}(L_{eng}^2 + 3r_{eng}^2)} \tag{6.25}$$

$$\alpha_F = 12 \mu g \frac{L_{ct} - L_{cg}}{L_{eng}^2 + 3r_{eng}^2} \tag{6.26}$$

Herein is L_{ct} and L_{cg} the length from the nose of the Flying-V to the centroid and center of gravity relatively, L_{eng} the length of the engine and r_{eng} the radius of the engine.

As the engine is rotating this means that the frontal area and drag coefficient are changing with time. To find this value the shape of the engine, including nacelle, is simplified to a cylinder as a lot of literature is available for this. The frontal area is easy to calculate for the case that the flow is directly parallel or perpendicular to the engine. However, when it is under angle around multiple axis it is more difficult to address it with goniometrics alone. For this reason the unit vector of the flow is used to determine the amount of area which is affected, which should give an accurate enough frontal area. This can be in math form found in Equation 6.27.

$$A_{eng} = \begin{bmatrix} \pi r_{eng}^2 \\ 2 r_{eng} L_{eng} \\ 2 r_{eng} L_{eng} \end{bmatrix} \cdot (\mathbf{R}_2 \mathbf{R}_1 \begin{bmatrix} \frac{|u(t)+u_{wind}|}{|v|} \\ \frac{|v(t)+v_{wind}|}{|v|} \\ \frac{|w(t)+w_{wind}|}{|v|} \end{bmatrix}) \tag{6.27}$$

Herein are u_{wind}, v_{wind} and w_{wind} the velocity of the wind and $u(t)$, $v(t)$ and $w(t)$ are the velocities of the engine in x, y and z-direction respectively. $|v|$ is the magnitude of the velocity vector as shown in Equation 6.28 and $\mathbf{R}_1$ and $\mathbf{R}_2$ are the rotation matrices shown in Equation 6.29 and 6.30.

$$|v| = \sqrt{(u(t) + u_{wind})^2 + (v(t) + v_{wind})^2 + (w(t) + w_{wind})^2} \tag{6.28}$$

$$\mathbf{R}_1 = \begin{bmatrix} \cos\theta\cos\phi & \cos\theta\sin\phi\sin\psi - \sin\theta\cos\psi & \cos\theta\sin\phi\cos\psi + \sin\theta\sin\psi \\ \sin\theta\cos\phi & \sin\theta\sin\phi\sin\psi + \cos\theta\cos\psi & \sin\theta\sin\phi\cos\psi - \cos\theta\sin\psi \\ -\sin\phi & \cos\phi\sin\psi & \cos\phi\cos\psi \end{bmatrix} \tag{6.29}$$

Herein is θ the yaw angle, ϕ the pitch angle and ψ the roll angle of the aircraft at the moment of separation.

$$\mathbf{R}_2 = \begin{bmatrix} \cos\phi\cos\psi & \sin\theta\sin\phi\cos\psi - \cos\theta\sin\psi & \cos\theta\sin\phi\cos\psi + \sin\theta\sin\psi \\ \cos\phi\sin\psi & \sin\theta\sin\phi\sin\psi + \cos\theta\cos\psi & \cos\theta\sin\phi\sin\psi - \sin\theta\cos\psi \\ -\sin\phi & \sin\theta\cos\phi & \cos\theta\cos\phi \end{bmatrix} \tag{6.30}$$

This time θ, ϕ and ψ are the angular orientations of the engine about the x,y and z-axis with respect to the orientation of the aircraft.

The drag coefficient of the engine also changes with different orientation and Reynolds number. The Reynolds number for engine separation is in the order of 10^7. There is very little information available about subsonic flow at such a high Reynolds number and especially about inclined cylinders and even less about cylinders rotated around multiple axis. Literature of single-axis inclined cylinders at lower Reynolds numbers (10^3 to 10^4) show that the drag increases first and decreases again after 45 degrees being slightly higher at 90 degrees than 0 degrees [15]. Furthermore, other literature shows that the drag coefficient of cylinder at 90 degrees stabilizes around $Re = 10^7$ to a value of $C_D = 0.7$ slightly lower than at previous mentioned Reynolds numbers [26]. Combining these conclusions would probably not result in a more accurate simulation as it would be guess work. Due to lack of good data it has chosen to use a constant value of $C_D = 0.7$ and do a sensitivity analysis afterwards.

6.3.2. Configuration

The moment of separation can occur in various scenarios. Considering the possible fatalities during impact it is of high importance that all these possible scenarios should be assessed. However, to keep it simple, it has been decided to keep it with a simple crash with only a horizontal component, without any initial yaw angle. Furthermore two types of separation are investigated. In first simulation the engine is separated at both connection types at the same time, dropping horizontally. The second simulation separates first at the front connection such that a pendular motion is initiated and separates at the aft mount the moment the engine touches the ground. These two situations are depicted in Figure 6.8.

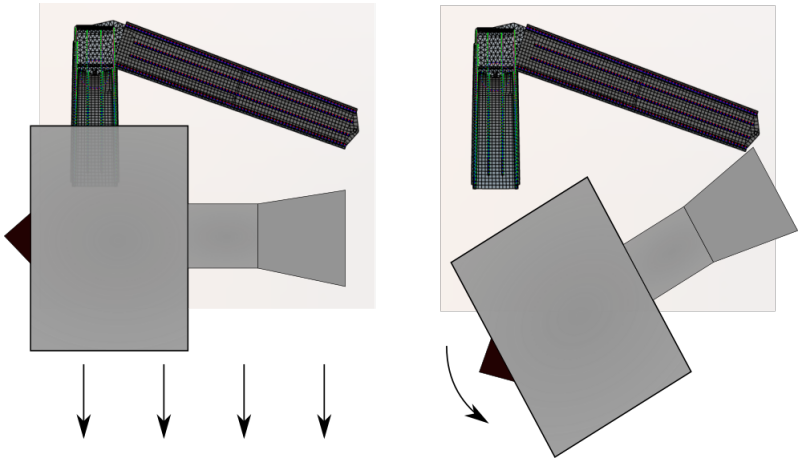

Figure 6.8: Graphical image of the two cases of engine separation.

Due to the pendular motion the second simulation starts with an initial velocity, which is equal to the angular velocity multiplied by the length. The angular velocity can be calculated using Equation 6.31.

$$v = \omega \cdot \frac{2}{3}L = \sqrt{\frac{2g}{L}(\cos\theta - \cos\theta_0)} \cdot \frac{2}{3}L \tag{6.31}$$

The velocity would be maximal if the engine could be separated once it is vertically. However, the length of the engine is almost twice the distance between engine and and the distance to the ground which means that it can not reach that value. The maximum angle that the engine can reach is $\theta = 61.2°$, substituting this and $\theta_0 = \frac{\pi}{2}$ in the equation above gives an initial velocity of 4.94 m/s, whereof 2.38 m/s in the x-direction. This also shifts the engine slightly backwards and allows friction to happen at the start of the separation.

Both of these scenarios consider similar flight velocity, air density, wind velocity and pitch and roll angles. The flight velocity that is going to be considered is the approach velocity which is 70.5 m/s for the Flying-V 1000 [31]. The approach velocity has been chosen as most fatal accidents occur during the final approach and landing according to Boeing's 2022 statistical summary of commercial jet airplane accidents [38]. It is acknowledged that this approach velocity is under an angle resulting in a lower horizontal velocity component, however, for conservative reasons it has been kept this way. This means that the following velocity is going to be considered:

$$u_{ini} = 70.5\ ms^{-1}$$

The air density that is going to be considered:

$$\rho = 1.225\ kgm^{-3}$$

The wind velocities that are going to be considered:

$$u_{wind} = [-15, 0, 15]\ ms^{-1}$$
$$v_{wind} = [0, 0, 0]\ ms^{-1}$$
$$w_{wind} = [0, 0, 0]\ ms^{-1}$$

6.3.3. Modelling method

The position of the engine's center of gravity over will be calculated using Equation 6.32.

$$\begin{bmatrix} x(t+dt) \\ y(t+dt) \\ z(t+dt) \end{bmatrix} = \frac{1}{2} \cdot dt^2 \cdot \begin{bmatrix} a_x(t) \\ a_y(t) \\ a_z(t) \end{bmatrix} + dt \cdot \begin{bmatrix} u(t) \\ w(t) \\ z(t) \end{bmatrix} + \begin{bmatrix} x(t) \\ y(t) \\ z(t) \end{bmatrix} \tag{6.32}$$

Herein are x, y and z the position of the engine, a_x, a_y and a_z the accelerations at t and u, w and z the velocity of the engine in x, y and z-direction respectively. The variables t and dt are the respective timestep

The velocities of the engine can be calculated using Equation 6.33.

$$\begin{bmatrix} u(t+dt) \\ v(t+dt) \\ w(t+dt) \end{bmatrix} = dt \cdot \begin{bmatrix} a_x(t) \\ a_y(t) \\ a_z(t) \end{bmatrix} + \begin{bmatrix} u(t) \\ w(t) \\ z(t) \end{bmatrix} \tag{6.33}$$

These new velocities are used to update the drag acceleration. These accelerations are updated every time step, dt, and can be calculated as using Equation 6.34

$$\begin{bmatrix} a_x(t+dt) \\ a_y(t+dt) \\ a_z(t+dt) \end{bmatrix} = \begin{bmatrix} 0 \\ 0 \\ -9.81 \end{bmatrix} + \frac{1}{2m_{eng}} C_D \rho A_{eng} |v| \begin{bmatrix} u(t)+u_{wind} \\ v(t)+v_{wind} \\ w(t)+w_{wind} \end{bmatrix} + \frac{9.81\mu}{|u|} \begin{bmatrix} u(t) \\ v(t) \\ w(t) \end{bmatrix} + \begin{bmatrix} a_x(0) \\ a_y(0) \\ a_z(0) \end{bmatrix} \tag{6.34}$$

Herein are u_{wind}, v_{wind} and w_{wind} the direction of the wind affecting the flow, $|v|$ is the magnitude of the velocity vector v as shown in Equation 6.28 and $|u|$ is the magnitude of the velocity vector u as shown

in Equation 6.35. It should be noted that the initial accelerations are only there at t = 0 and are 0 for the rest of the time. Furthermore, the friction term is there once the engine reaches the ground.

$$|u| = \sqrt{u(t)^2 + v(t)^2 + w(t)^2} \tag{6.35}$$

The orientation of the engine is dependent on the rotation of the engine, and can be calculated using Equation 6.36. Herein is the rotation around the longitudinal axis ignored as this does not change the geometrical orientation.

$$\begin{bmatrix} \theta(t+dt) \\ \phi(t+dt) \\ \psi(t+dt) \end{bmatrix} = \frac{1}{2} \cdot dt^2 \cdot \begin{bmatrix} \alpha_x(t) \\ \alpha_y(t) \\ \alpha_z(t) \end{bmatrix} + dt \cdot \begin{bmatrix} \omega(t) \\ \zeta(t) \\ \xi(t) \end{bmatrix} + \begin{bmatrix} \theta(t) \\ \phi(t) \\ \psi(t) \end{bmatrix} \tag{6.36}$$

Herein are θ, ϕ and ψ the angular orientation, α_x, α_y and α_z the angular accelerations, ω, ζ and ξ the angular velocity of the engine.

The angular accelerations can be calculated using Equation 6.37.

$$\begin{aligned} \begin{bmatrix} \alpha_x(t+dt) \\ \alpha_y(t+dt) \\ \alpha_z(t+dt) \end{bmatrix} &= 6\frac{C_D \rho A_{eng}|v|}{m_{eng}(L_{eng}^2 + 3r_{eng}^2)} \cdot ((\mathbf{R_2}\mathbf{R_1} \begin{bmatrix} L_{ct} - L_{cg} \\ 0 \\ 0 \end{bmatrix}) \times \begin{bmatrix} u(t) + u_{wind} \\ v(t) + v_{wind} \\ w(t) + w_{wind} \end{bmatrix}) \\ &+ \frac{12\mu g}{(L_{eng}^2 + 3r_{eng}^2)|u|} \cdot ((\mathbf{R_2}\mathbf{R_1} \begin{bmatrix} L_{ct} - L_{cg} \\ 0 \\ 0 \end{bmatrix}) \times \begin{bmatrix} u(t) \\ v(t) \\ w(t) \end{bmatrix}) + \begin{bmatrix} \alpha_x(0) \\ \alpha_y(0) \\ \alpha_z(0) \end{bmatrix} \end{aligned} \tag{6.37}$$

Herein are α_{xini}, α_{yini} and α_{zini} the initial angular accelerations and $\mathbf{R_2}$ is the rotation matrix similar to shown in Equation 6.30. It should again be noted that the initial angular accelerations are only there at t = 0 and 0 afterwards and that the effect of the normal force on the rotation of the engine is ignored. In order to have a better model this needs to be included to have a better idea of the orientation and position of the engine. However, for this research it is assumed that after separation for both cases the engine is directly aligned with the aircraft. This also means that the rotation will be negligible for the two separation cases.

Assumption 20 *The initial rotation after engine separation for the rotational separation case has only a small effect on the final results.*

During the crash, the velocity of the aircraft will change due to air resistance and friction. These need to be taken into account to find the relative position of aircraft and engine. The position of the aircraft can be calculated using Equation 6.32 and 6.33 and Equation 6.38 below.

$$\begin{bmatrix} a_x(t+dt) \\ a_y(t+dt) \\ a_z(t+dt) \end{bmatrix} = \frac{1}{2m_c} C_D \rho A_c |v| \begin{bmatrix} u(t) + u_{wind} \\ v(t) + v_{wind} \\ w(t) + w_{wind} \end{bmatrix} + \frac{9.81\mu}{|u|} \begin{bmatrix} u(t) \\ v(t) \\ w(t) \end{bmatrix} \tag{6.38}$$

As mentioned before, in this study the rotation of the aircraft is excluded as only a simple crash scenario is considered, with an horizontal component, without any initial rotation. Which means that the bulk of the forces align with the center of gravity and thus does not cause any rotation. Furthermore, the design is still in its early stages which means that the center of gravity and centroid will shift based on future design choices, which will deem the calculated rotations inaccurate.

Recommendation 26 *In future research the rotation of the aircraft should also be taken into account which can be done using a similar approach as done for the engine.*

The values for m_c is from Oosterom [31] and C_D and A_c are from Hillen [17].

$$\begin{aligned} m_c &= 275000 - 2 \cdot 10950 = 253100\ kg \\ C_D &= 0.146 \\ A_c &= 2050\ m^2 \end{aligned}$$

Using this the positioning of the aircraft and engine can be found after the separation for all conditions and several configurations.

Lastly, it is acknowledged that the interaction between engine and aircraft has been ignored. The effect of the aircraft on the flow interacting with the engine is thought to be significant. However, overall, the simulations should still give an impression if continuation on the topic of separation for the Flying-V is necessary.

7

Results and Discussions

In this section the results from the optimization of the engine mounting structure and mentioned crash-worthiness analysis of this optimized structure are discussed. This includes a mesh convergence study for the engine mounting structure and a sensitivity analysis of the crashworthiness analysis in order to see the effect of some assumptions and variables.

7.1. Mesh convergence

The mesh convergence for the engine mounting structure is done using only TO-04, the initial design parameters as in Section 5.5.1 and the maximum displacement as comparison value. It has been chosen to keep the mesh convergence simple and use the same mesh size for all parts. The results from this mesh convergence study is shown in Table 7.1.

Table 7.1: Results of the mesh convergence study using TO-04 and maximum displacement.

Mesh size [mm]	200	175	150	125	100	75	50
Max displacement [mm]	213.829	159.785	169.792	176.391	190.34	194.661	207.076
Difference [%]	-	25.27	6.26	3.89	7.91	2.27	6.38

This shows that the mesh does not convergence as deviations remain larger than 1%, smaller mesh sizes could not be used due to a limit of elements that the software allows. Previous mesh size analysis shows a convergence at a mesh size of 150 mm. It seems that this is also the case in this situation but it diverges afterwards again, this is thought to be the result of the tie connections between parts however no exact reason could be found. Further investigation requires to replace the tie connections with a more detailed way which is beyond the scope of this research and therefore it has been decided to use a mesh size of 150 mm while taking into account that the results may be inaccurate.

Due to time limits it has been decided to use the same mesh size for the engine mounting structure for the vertical drop-test simulations. For similar reasons no mesh convergence is done for the extended wing-fuselage of the Flying-V, as this has been done extensively by Desiderio [10]. It is noted that the engine mounting has a significant effect on the results and thus a new mesh convergence study is required. However, as it is a comparison study and no exact values are required it was considered acceptable for this research.

7.2. Engine mounting structure

The optimization of the engine mounting structure took a total of 4 iterations, using a damping parameter of 0.7. The minimum MoS, average negative MoS, number of elements with a negative MoS and resultant mass of each iteration is shown in Table 7.2. It should be noted that the number of elements with a negative MoS counts per loadcase thus an element with a negative MoS in two loadcases counts as 2 in this parameter. The MoS of each part and the corresponding loadcase and failure mode are shown for the first and last iteration in Figures 7.1 to 7.3. Similar figures for iteration 1 to 3 can be found

in Chapter B. It should be noted that the maximum MoS shown is capped at 2 such that the differences within the desired range remains clear. This means that the real MoS might be higher when a value of 2 is shown.

Table 7.2: Mass, minimum MoS, nr of elements with negative MoS and average negative MoS for each iteration.

Iteration nr. [-]	0	1	2	3	4
Mass [kg]	3485	4240	4591	4707	4890
Min MoS [-]	-0.86	-0.39	-0.40	-0.48	-0.64
Nr of elements with negative MoS [-]	61	44	50	49	26
Average negative MoS [-]	-0.30	-0.17	-0.13	-0.17	-0.20

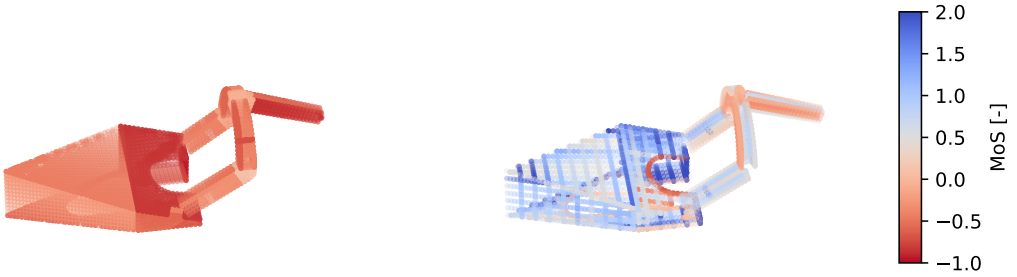

Figure 7.1: Minimum MoS values of panels (left) and stiffeners (right) before first iteration, showing that most panels have a negative MoS while most stiffeners are within the desired region.

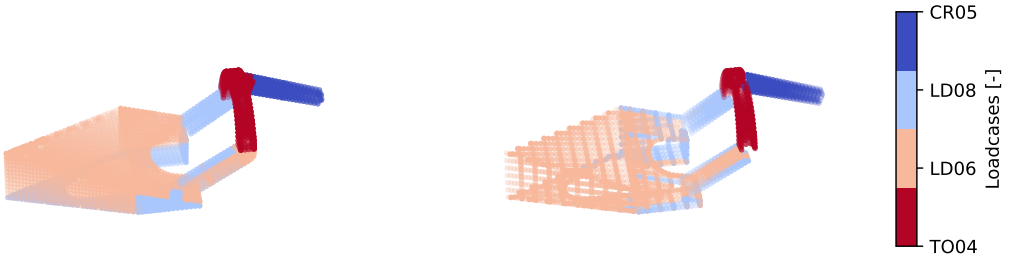

Figure 7.2: Responsible loadcase for minimum MoS values of panels (left) and stiffeners (right) before first iteration, showing that every considered loadcase has influence on the optimization of the structure.

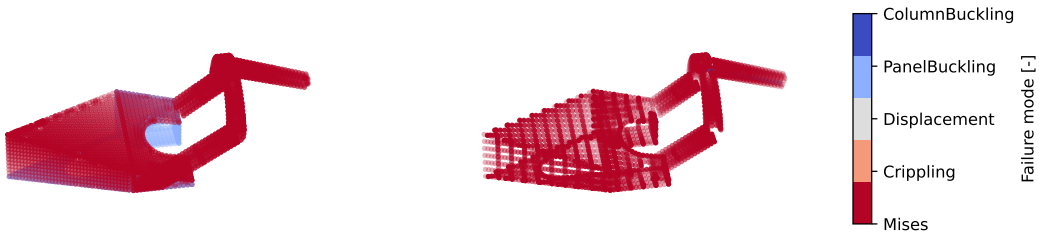

Figure 7.3: Responsible failure mode for minimum MoS values of panels (left) and stiffeners (right) before first iteration, showing the criticality of the von Mises stress.

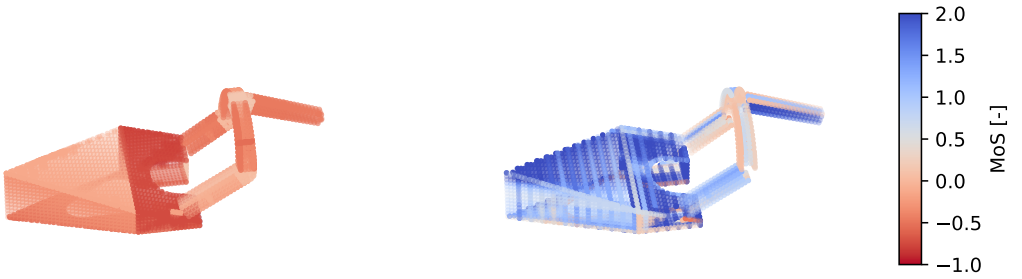

Figure 7.4: Minimum MoS values of panels (left) and stiffeners (right) of last iteration, showing an overall decreasing MoS except for the panels with stress concentrations.

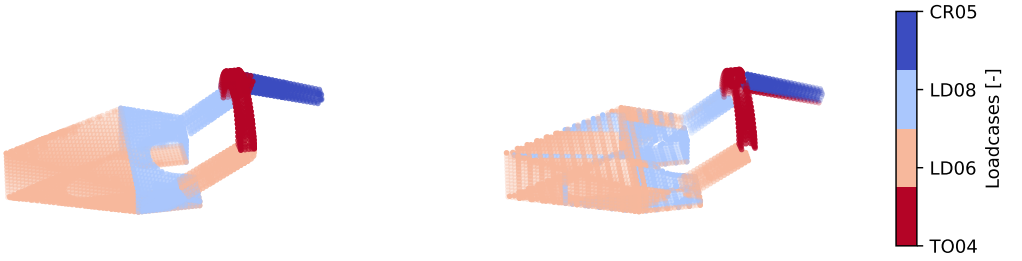

Figure 7.5: Responsible loadcase for minimum MoS values of panels (left) and stiffeners (right) of last iteration, showing that even after some iterations the critical loadcase remains the same for most elements.

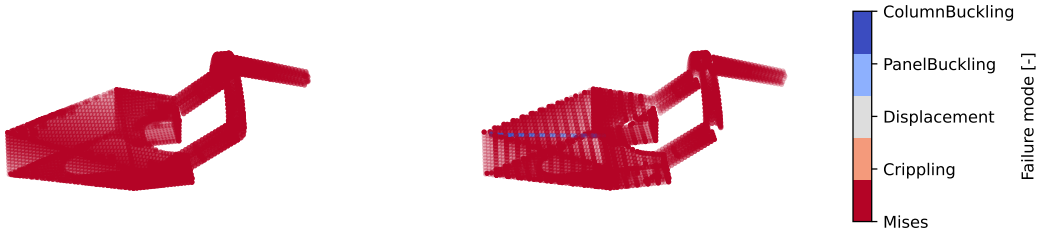

Figure 7.6: Responsible failure mode for minimum MoS values of panels (left) and stiffeners (right) of last iteration, showing that von Mises remains the most critical failure mode.

Before the optimization it has been decided to exclude some loadcases (CR01,CR02,TO05) which have proven to have limited to no effect on the final structure. Therefore, one iteration has been done with the last iteration in the optimization research to validate this assumption. The result of this verification is shown in Figure 7.7 to 7.9 on the next page. The minimum Mos remains the same at -0.64 but the number of element with a negative MoS increase to 46 and the average negative MoS increases to -0.17.

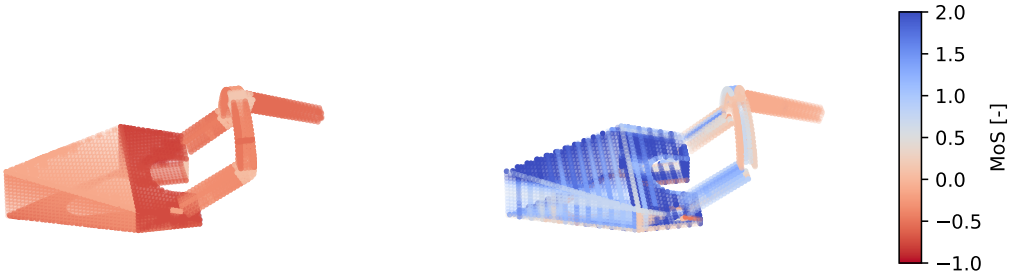

Figure 7.7: Minimum MoS values of panels (left) and stiffeners (right) of verification iteration, showing an increase in MoS at the overhead beams compared to the final iteration of the optimization.

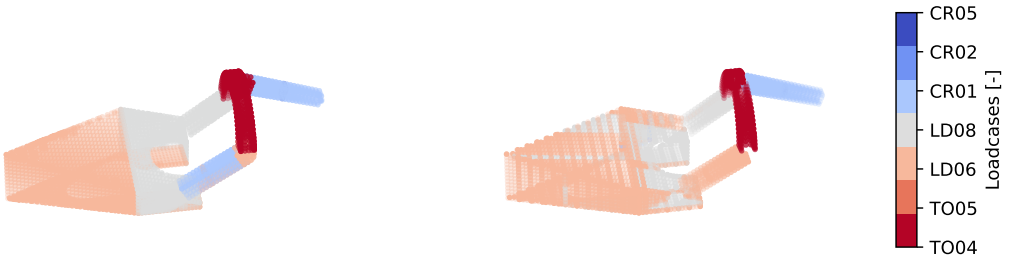

Figure 7.8: Responsible loadcase for minimum MoS values of panels (left) and stiffeners (right) of verification iteration, showing that for the final design CR01 is more critical than CR05.

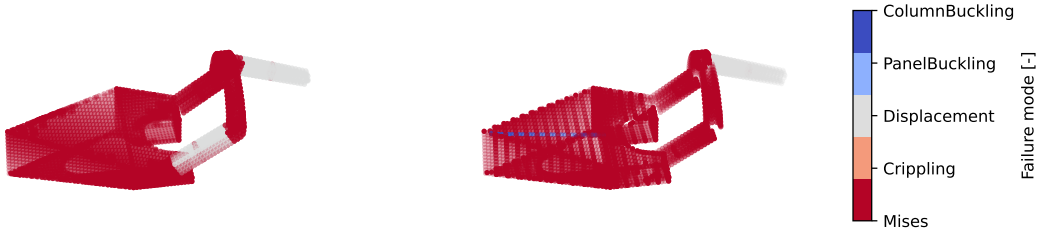

Figure 7.9: Responsible failure mode for minimum MoS values of panels (left) and stiffeners (right) of verification iteration, showing that the increased MoS at the overhead beams is due to the displacement criteria.

The final dimensions of the part for the last iteration with the initial input specified in Section 5.5.1 are noted in Table 7.3 to 7.9 below.

Table 7.3: Final dimensions for OH1.

Parameter	Value	Type	Parameter	Value[1]	Type
Width 1 [mm]	400	Input	Stiffeners 1 dim. [mm]	[100, 50, 10, 10]	Input
Height 1 [mm]	450	Input	Stiffeners 2 dim. [mm]	[100, 50, 10, 10]	Input
Width 2 [mm]	360	Input	Corner stiffener dim. [mm]	[53.3, 53.3, 7.1, 7.1]	Input
Height 2 [mm]	390	Input	Panel thicknesses [mm]	[7.2, 5.5, 8.8, 10.1]	Input
Nr of stiffeners 1 [-]	2	Input	Nr of ribs [-]	1	Input
Nr of stiffeners 2 [-]	2	Input	Rib thicknesses [mm]	2.8	Input

Table 7.4: Final dimensions for OH2.

Parameter	Value	Type	Parameter	Value[1]	Type
Width 1 [mm]	500	Input	Stiffeners 1 dim. [mm]	[100, 50, 10, 10]	Input
Height 1 [mm]	520	Input	Stiffeners 2 dim. [mm]	[100, 50, 10, 10]	Input
Width 2 [mm]	440	Input	Corner stiffener dim. [mm]	[53.2, 53.2, 7.1, 7.1]	Input
Height 2 [mm]	460	Input	Panel thicknesses [mm]	[5, 6.2, 5.5, 5.8]	Input
Nr of stiffeners 1 [-]	2	Input	Nr of ribs [-]	1	Input
Nr of stiffeners 2 [-]	2	Input	Rib thicknesses [mm]	3.0	Input

[1]The index in the array for panel thicknesses refers to the panel numbers shown in Figure 5.6. The dimensions for the stiffeners are listed as follows: [End-to-end height, flange width, web thickness, flange thickness]

Table 7.5: Final dimensions for OH3.

Parameter	Value	Type	Parameter	Value[1]	Type
Width 1 [mm]	500	Input	Stiffeners 1 dim. [mm]	[100, 50, 10, 10]	Input
Height 1 [mm]	520	Input	Stiffeners 2 dim. [mm]	[100, 50, 10, 10]	Input
Width 2 [mm]	440	Input	Corner stiffener dim. [mm]	[49.7, 49.7, 6,6, 6.6]	Input
Height 2 [mm]	460	Input	Panel thicknesses [mm]	[5, 5.9, 6.9, 6.0]	Input
Nr of stiffeners 1 [-]	2	Input	Nr of ribs [-]	1	Input
Nr of stiffeners 2 [-]	2	Input	Rib thicknesses [mm]	2.8	Input

Table 7.6: Final dimensions for OH4.

Parameter	Value	Type	Parameter	Value[1]	Type
Width 1 [mm]	500	Input	Stiffeners 1 dim. [mm]	[100, 50, 10, 10]	Input
Height 1 [mm]	520	Input	Stiffeners 2 dim. [mm]	[100, 50, 10, 10]	Input
Width 2 [mm]	520	Input	Corner stiffener dim. [mm]	[36.6, 36.6, 4.9, 4.9]	Input
Height 2 [mm]	500	Input	Panel thicknesses [mm]	[5, 6.1, 5, 6.1]	Input
Nr of stiffeners 1 [-]	2	Input	Nr of ribs [-]	1	Input
Nr of stiffeners 2 [-]	2	Input	Rib thicknesses [mm]	1.0	Input

Table 7.7: Final dimensions for OH5.

Parameter	Value	Type	Parameter	Value[1]	Type
Width 1 [mm]	500	Input	Stiffeners 1 dim. [mm]	[100, 50, 10, 10]	Input
Height 1 [mm]	520	Input	Stiffeners 2 dim. [mm]	[100, 50, 10, 10]	Input
Width 2 [mm]	520	Input	Corner stiffener dim. [mm]	[130.4, 130.4, 17.4, 17.4]	Input
Height 2 [mm]	500	Input	Panel thicknesses [mm]	[5, 5.1, 5, 5.1]	Input
Nr of stiffeners 1 [-]	2	Input	Nr of ribs [-]	1	Input
Nr of stiffeners 2 [-]	2	Input	Rib thicknesses [mm]	1.1	Input

Table 7.8: Final dimensions for SSLB.

Parameter	Value[1]	Type
Panel thicknesses [mm]	[12.3, 7.3, 3.4, 2.1, 1.1, 1.6, 13.0, 14.4]	Input
Nr of stiffeners 1 [-]	16	Input
Nr of stiffeners 2 [-]	21	Input
Nr of stiffeners 3 [-]	12	Input
Stiffeners 1 dim. [mm]	[210.8, 151.8, 6.7, 6.7]	Input
Stiffeners 2 dim. [mm]	[140.6, 140.6, 12.3, 12.3]	Input
Stiffeners 3 dim. [mm]	[148.3, 59.3, 10.5, 10.5]	Input
Corner stiffener dim. [mm]	[93.7, 52.5, 3.4, 3.4]	Input

Table 7.9: Final dimensions for the joints.

Parameter	Value	Type	Parameter	Value	Type
Thickness OH12 [mm]	20.7	Input	Thickness SSLB4 [mm]	15	Input
Thickness OH24 [mm]	15	Input	Thickness SSLB5 [mm]	15	Input
Thickness OH35 [mm]	12.5	Input	Location SSLB5 along panel [mm]	400	Input

[1]The index in the array for panel thicknesses refers to the panel numbers shown in Figure 5.6. The dimensions for the stiffeners are listed as follows: [End-to-end height, flange width, web thickness, flange thickness]

7.2.1. Discussion

The applied method has not proven to be able to reduce all MoS to a positive value. However, it does not mean that the applied method is inherently bad but rather it is not complete. The applied method shows that it is able to reduce the number of elements with a negative MoS quite successfully after a few iterations. The remaining elements are due to a few stress concentrations, mostly occurring at the tie connections, which could not be solved using the method. The final 26 number of elements are not the result of 26 stress concentrations but rather due to the location of these stress concentrations and the fact that an element can be counted more than once if multiple loadcases result in a negative MoS. The location of most of these stress concentration is at a point where multiple panels and stiffeners connect and thus share nodes which results that multiple elements have the same MoS. In short, this means that a single stress concentration causes an increase of a significant amount of elements in the 'Nr of elements with negative MoS' criteria. Furthermore, these stress concentrations increase in magnitude for some iterations which decreases the minimal MoS and with that also the average negative MoS even though for most elements the MoS increases. This increase in magnitude is thought to be due to increase of local differences of in-plane stiffness but this requires further investigation.

The initial results in Figure 7.1 show that most of the panels are below the required MoS whereas most stiffeners easily within the range. Furthermore, the von Mises criterion is the most critical for most parts, which might be the result of above mentioned stress concentrations and the fact that only a limited amount of failure modes are considered for the overhead beams. The results also shows that all four load cases have an influence on the iterations as all cause a minimum MoS in at least one element as shown in Figure 7.2 and 7.5. This is not the case in the validation iteration, which also considers the loadcases not used for optimization. This iteration shows that CR-01 is more prominent and CR-05 is completely excluded from the picture. Herefrom can be concluded that CR-02 and TO-05 are indeed less severe and can be excluded in future optimization studies. Furthermore, CR-01 should be added to the optimization study and CR-05 should be further investigated by analysing more cases as the structure might already been mostly optimized for this loadcase. The reason that CR-01 became much more prominent in this study compared to previous might be due to the significant change in estimated engine mass. Another conclusion that can be drawn is that most of the MoS added by CR-01 this loadcase are small as the average negative MoS reduces. From Figure 7.4 should also be noted that a lot of elements are within the desired range of MoS due to grouping of parameters and thus further mass optimization remains possible.

Although the structure is not fully optimized the current analysis still gives a rough estimation of the final mass of the engine mounting structure, which is estimated to be in the high 4000s. It is expected that the final mass will be lower than the last iteration shown in Table 7.2 as the low MoS, due to the stress concentrations, cause an unnecessary high increase in thickness of stiffeners and panels in multiple iterations without having effecting these stress concentrations. One could at least conclude that the resultant engine mounting structure will be significantly heavier compared to 3411 kg found in previous research, having a negative effect on the viability of the Flying-V.

Lastly, one should realise that this is optimization is only for the initial design parameters. In order to find the optimal design different starting designs, with different parameter ratios, need to be analysed as mentioned in Section 5.5.1. This includes other design parameters excluded from the optimization method, such as material, location of center of gravity of the engine and the location of SSLB5 along the panel. These parameters were mend to be analysed in an sensitivity analysis, however it has been decided to exclude this due to the duration of a full optimization loop and the limited additional value to this research.

Recommendation 27 *The connection between the joints and panels should be further investigated in future studies to prevent stress concentrations.*

Recommendation 28 *Future research should include above mentioned parameters into their optimization analysis.*

7.3. Crashworthiness

The vertical drop test scenario as described in Section 6 is done using an non-optimized engine mounting structure due to the limited time available using a computer cluster. There was access to a bigger and better computer cluster than TU Delft has till a specific date, which has a big influence on the total research time due to the size of the simulations. Therefore it has been chosen to first assess the crashworthiness before optimizing the structure, which can be done on a normal computer. This will have an impact on the result but this should be limited as the engine plus landing gear are more than 75% of the total mass and the difference between the used 3483 kg engine mounting structure and the estimated optimized structure is only approximately 5% of the total mass. The used variables are the same as the initialization noted in Section 5.5.1.

7.3.1. Elongated fuselage

As mentioned before, Desiderio already has shown that additional frames do not affect the crashing behavior for 4 to 6 frames for a normal fuselage. Simulations are performed and compared to Desiderio's case in an attempt to validate this assumption for the Flying-V. This is a simulation with the extended wing-fuselage but without the engine mounting structure. The results are shown below in Figure 7.10 and 7.11 and Table 7.10. Herein is K_{eg} the kinetic energy and E_D the dissipated plastic energy.

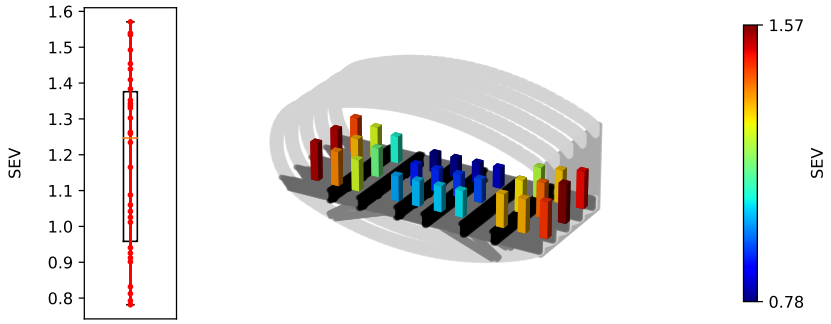

Figure 7.10: SEV of Desiderio's model with damage properties, used as the base model.

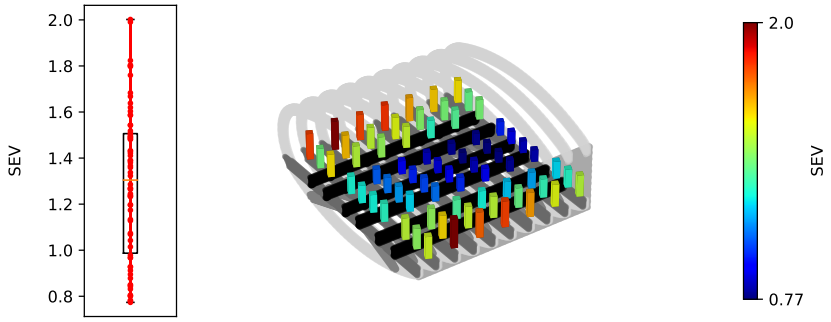

Figure 7.11: SEV of elongated model with damage properties, showing a similar distribution but large difference in SEV compared to the base model.

Table 7.10: Median SEV and dissipated energy per section for Desiderio's and elongated simulations, showing a large difference in energy absorption of frames and floor beams. Note, the values of the components might not add up to the total energy dissipated, due to rounding errors and the fact that the limited absorption of the spar is excluded.

Energy	Desiderio	Elong. fuselage
Initial K_{eg} [kJ]	128.83	291.28
Total $\frac{E_D}{K_{eg}}$[%]	70.74	68.65
-Skin [%]	12.00	9.55
-Frames [%]	33.96	25.18
-Struts [%]	10.19	10.24
-Floor beams [%]	6.39	12.25
-Floor long beams [%]	7.94	10.02
Friction [kJ]	4.59	7.79
Median SEV [-]	1.25	1.30

The simulations of Desiderio initially did not include the damage parameters, which was thought to have a big effect on the results above as it reduces the stiffness. In order to confirm this hypothesis simulations are done without the damage parameter and the results are shown in the Figure 7.12 and 7.13 below.

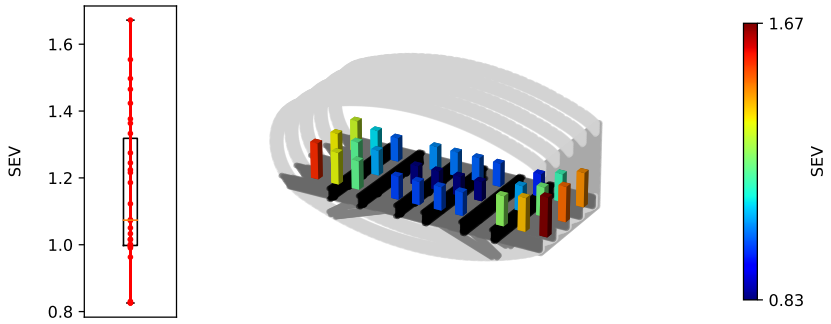

Figure 7.12: SEV of Desiderio's model without damage properties, showing a small increase of SEV when damage properties are considered.

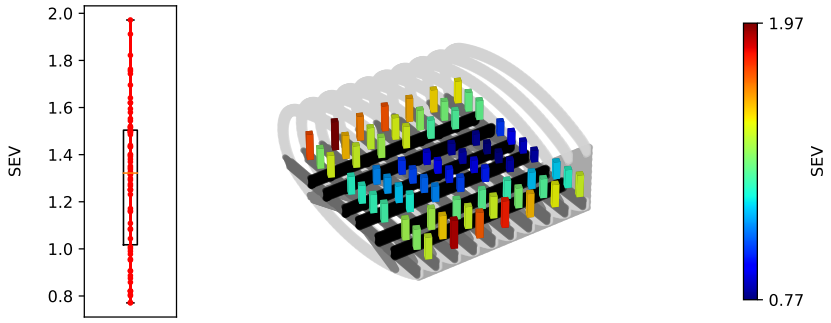

Figure 7.13: SEV of elongated model without damage properties, showing a small increase of SEV when damage properties are considered.

The SEV from the first simulations could have been influenced by other factors. Therefore more simulations have been done to sort out possible differences. Firstly, the number of passenger rows per frame has been reduced from 0.7 to 0.6, such that it is constant with Desiderio's simulation. The results are shown in Figure 7.14. This simulation was done before any damage parameters were added.

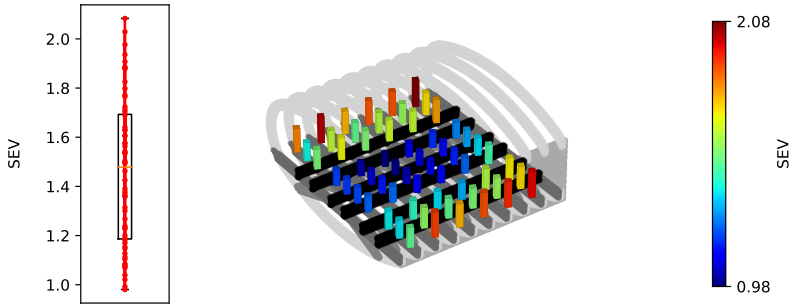

Figure 7.14: SEV of elongated model with 6 rows of seats and without damage, showing an increase in SEV for a lower ratio of passenger rows per frame.

As above still does show a difference it is thought that the out-of-plane buckling could affect the results. Desiderio's model is smaller which might reduce the stiffness due to above effect compared to the elongated one. Therefore a sliding boundary condition has been added on the continuous elements, such a skin, spar and longitudinal beams, for both simulations. This boundary condition means that these elements can not deform out of plane. These simulations are done using the same number of passenger rows per frame and before damage parameters were added. The results of these simulations are shown in Figure 7.15 and 7.16.

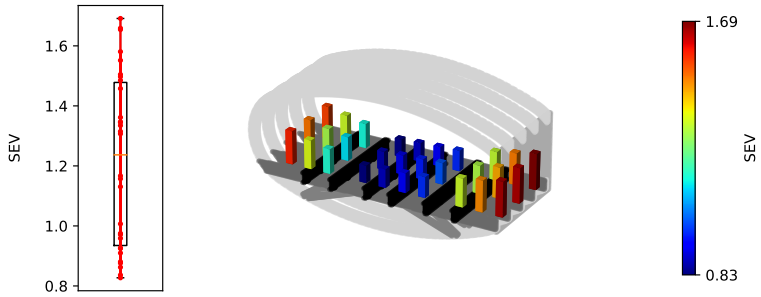

Figure 7.15: SEV of Desiderio's model with sliding boundary conditions and without damage, showing a more smooth distribution and a slightly lower SEV.

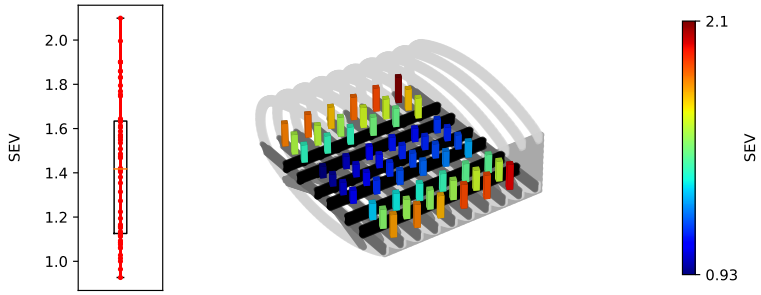

Figure 7.16: SEV of elongated model with 6 rows of seats, with sliding boundary conditions and without damage, showing a more smooth distribution and a slightly lower SEV.

Discussion
It was expected that the elongation of the Flying-V had almost no influence as additional mass and surface area are added in a similar relation as the normal fuselage. However, a large difference between the maximum in Desiderio and the elongated one could be found. It was thought that this could be due to the larger ratio of frames per passenger row but reducing the number of passenger rows by 1 to obtain the same ratio increases the SEV instead which was not expected. This increase in SEV is due to higher deaccelerations which is expected to be due to additional stiffness of the less deformed frame. Applying a sliding boundary condition makes both cases stiffer at the sides, resulting in a more smooth distribution of the SEV over the fuselage but still does not make both cases slightly more comparable. The difference in SEV between Desiderio's model and the elongated model can be explained due to the difference in energy absorption of each component but no reason could be found or thought of that explains the existence of this difference. Therefore the conclusion has been made that, in order to get accurate results the full fuselage needs to be taken into account.

Above conclusion does not make the rest of the simulations obsolete as the exact values of SEV are less of an interest. The current method still allows to compare different cases and draw conclusions on the effect of the differences. Furthermore, it has been decided to continue with 7 rows of passengers as the reduced loads of 6 rows reduce the validity of the results. In the current design the frame spacing (650 mm) is lower than the seat spacing (892 mm), which means that the ratio between these two numbers is closer to 0.7 than 0.6. In addition, including the damage properties indeed has a significant effect on the SEV and should therefore be included in all future simulations. Lastly, it is thought that the addition of the sliding boundary conditions results in a more realistic simulation, due to the reduction of deformation at the sides of the model. However, it will not be included in future simulations as a simulation with boundary conditions resulted in simulation times of almost 52 hours compared to less than 4 hours without.

The local differences in SEV along the length of the wing-fuselage is likely due to two things. Firstly, different spacing of the seats cause one seat to be directly above a floor beam and another seat between the floor beams. Secondly, the lack of boundary conditions at the edges allow the wing-fuselage to rotate more during deformation. This second effect is shown in Figure 7.15 and 7.16, removing these rotations gives a more anticipated SEV distribution over the fuselage. These figures also show more evidently that the side of the spar is stiffer resulting in higher SEV values.

7.3.2. Inertia effect

Apart of the elongation, Desiderio also excludes the effect of the rest of the aircraft. This might have negligible effect if the rotations, even after impact, are minimum. Regardless, it should first be checked if the added inertia properties influence the results itself. Therefore a simulation is performed of the elongated simulation with inertia effects and compared with the simulation in previous section. The results are shown below in Figure 7.17 and Table 7.11. Herein is K_{eg} the kinetic energy and E_D the dissipated plastic energy.

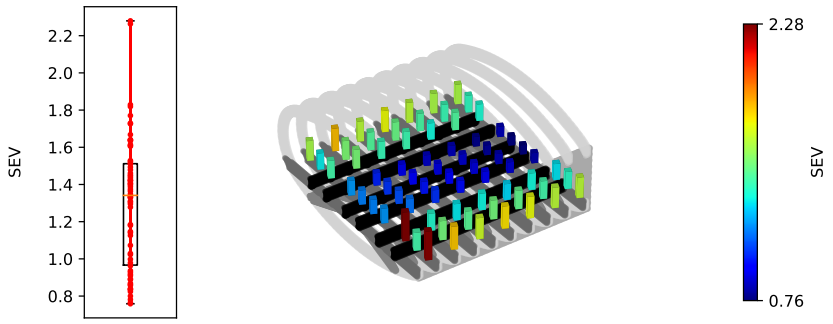

Figure 7.17: SEV of elongated model with added inertia properties, showing the overall limited effect of the added inertia.

Table 7.11: Median SEV and dissipated energy per section for elongated and inertia simulations. Note, the values of the components might not add up to the total energy dissipated, due to rounding errors and the fact that the limited absorption of the spar is excluded.

Energy	Elong. fuselage	Elong. fuselage with inertia
Initial K_{eg} [kJ]	291.28	291.35
Total $\frac{E_D}{K_{eg}}$[%]	68.65	68.11
-Skin [%]	9.55	10.28
-Frames [%]	25.18	26.49
-Struts [%]	10.24	10.35
-Floor beams [%]	12.25	10.87
-Floor long beams [%]	10.02	8.26
Friction [kJ]	7.79	7.39
Median SEV [-]	1.30	1.34

Before the simulation with engine mounting structure is performed a simulation of the effect of the inertia is done. Therefore, two drop-test are performed of the non-optimized structure wherein one has the inertia added and the other one does not. The effect of the non-optimized engine mount structure compared to the optimized structure should have negligible effect on this analysis, as the outcome is only assessed visually. The final frame of the drop-tests at 0.3 seconds are shown in Figure 7.18.

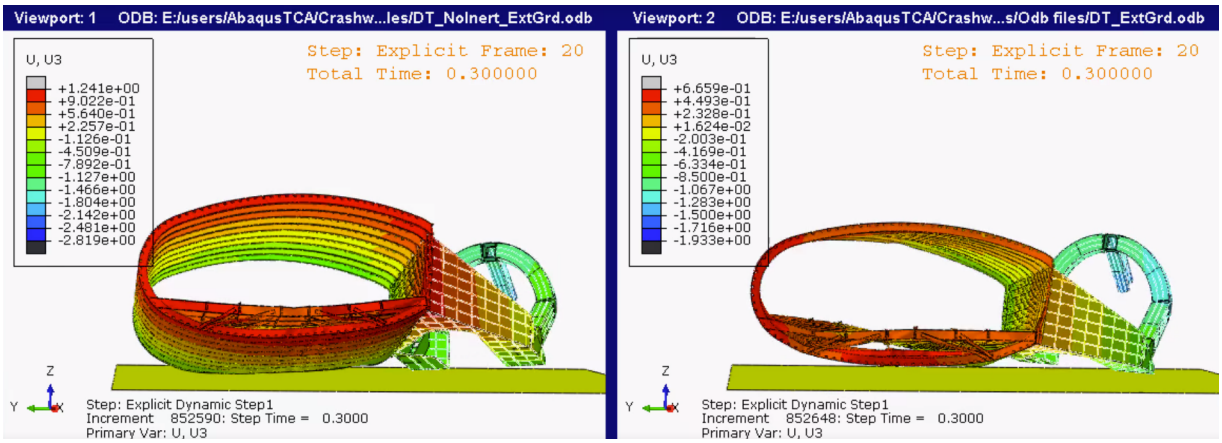

Figure 7.18: Drop-test of non-optimized model with inertia (right) and without inertia (left) after 0.3 seconds. Emphasising the need of the added inertia for simulations with engine mounting structure.

Discussion

Figure 7.17 is fairly similar to Figure 7.11 except for two outliers. The median value only increases slightly, which is likely due to the fact that the inertia does add a little bit of stiffness in a similar fashion as the sliding boundary condition does, bringing the results closer to reality. The total energy absorption is similar, the floor beams and floor long beams absorb a little less whereas the frames absorb more. This can be explained by the restriction of bending of the floor long beams, which then also directly affect the bending of the floor beams. In the end it can be concluded that the inertia does have slight positive effect on the results.

On the other hands shows Figure 7.18 that the added inertia indeed has an effect on the final results when the engine mounting structure is added. This is expected as the additional inertia adds additional rotational resistance to the relatively quite heavy combination of engine mounting structure, landing gear and engine compared to the wing-fuselage plus passengers. The rotation is mainly affected around the y-axis due to location of the heavy engine. The effect of the heavy engine on the difference in rotation around the x-axis is limited, which is as expected as all sections, except for the outer-wing and partly the cockpit, have a similar cross-section. In addition, the added cargo are located

close to this axis, having a small effect on the inertia around the x-axis. In short, the model is behaving as expected with the calculated inertial properties.

The added inertia should not affect the results compared to a simulation with the full model as the loads relative to the contact area and energy absorption capabilities are not altered. To be ensured that this is the case, a computationally heavy and more time consuming, simulation could be ran of the full model and compared in future studies.

Recommendation 29 *Validation of the added inertia can be done using a simulation of the full model in future studies.*

7.3.3. Influence engine mounting structure

Using previous simulation a good comparison case have been formed. The results of the drop test with the engine mounting structure is shown in Figure 7.20 and 7.19 and Table 7.12 below. During the simulations it was forgotten to specify a set regarding the engine mounting structure, therefore the percentage of energy used for plastic deformation could not be extracted. The difference between the sum of all components and the total $\frac{E_D}{K_{eg}}$ is the plastic deformation of the spar and engine mount structure combined which still allows to compare different designs. This holds for the rest of the simulation results in this report.

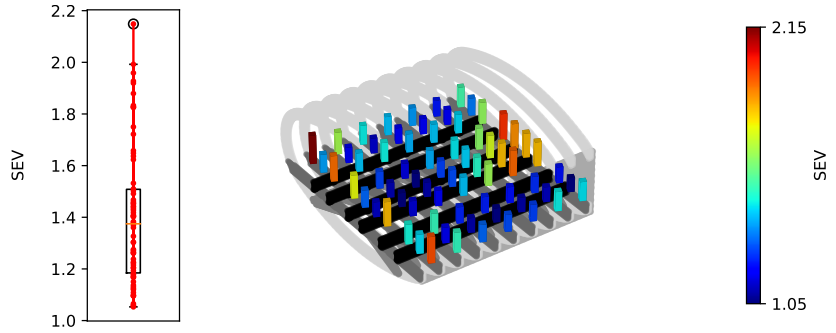

Figure 7.19: SEV of model with engine, showing a large increase of SEV at the back of the section.

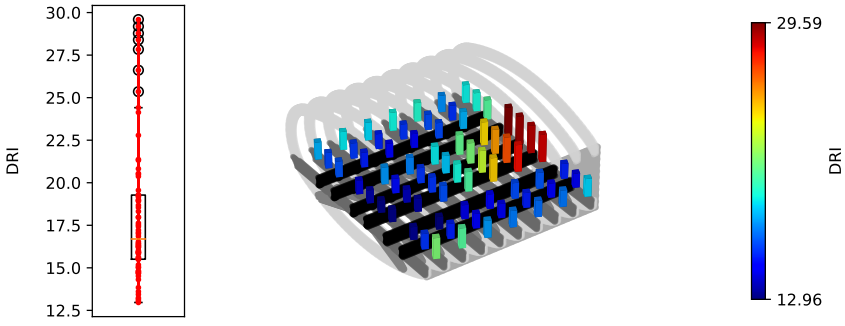

Figure 7.20: DRI of model with engine, showing that the large SEV in the aft section is due to accelerations in the upwards direction.

Table 7.12: Median SEV and dissipated energy per section for inertia and engine simulations, showing that a large portion of the dissipated energy is due to the engine mounting structure. Note, the values of the components might not add up to the total energy dissipated, due to rounding errors.

Energy	Elong. fuselage with inertia	Elong. fuselage with engine
Initial K_{eg} [kJ]	291.35	932.04
Total $\frac{E_D}{K_{eg}}$[%]	68.11	60.90
-Skin [%]	10.28	11.32
-Frames [%]	26.49	18.77
-Struts [%]	10.35	5.53
-Floor beams [%]	10.87	3.54
-Floor long beams [%]	8.26	6.51
——————— - Difference	1.41	15.23
Friction [kJ]	7.39	61.91
Median SEV [-]	1.34	1.38

Discussion
The addition of the engine mounting structure to the drop-test almost triples the mass of the structure and therefore it was expected that the SEV would become way higher and shift more towards the spar. Instead, the median SEV only increased slightly because after some deformation the landing gear box also touches the ground and absorbs some of the energy, which can clearly be seen in Table 7.12. The SEV does not shift towards the spar but rather towards the back. This is due to the gravitational load of the engine mounting structure causing a slight rotation resulting that the back hits the ground and thus start deforming first. The additional mass causes such a big deformation that the floor beams hit the frames resulting in the large decelerations and thus SEV in the back.

The fact that the mass per unit of surface area is constant for the reduced length case does not apply anymore after adding the engine mounting structure. This ratio does increase with a significant amount and therefore for more accurate numbers the full model need to be considered. However, the elongated model still shows the general effect which at this detail of design is considered good enough. It is expected that the SEV would decrease further when the full model is taken into account as it decreases above mentioned ratio.

Nevertheless, these results do emphasize the need of a good connection between the engine mounting structure and wing-fuselage. Currently the connection is made using an unbreakable tie connection but in reality it will endure high stresses. It has shown that it is beneficial for the crash-worthiness that it stays attached and is able to absorb some of the loads efficiently.

Lastly, it also means that the Johnson-Cook model properties of the real material needs to be determined as the energy absorption is significant. The assumption that it would be limited was thus invalid.

7.3.4. Engine separation
A similar simulation as above ran but without the engine mass in order to see the effect of engine separation on the SEV, these results can be seen in Figure 7.22 and 7.21 and Table 7.13.

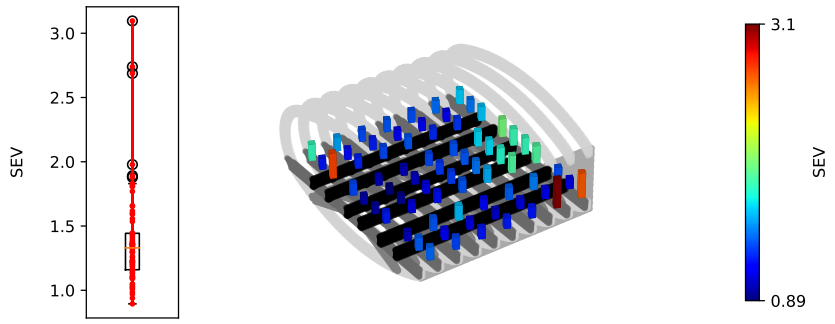

Figure 7.21: SEV of model with engine separation, showing a great reduction in overall SEV except for some outliers.

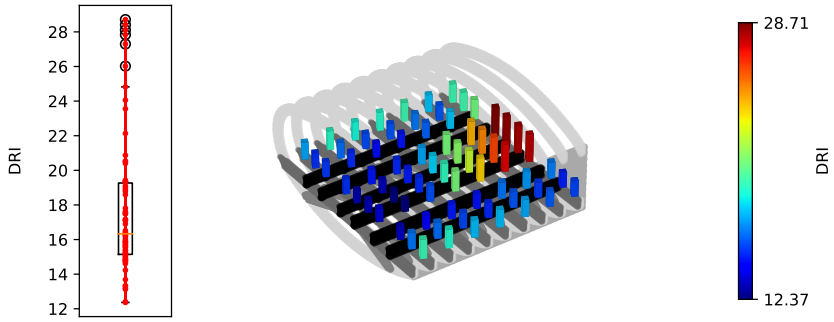

Figure 7.22: DRI of model with engine separation, showing that the increase in SEV in the aft section is due to accelerations in the upwards direction.

Table 7.13: Median SEV and dissipated energy per section for engine and engine separation simulations, showing a significant reduction in the absorbed energy of the engine mounting structure. Note, the values of the components might not add up to the total energy dissipated, due to rounding errors.

Energy	Elong. fuselage with engine	Elong. fuselage with engine separation
Initial K_{eg} [kJ]	932.04	576.85
Total $\frac{E_D}{K_{eg}}$[%]	60.90	66.22
-Skin [%]	11.32	14.07
-Frames [%]	18.77	27.64
-Struts [%]	5.53	7.94
-Floor beams [%]	3.54	3.78
-Floor long beams [%]	6.51	4.74
———————— - Difference	15.23	8.05
Friction [kJ]	61.91	48.68
Median SEV [-]	1.38	1.33

Next to the effect on the SEV, it is also of interest if safe engine separation is even possible. Therefore aforementioned engine-impact model is used for the two explained scenarios and results are shown in Figure 7.23.

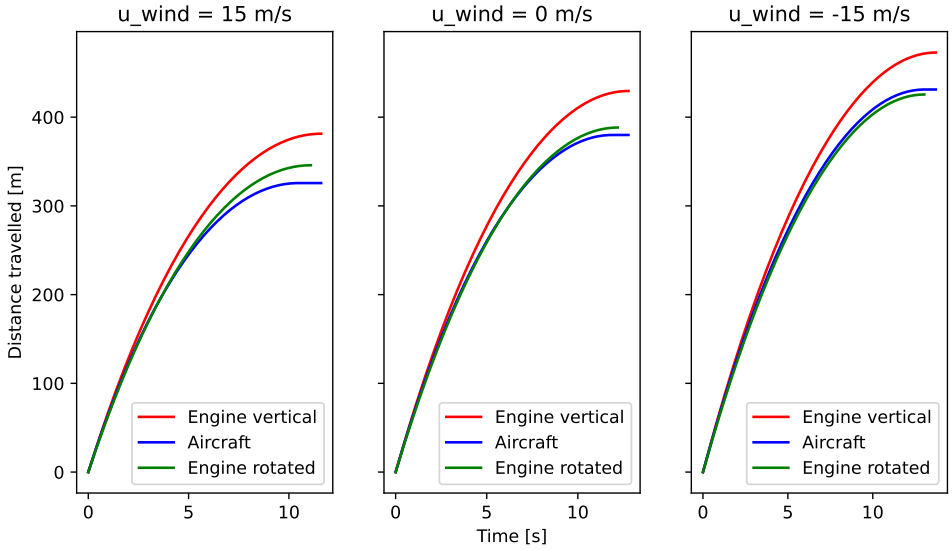

Figure 7.23: The distance travelled of the aircraft and engines for the different separation cases and wind velocities. Illustrating a possibility for safe engine separation using the rotated engine case.

Discussion
The separation of the engine results in a higher maximum SEV, however both the median and interquartile range are lower than with engine. The outliers are due to high horizontal decelerations and it should be investigated how to reduce this in the future. Also in this simulation, thus without the 10 ton engine, do the floor beams hit the frames resulting in the high SEV in the back. Overall the engine separation shows to be beneficial and should be considered in future research.

Beforehand it was thought that safe engine separation is almost impossible for the Flying-V. Although the used model is rather simplistic with quite some assumptions this simulation shows that engine separation is still a topic of interest for future research. This is primarily due to the fact that the rotated separation case has friction right from the start, which causes most of the deceleration.

Recommendation 30 *Safe engine separation for the Flying-V should continued to be investigated in future research.*

7.3.5. Sensitivity analysis

During the creation of the drop-test model only limited assumptions are done, most coming from the engine mount structure. It has been chosen to exclude the redesign from this research therefore most design parameters of the wing-fuselage, such as floor beams, frames, etc., will be excluded from this analysis. However, it has been decided to do an additional simulation with increased thickness of the floor struts to exclude the effect of the floor beam and frame touching. Another main uncertainty which are thought to have a significant influence on the results is investigated within this sensitivity analysis, which is the drag coefficient value.

The floor struts thickness are increased from 2 mm to 3 mm for all the struts and both the simulation with engine and engine separation have been redone. The results of the two simulations are found in Figure 7.24 and 7.25 and Table 7.14. Here again no set was created for the engine mounting structure thus the difference is used to draw conclusions.

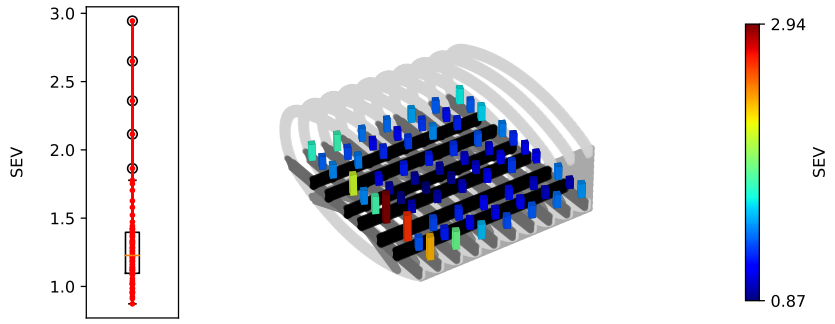

Figure 7.24: SEV of model with engine and 3 mm struts, showing an overall lower SEV due to reduction of DRI in the aft section.

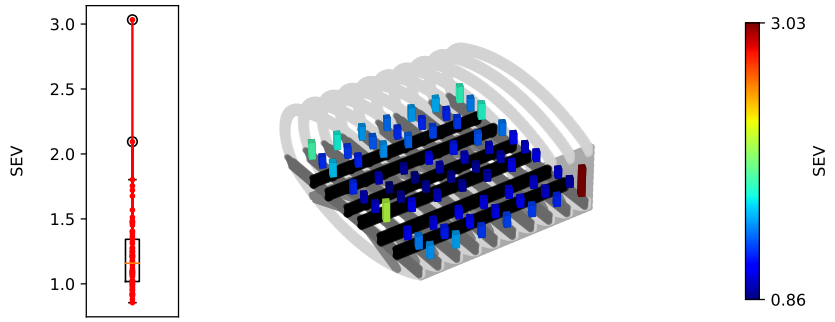

Figure 7.25: SEV of model with engine separation and 3 mm struts, showing an overall lower SEV due to reduction of DRI in the aft section.

Table 7.14: Dissipated energy per section for engine and engine separation simulations.Note, the values of the components might not add up to the total energy dissipated, due to rounding errors.

Energy	Elong. fuselage with engine	Elong. fuselage with engine separation
Initial K_{eg} [kJ]	932.38	577.54
Total $\frac{E_D}{K_{eg}}$[%]	60.03	64.79
-Skin [%]	10.93	13.27
-Frames [%]	17.98	25.66
-Struts [%]	6.89	9.91
-Floor beams [%]	3.15	3.91
-Floor long beams [%]	6.10	4.42
———————— -		
Difference	14.98	7.62
Friction [kJ]	66.83	43.66
Median SEV [-]	1.23	1.16

Above figures show that a thickness of 3 mm for the floor struts indeed results that the floor beams do not touch the frames. This results in significant a lower median SEV of 1.23 and also a significant decrease of the interquartile range. However, there is also sharp increase in maximum SEV which is coming from horizontal components, more specifically the passenger with the largest SEV in model with engine experiences at its peak an acceleration of 412 m/s^2 towards the side. Overall the rest of the conclusions remain the same, the engine mount structure is still beneficial for the crash-worthiness and so does engine separation.

From Figure 7.23 could be concluded that the engine separation is beneficial therefore vertical separation is excluded from this sensitivity analysis. It has been decided to considered drag coefficients of 0.6 to 1 with steps of 0.1. The results are shown in Figure 7.26.

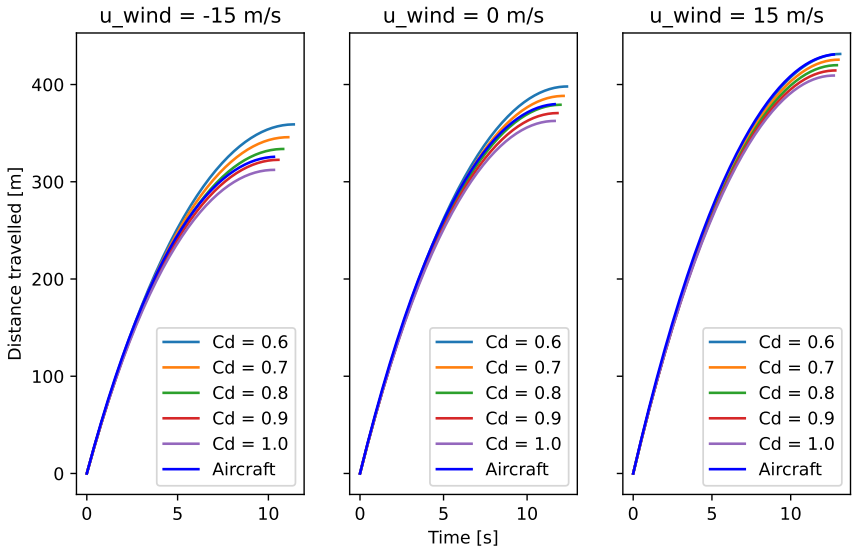

Figure 7.26: The distance travelled of the aircraft and engine for different drag coefficients and wind velocities. Illustrating a possibility of safe engine separation for drag coefficients of 0.9 and 1.0 in most wind conditions.

From Figure 7.26 can be concluded that for higher C_D the separation of the engine becomes really interesting as the separation for this simplistic case is successful independent of wind velocity.

8

Conclusions and Recommendations

In this chapter the conclusion regarding the research objective and summarized answers to the research questions are given. Furthermore, all recommendations done for future research throughout the report are itemized into an overview in chronological order.

8.1. Conclusion

The goal of the research was to develop a certifiable and lightweight engine mounting structure with corresponding joints for the Flying-V which also complies with all set requirements. In order to answer this sub-questions have been made which have been used to get a complete overview of the project. These sub-questions have lead to some interesting findings regarding critical loadcases, the suggested optimization method and the influence of engine mounting structure on the crashworthiness.

From the 25 load cases presented in this report the seven ought to be most critical have been chosen to verify the final design whereof the four most dominant loadcases in previous research were used to optimize the structure. From this optimization study was found that TO-04, LD-06 and LD-08 are indeed critical loadcases and should be included in future optimization studies. On the contrary, CR-02 and TO-05 can be excluded from these studies and further investigation is required to determine if both CR-01 and CR-05 are critical loadcases or if only CR-01 should be considered critical.

The suggested optimization method proved to be only partly successful due to stress concentrations within the design. Most of the elements got a positive MoS within 4 iterations except for the parts with stress concentrations. These stress concentrations affect the final mass negatively as the resultant negative MoS unnecessary influence thicknesses each iteration without solving the stress concentration. As a result, no direct conclusions can be drawn. However, the suggested method has shown to be potentially significantly faster than the Design of Experiment method used in previous research. Furthermore, although no real optimized engine mounting structure could be achieved, it could be concluded that it will be significantly heavier than estimates from previous research. This can be the result of a larger estimated engine mass, higher level of detail or more likely, a combination of both.

Furthermore, the effect of the engine mounting structure on the Flying-V has been assessed by means of a vertical drop-test. Therefore, a new method based on inertia has been developed to reduce the computational effort for a crashworthiness analysis of such a drop-test. This method has proven to not have a direct influence on the results but does indirectly reduce the ratio of crushable volume and mass which only allows to use it for relatively fast but conservative estimates, e.g. trends between designs. The crashworthiness analysis has shown a positive influence of the current engine mounting structure on the crashworthiness, although further investigation is required. This influence is due to the absorbance of impact energy by the engine mounting structure self, which reduces the SEV significantly. Moreover, preliminary results regarding engine separation show possibilities for the current design in the simplest cases and also show that significant lower accelerations are experienced, benefiting the viability of the design.

The developed methods and design does provide a promising starting point that can result in a certifiable engine mounting structure. However, due to simplifications, not taking into account of certain failure modes and stress concentrations it is certain that the current structure is not optimal and does not meet certification at this moment.

8.2. Recommendations

Throughout the report many recommendations for future research were mentioned, and these recommendations are summarized below, in the same order that they were presented in this thesis report. Although all of these recommendations are valid and need to be done to get a better and more realistic design or design methodology the emphasis should be on number 5. The joint between the skin-stiffened landing gear box and rear spar is thought to have the largest effect on the viability of the design during both operation and crash scenarios.

1. Future studies should consider more in-depth material analysis and specific fastening details, such as fastener dimensions or grade.
2. The effects on stability and aerodynamic performance due to change in location of landing gear and engine should be investigated in future research.
3. Future research should investigate solutions for the possible corrosion between aluminium and titanium.
4. In future studies the structure may be further optimized by having different stiffener or rib designs at different places.
5. Adjustments 4 and 5 should be considered in future research.
6. The connection between the skin stiffened landing gear and rear spar should be investigated in future research.
7. In future research the design of the thrust links and engine mounts should be taken into account.
8. Future studies should consider to combine the to be designed landing-gear connection with the skin-stiffened landing gear joints.
9. The loads introduced by the landing gear should be evaluated with more detailed methods in future studies.
10. In future studies the structure should be reassessed by including the engine torque and gyroscopic loads in the load cases.
11. In future studies the dynamic loads of blade loss, shaft failure, failure or loss of bearing/bearing support and bird ingestion needs to be determined.
12. In future studies a gradually changing thickness of the skin should be considered.
13. In future studies each fixed variable to save computation time should be made free.
14. A general method of splitting panels under a random orientation should be investigated in future research.
15. Local panel buckling for curved panels should be investigated in future research.
16. The effect of non-rectangular panels should be taken into account in future research.
17. The effect of crossing stiffeners on the column buckling of a specific stiffener should be included in future research.
18. The Euler-Johnson curve should be considered in future research.
19. The crippling and buckling of curved stiffeners should be included in future research.
20. In future studies the effects of fatigue on the structure should be considered once the details are known.
21. Future research should investigate the effect of creep on the overhead beams.
22. Future studies should investigate the effect of initial imperfections on the structure.
23. In future studies results from the crash-worthiness tests may be implemented in the optimization model.
24. In future research, the inertial properties of the full aircraft needs to be determined more accurately.

25. The inertia of all sections, especially the purple section, needs to be recalculated in the future.
26. In future research the rotation of the aircraft should also be taken into account which can be done using a similar approach as done for the engine.
27. The connection between the joints and panels should be further investigated in future studies to prevent stress concentrations.
28. Future research should include above mentioned parameters into their optimization analysis.
29. Validation of the added inertia can be done using a simulation of the full model in future studies.
30. Safe engine separation for the Flying-V should continued to be investigated in future research.

References

[1] Airbus. (2022). Global Market Forecast. https://www.airbus.com/en/products-services/commercial-aircraft/market/global-market-forecast

[2] Airbus S.A.S. (2021). A350 AIRCRAFT CHARACTERISTICS AIRPORT AND MAINTENANCE PLANNING. https://www.airbus.com/sites/g/files/jlcbta136/files/2021-11/Airbus-Commercial-Aircraft-AC-A350-900-1000.pdf

[3] ANSYS, Inc. (2022). Ansys GRANTA EduPack software.

[4] Bourget, G. (2020). The effect of landing gear implementation on flying v aerodynamics, stability and controllability. https://repository.tudelft.nl/islandora/object/uuid%5C%3A599eca91-6200-4d29-8dd7-e4e7060703e1

[5] Brinkley, J.W and Schaffer, J.T. (1971). *Dynamic simulation techniques for the design of escape systems: Current applications and future air force requirements*.

[6] Chee, W. T. (1983). Aft engine mount [US Patent 4603822A]. https://patents.google.com/patent/US4603822

[7] Corona, E., & Orient, G. (2014). An evaluation of the johnson-cook model to simulate puncture of 7075 aluminum plates.

[8] Curtis, H. (1996). *Fundamentals of aircraft structural analysis*.

[9] De Jonge, J., Schütz, D., Lowak, H., & Schijve, J. (1973). A standardized load sequence for flight simulation tests on transport aircraft wing structures.

[10] Desiderio, M. (2023). Flying-V Crashworthiness: a Preliminary Assessment. http://repository.tudelft.nl

[11] Dotman, T. (2021). A structural sizing methodology for the wing-fuselage of the Flying-V. https://repository.tudelft.nl/islandora/object/uuid%3A69e21e65-7168-4f83-abf5-b646bb4c7fe5

[12] Dym, C. (2010). Solid mechanics. *AIAA Scitech 2020 Forum*, *9780521192*.

[13] EASA. (2021). Certification Specifications and Acceptable Means of Compliance for Large Aeroplanes (CS-25), 177–324. https://www.easa.europa.eu/en/downloads/136622/en

[14] European Union Aviation Safety Agency. (2022). TYPE-CERTIFICATE DATA SHEET for Engine Trent XWB series engines. https://www.easa.europa.eu/en/downloads/7635/en

[15] Franzluebbers, B. (2013). Drag coefficients of inclined hollow cylinders: Rans versus les.

[16] Graz University of Technology. (2020). Engine mounts. https://aeroenginesafety.tugraz.at/doku.php?id=10:10#fracture-of-the-engine-connection-at-the-pylon

[17] Hillen, M. (2020). Parametrisation of the Flying-V Outer Mould Line. https://repository.tudelft.nl/islandora/object/uuid%3Af4863ae4-2792-4335-b929-ff9dfdb6fed5

[18] International Civil Aviation Organization. (2009). TENTH SESSION OF THE STATISTICS DIVISION. https://www.icao.int/Meetings/STA10/Documents/Sta10_Wp005_en.pdf

[19] Jane's Group UK Limited. (2023). Rolls-Royce Trent XWB. https://customer-janes-com.tudelft.idm.oclc.org/Janes/Display/JAE_A008-JAE_

[20] Jones, R. M. (2009). *Deformation theory of plasticity*. Bull Ridge Publishing.

[21] Kassapoglou, C. (2010). Design and analysis of composite structures.

[22] Kassner, M., Smith, K., & Campbell, C. (2015). Low-temperature creep in pure metals and alloys. https://link.springer.com/article/10.1007/s10853-015-9219-2

[23] Kassner, M.E. (2004). *Fundamentals of creep in metals and alloys*. Butterworth-Heinemann.

[24] Martinez-Val, R. (2007). Flying Wings. A New Paradigm for Civil Aviation? *47*. https://pdfs.semanticscholar.org/0f45/87635e7d2bff414d971019aea526f639ff08.pdf?_ga=2.74087442.1891676336.1669626798-121780954.1669203233

[25] Megson, T. (2017). *Aircraft structures for engineering students*. Todd Green.

[26] Mendez, M., Nardo, M., & Benocci, C. (2017). Running fineopen43 simulations at vki: A tutorial and a collection of scripts.

[27] Moulton, B., & D.F., H. (2023). Simplified Mass and Inertial Estimates for Aircraft with Components of Constant Density. https://digitalcommons.usu.edu/cgi/viewcontent.cgi?article=1030&context=mae_stures

[28] Nanninga, M. (2023). High-Fidelity Structural Sizing Method for Weight Estimation of a Flying-V. https://repository.tudelft.nl/islandora/object/uuid:2efac46a-1328-49af-bbd8-685512c3eff3

[29] Nui, M. (1999). *Airframe stress analysis and sizing*. Conmilit Press Ltd.

[30] Obert, E. (2009). Aerodynamic Design of Transport Aircraft. https://books.google.nl/books?id=V1DuJfPov48C&lpg=PA511&pg=PA511&redir_esc=y#v=onepage&q&f=false

[31] Oosterom, W. J. (2021). Flying-V Family Design. http://repository.tudelft.nl/.

[32] Popov, B. N. (2015). *Corrosion engineering*. Elsevier B.V.

[33] Schijve, J. (2009). *Fatigue of structure and materials*. Spinger Science B.V.

[34] Seelen, L., Joseph, T. P., Spofford, H. M., & Orkiszewski, C. S. (1992). Aircraft engine forward mount [US Patent 5277382A]. https://patents.google.com/patent/US5277382

[35] Sjöberg, G. (2008). Aircraft Engine Structure Materials. https://old.amu.ac.in/emp/studym/99999646.pdf

[36] Stech, E.L. and Payne, P.R. (1969). *Dynamic models of the human body*.

[37] Stefanovic, M., & Livne, E. (2021). Structural Design Synthesis of Aircraft Engine Pylons at Certification Level of Detail. https://arc.aiaa.org/doi/pdf/10.2514/1.C035953

[38] The Boeing Company. (2023). Statistical Summary of Commercial Jet Airplane Accidents. https://www.boeing.com/resources/boeingdotcom/company/about_bca/pdf/statsum.pdf

[39] Torenbeek, E. (1982). *Synthesis of subsonic airplane design*. Delft University Press.

[40] Transport Aircraft Crashworthiness and Ditching Working Group. (2018). Transport Aircraft Crashworthiness and Ditching Working Group Report to FAA (Rev. B). https://www.faa.gov/regulations_policies/rulemaking/committees/documents/media/ARAC-TACDWG_FAA_Report-Final_September20_2018ARAC%20W%20AFA%20DISSENT.pdf

[41] United States Air Force. (1971). Mil-s-9479b, military specification: Seat system, upward ejection, aircraft, general specification for.

[42] U.S. Department of Transportation Federal Aviation Administration. (2003). Failure modeling of titanium 6al-4v and aluminum 2024-t3 with the johnson-cook material model.

[43] U.S. Department of Transportation Federal Aviation Administration. (2009). Advisory Circular. https://www.faa.gov/documentLibrary/media/Advisory_Circular/AC20-107B.pdf

[44] Voeten, R. (2022). A design methodology for unconventional engine mounting structures applied to the Flying-V. https://repository.tudelft.nl/islandora/object/uuid%5C%3A8ae4ad77-43d6-44d4-ae34-bb3b118587dd

[45] Wallet, E. (2021). Flying-V Composite.

A

Figures of Limit Plots

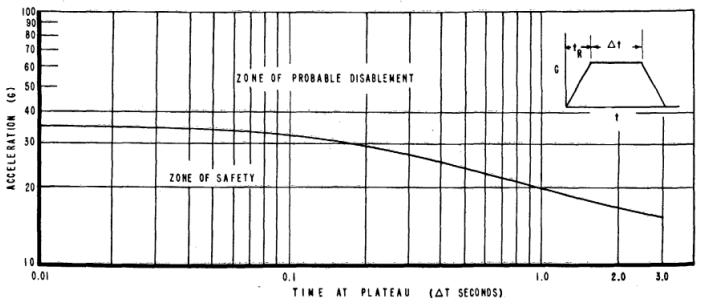

Δt (SEC)	0-.03	.06	.084	.13	.15	.19	.22	.27	.32	.38	.45	.52	.61	.73	.87	1.0	1.22	1.5	1.92	2.45	3.0
G	35	34	33	32	31	30	29	28	27	26	25	24	23	22	21	20	19	18	17	16	15

Figure A.1: Graph to determine G_{xL} for $t_R \geq 0.03$. [41]

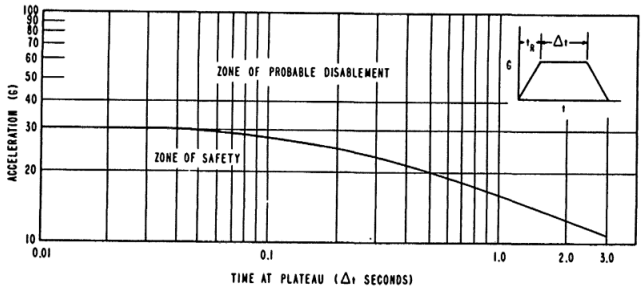

Δt (SEC)	0-.03	.05	.08	.11	.15	.2	.23	.30	.33	.38	.45	.6	.75	.9	1.0	1.2	1.5	1.9	2.5	3.0
G	30	29	28	27	26	25	24	23	22	21	20	19	18	17	16	15	14	13	12	11

Figure A.2: Graph to determine $-G_{xL}$ for $t_R \geq 0.03$. [41]

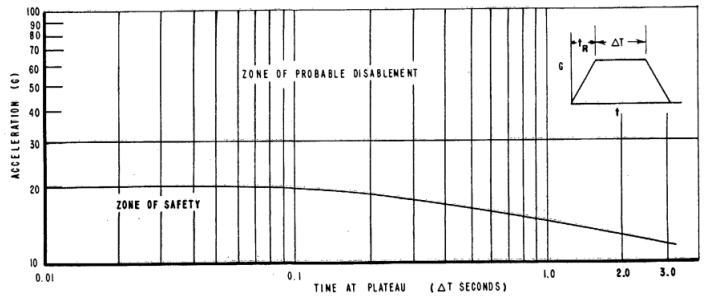

Δ_t (SEC)	0-.03	.085	.15	.25	.36	.52	.75	1.1	1.6	3.0
G	20	19.5	19	18	17	16	15	14	13	11.5

Figure A.3: Graph to determine $\pm G_{xL}$ for $t_R < 0.03$. [41]

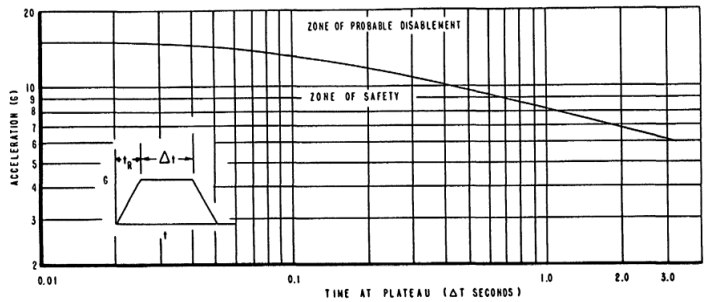

Δ_t (SEC)	0-.03	.06	.11	.18	.28	.41	.62	.86	1.6	3.0
G	15	14	13	12	11	10	9	8	7	6

Figure A.4: Graph to determine $\pm G_{yL}$ for all t_R. [41]

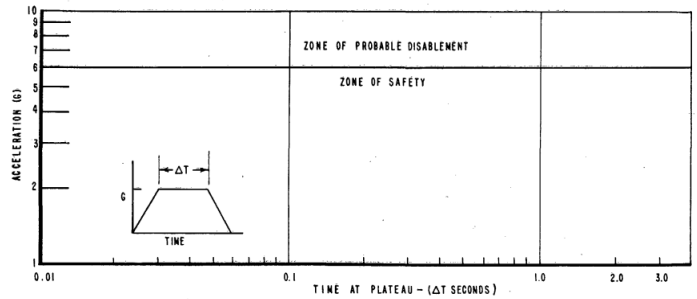

PLATEAU	DURATION M SEC	0-3000
	MAGNITUDE G	6

Figure A.5: Graph to determine $-G_{zL}$ for $t_R < 0.04$. [41]

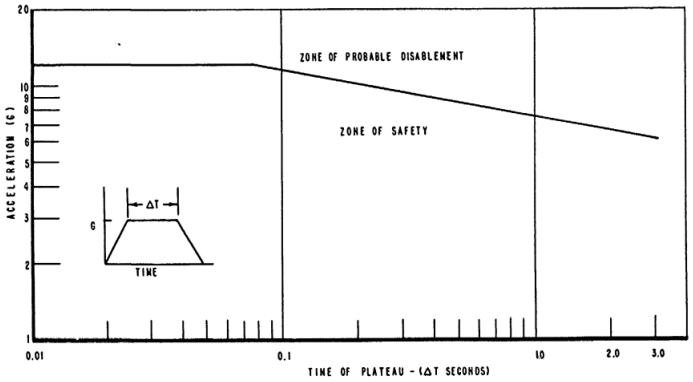

PLATEAU	DURATION MSEC	80	126	208	360	666	1340	3000
	MAGNITUDE G	12	11	10	9	8	7	6

Figure A.6: Graph to determine $-G_{zL}$ for $t_R \geq 0.04$. [41]

B

Design Optimization Figures

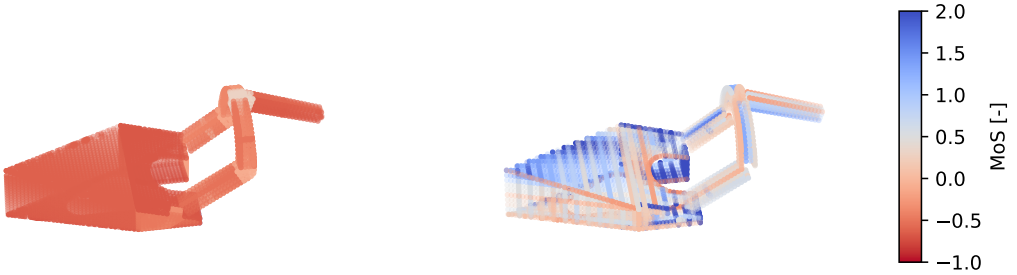

Figure B.1: Minimum MoS values of panels (left) and stiffeners (right) of first iteration.

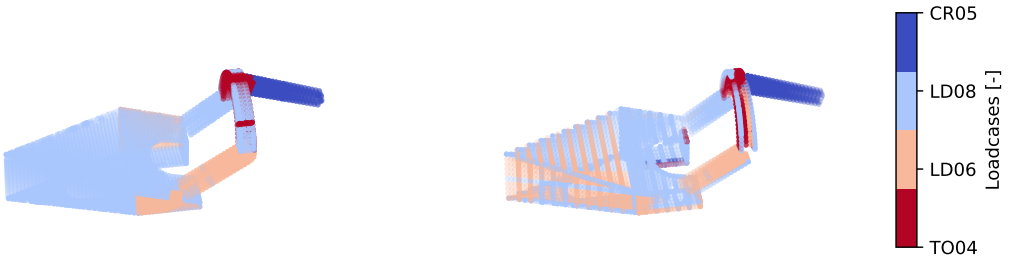

Figure B.2: Responsible loadcase for minimum MoS values occur of panels (left) and stiffeners (right) of first iteration.

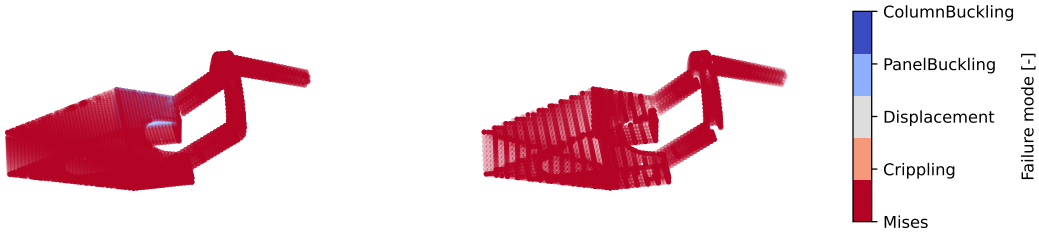

Figure B.3: Responsible failure mode for minimum MoS values of panels (left) and stiffeners (right) of first iteration.

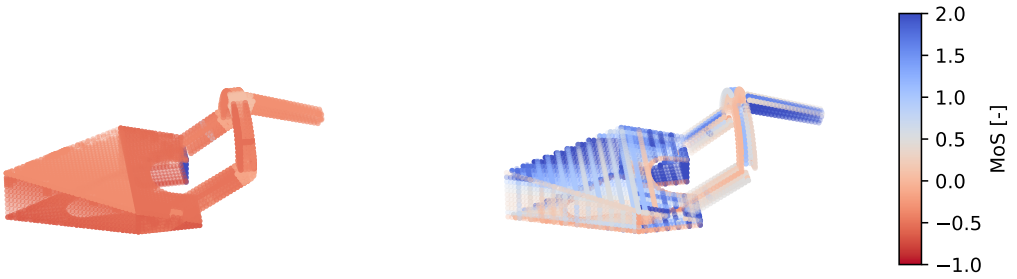

Figure B.4: Minimum MoS values of panels (left) and stiffeners (right) of second iteration.

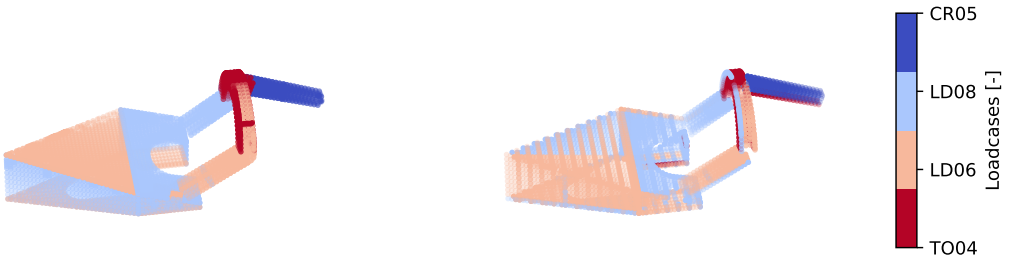

Figure B.5: Responsible loadcase for minimum MoS values occur of panels (left) and stiffeners (right) of second iteration.

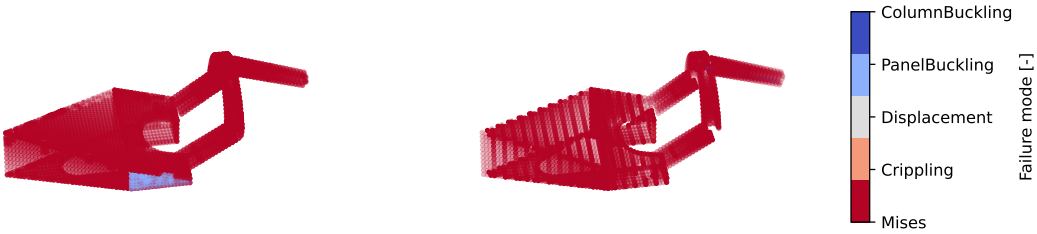

Figure B.6: Responsible failure mode for minimum MoS values of panels (left) and stiffeners (right) of second iteration.

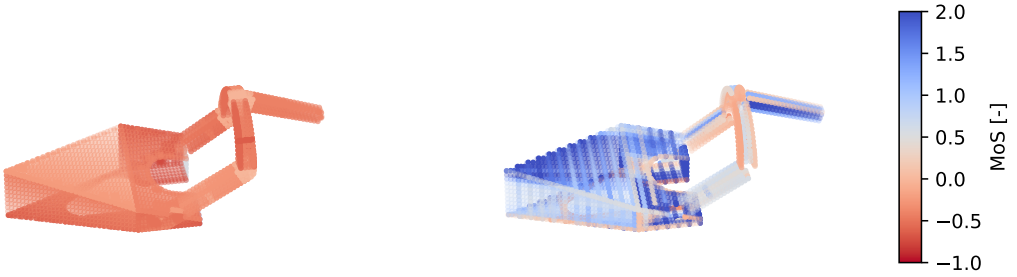

Figure B.7: Minimum MoS values of panels (left) and stiffeners (right) of third iteration.

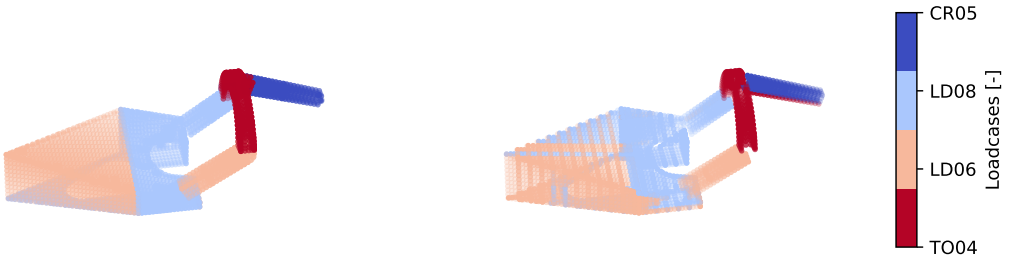

Figure B.8: Responsible loadcase for minimum MoS values occur of panels (left) and stiffeners (right) of third iteration.

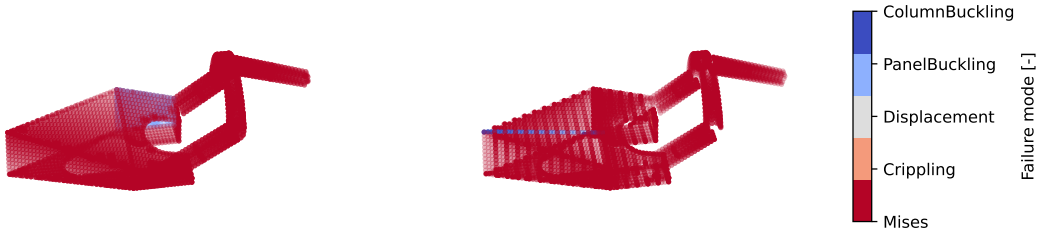

Figure B.9: Responsible failure mode for minimum MoS values of panels (left) and stiffeners (right) of third iteration.

C

List of Assumptions

Throughout the report a number of assumptions are stated. For convenience these assumption are listed in the same order of occurrence below.

1. The mass of the Rolls Royce Trent XWB-97, including nacelle, is 10950 kg.
2. The center of gravity is in the center at 1/3rd of the engine's length.
3. The Trent XWB-97 engine is not able to transfer different kind of loads to the mounts as it does in existing aircraft.
4. The drag and lift generated by the engine can be ignored during operation.
5. Engine torque and gyroscopic loads are small compared to the other load cases.
6. A static load of 256354 N during blade loss is the most critical load during failure.
7. The center of thrust is along the central axis of the engine at the center of the fan.
8. Stiffeners and panels can be simplified to 1D coating and 2D shell elements without having a large effect on the results.
9. The connections represented by couplings are assumed to be relatively rigid compared to the rest of the structure.
10. For each dynamic loadcase, the time step producing the lowest MoS in the Von Mises criterion provides the most critical nodal forces.
11. Applying a follower force is not required as its effect is limited with the set limit on the displacement and rotation of the engine.
12. Sub-panels can be assumed rectangular without underestimating the critical buckling loads.
13. Local panel buckling is more critical than global panel buckling.
14. The crippling of a flange is independent of the length for all stiffeners.
15. The effect of non-rectangular sub-panels have limited effect on the critical buckling load.
16. All non-designed sections are made of Al2024-T361.
17. The aircraft can be divided into five separate sections for a decent indication of the total inertial properties.
18. The blue section contains cargo in a cuboid shape with dimensions of 12.4 x 6 x 2 m and a constant density of 161 kgm^{-3}.
19. The Johnson-Cook variables of Al-7075-T651 are similar to those of Al-7475.
20. The initial rotation after engine separation for the rotational separation case has only a small effect on the final results.